CORRELATING THE MORPHOLOGICAL AND LIGHT SCATTERING PROPERTIES OF BIOLOGICAL CELLS

by

Marina Moran

July 2, 2013

Director of Dissertation: Dr. Jun Q. Lu

Major Department: Physics

The scattered light pattern from a biological cell is greatly influenced by the internal structure and optical properties of the cell. This research project examines the relationships between the morphological and scattering properties of biological cells through numerical simulations. The mains goals are: (1) to develop a procedure to analytically model biological cells, (2) to quantitatively study the effects of a range of cell characteristics on the features of the light scattering patterns, and (3) to classify cells based on the features of their light scattering patterns. A procedure to create an analytical cell model was developed which extracted structural information from the confocal microscopic images of cells and allowed for the alteration of the cell structure in a controlled and systematic way. The influence of cell surface roughness, nuclear size, and mitochondrial volume density, spatial distribution, size and shape on the light scattering patterns was studied through numerical simulations of light scattering using the Discrete Dipole Approximation. It was found that the light scattering intensity in the scattering angle range of 25° to 45° responded to changes in the surface fluctuation of the cell and the range of 90° to 110° was well suited for characterization of mitochondrial density and nuclear size. A comparison of light scattering pattern analysis methods revealed that the angular distribution of the scattered light and Gabor filters were most helpful in differentiating between

the cell characteristics. In addition, a measured increase in the Gabor energy of the light scattering patterns in response to an increase in the complexity of the cell models suggested that a complex nuclear structure and mitochondria should be included when modeling biological cells for light scattering simulations. Analysis of the scattering pattern features with Gabor filters resulted in discrimination of the cell models according to cell surface roughness, nuclear size, and mitochondrial volume density and size with over 90% classification accuracy. This study suggested the location of the scattering planes that are most relevant to researchers depending on the desired information about the cell and may provide a quantitative approach to cell discrimination with practical applications in flow cytometry for the diagnosis of diseases.

CORRELATING THE MORPHOLOGICAL AND LIGHT SCATTERING PROPERTIES OF BIOLOGICAL CELLS

A Dissertation

Presented To the Faculty of the Department of Department of Physics

East Carolina University

In Partial Fulfillment of the Requirements for the Degree

Doctor of Philosophy in Biomedical Physics

by

Marina Moran

July 2, 2013

CORRELATING THE MORPHOLOGICAL AND LIGHT SCATTERING PROPERTIES OF BIOLOGICAL CELLS

by

Marina Moran

APPROVED BY:

DIRECTOR OF
DISSERTATION/THESIS: _____
Jun Q. Lu, PhD

COMMITTEE MEMBER: _____
Xin-Hua Hu, PhD

COMMITTEE MEMBER: _____
John M. Kenney, PhD

COMMITTEE MEMBER: _____
Jae Won Jung, PhD

COMMITTEE MEMBER: _____
Jean-Luc Scemama, PhD

ACTING CHAIR OF THE DEPARTMENT
OF PHYSICS:_____
Jefferson Shinpaugh, PhD

DEAN OF THE
GRADUATE SCHOOL: _____
Paul J. Gemperline, PhD

ACKNOWLEDGEMENTS

I would like to thank my advisor, Dr. Jun Lu, for our daily discussions guiding me through this project. She encouraged me to think and provided invaluable feedback and suggestions. I would like to thank my committee members, Dr. Kenneth Jacobs, Dr. Michael Dingfelder, and Dr. Zi-Wei Lin for also taking the time to talk with me and providing their feedback. I am also thankful for Dr. Xiangming Fang for his extensive help on using SPSS, Dr. Chris Carolan and Dr. Said Said for their numerous talks on statistics, and Dr. Scott Brock for his help with my coding and computing issues for the past six years. I would also like to thank Dr. Scott Brock and Wenhuan Jiang for providing confocal images of biological cells.

I am also thankful for my friends Ioannis Gkigkitzis, Maria Clara Ferreira, Chris Snook, Carissa Reynolds, and Drew Ligon for their patience, encouragement, and support. Finally, I am forever indebted to Jason Walker for going out of his way to allow me to dedicate myself to my studies and for showing his never-ending support.

TABLE OF CONTENTS

LIST OF TABLES i

LIST OF FIGURES ii

LIST OF ABBREVIATIONS v

CHAPTER 1: INTRODUCTION 1

CHAPTER 2: CELL MORPHOLOGY 6

2.1. Index of refraction 6

2.2. Cell surface 6

2.3. Nucleus 7

2.4. Mitochondria 8

CHAPTER 3: LIGHT SCATTERING THEORY 12

3.1. Solving for the scattered field 12

3.2. Polarization properties of the scattered field 17

3.3. Optical properties of the scatterer 20

CHAPTER 4: Light scattering simulations 22

4.1. Discrete Dipole Approximation 22

4.2. ADDA 24

4.3. Consideration of errors in ADDA 25

CHAPTER 5: LIGHT SCATTERING PATTERN ANALYSIS AND CLASSIFICATION 33

5.1. Haralick features 33
5.2. Laws measures 35
5.3. Gabor filters 37
5.4. Discriminant analysis 40
CHAPTER 6: ANALYTICAL CELL MODELING 43
6.1. Modeling the base shape 43
6.2. Gaussian random sphere geometry 47
6.3. Modeling the surface fluctuation 50
6.4. Validation of surface fluctuation parameter extraction procedure 51
6.5. Modeling cellular organelles 59
6.6. Selection of cell model parameters 62
CHAPTER 7: COMPARISON OF LIGHT SCATTERING PATTERN ANALYSIS METHODS 65
7.1. Simulation methodology 65
7.2. Analysis of angular distribution of the scattered light intensity 70
7.3. Analysis of light scattering diffraction image 76
CHAPTER 8: CORRELATING THE MORPHOLOGY AND LIGHT SCATTERING PATTERNS OF BIOLOGICAL CELLS 81
CHAPTER 9: CLASSIFICATION OF CELLS BASED ON MORPHOLOGICAL PARAMETERS 91

9.1. Simulation methodology 91

9.2. Results and discussion 99

CHAPTER 10: CONCLUSION 112

REFERENCES 116

APPENDIX A: REPRESENTATION OF AN ELLIPSOID WITH ARBITRARY ORIENTATION IN SPHERICAL COORDINATES 124

APPENDIX B: CLASSIFICATION RESULTS FOR INCIDENT LINEAR POLARIZATIONS PARALLEL AND AT A 45° ANGLE TO THE SCATTERING PLANE 125

LIST OF TABLES

Table 6.1. Average (s.d) Gaussian sphere parameters recovered for a Gaussian sphere..... 54

Table 6.2. Original and average recovered parameters for 50 realizations of Gaussian spheres..... 57

Table 6.3. Recovered Gaussian sphere parameters for four B-cell surfaces and nuclei..... 62

Table 9.1. Set of twenty-four incident angles for electric field used in simulations 96

Table 9.2. Summary of number of cell models and groupings..... 101

Table 9.3. Classification accuracy for training set and test set for various cell characteristics. 111

Table B1. Classification accuracy for various cell characteristics for incident linear polarization parallel to the scattering plane 125

Table B2. Classification accuracy for various cell characteristics for incident linear polarization at a 45° angle to the scattering plane 126

LIST OF FIGURES

Figure 2.1: Examples of diffuse, peripheral, and perinuclear mitochondrial distributions 11

Figure 3.1: Configuration of light scattering from an arbitrary particle 13

Figure 3.2: The polarization states of the incident and scattered field, measured relative to the scattering plane 18

Figure 4.1: Comparison of S_{11} calculated by Mie theory and ADDA for a sphere of $r = 5.0\mu m$ and $m = 1.04$ 28

Figure 4.2: Comparison of $-S_{12}/S_{11}$ calculated by Mie theory and ADDA for a sphere of $r = 5.0\mu m$ and $m = 1.04$ 29

Figure 4.3: Comparison of S_{33}/S_{11} calculated by Mie theory and ADDA for a sphere of $r = 5.0\mu m$ and $m = 1.04$ 30

Figure 4.4: Comparison of S_{34}/S_{11} calculated by Mie theory and ADDA for a sphere of $r = 5.0\mu m$ and $m = 1.04$ 31

Figure 4.5: Comparison of S_{11} calculated by ADDA with *dpl*=24 and S_{11} calculated by ADDA with various *dpl* for a Gaussian sphere of $r = 5.0\mu m$ and $m = 1.04$ 32

Figure 5.1: Calculation of the co-occurrence matrix 34

Figure 5.2: Laws filter masks 35

Figure 5.3: Example of Gabor filtering 39

Figure 6.1: Illustration of procedure to obtain cell surface points. 46

Figure 6.2: Examples of Gaussian random spheres with different values for ν and σ 49

Figure 6.3: Comparison of covariance functions of logradius calculated from Gaussian spheres to the analytical form 53

Figure 6.4: The residual as a function of l_{max} in the covariance function fitting for a Gaussian sphere with different fixed values for ν 55

Figure 6.5: Comparison of original Gaussian sphere with Gaussian spheres generated with average recovered parameters 58

Figure 6.6: Examples of covariance functions calculated for a Gaussian sphere and analytical forms of the covariance function..... 59

Figure 6.7: Cell models showing the effect of changing the percentage of ellipsoidal fluctuations and the number of nearest neighbors used in the window average when modeling the nuclear substructures 61

Figure 6.8: Comparison of reconstructed and analytical 3D models of biological cells 63

Figure 6.9: Comparison of simulated and experimental $\perp\perp$ polarization images for a cell 64

Figure 7.1: Projection image schematic for light scattering simulations 68

Figure 7.2: Examples of cell models and their corresponding projected scattering images 69

Figure 7.3: The azimuthally-averaged angular distribution of the scattered light intensity averaged over the eight incident orientations 72

Figure 7.4: Bi-parameter scatter plots of the forward intensity versus the azimuthally-averaged intensity integrated over the scattering angle range of (a-e) 90°–110° and (f-j) 25°–45°..... 75

Figure 7.5: Gabor scatter plot with data from all cell models in groups #1 - #5 77

Figure 7.6: Haralick and Laws scatter plots for cell models in group #5 78

Figure 7.7: (a) The forward intensity versus the azimuthally-averaged intensity integrated over the scattering angle range of 90°–110° and (b) the Gabor scatter plot for cell models with different nucleus-to-cell volume ratios..... 79

Figure 8.1: (a-g) Cell models with increasing nuclear complexity and their corresponding $\parallel\parallel$ and $\parallel\perp$ polarization images 84

Figure 8.2: (a-g) Cross sections of the seven cell models with surface fluctuation with increasing nuclear complexity and their ∥ ∥ and ∥⊥ polarization images 85

Figure 8.3: (a-g) Cross sections of the seven cell models with surface fluctuation and mitochondria with increasing nuclear complexity and their ∥ ∥ and ∥⊥ polarization images 86

Figure 8.4: Analysis with Gabor filters of polarization images for eight cell models depicted in the previous figure 87

Figure 8.5: Cross sections of cell models with increasing mitochondrial density and their ∥ ∥ and ∥⊥ polarization images 89

Figure 8.6: Analysis of polarization images for the seven cell models showing the effect of increasing mitochondrial volume density 90

Figure 9.1: Probability density functions used for the modeling of mitochondrial (a) shape and (b) size 94

Figure 9.2: Examples of cell models used in simulations..... 95

Figure 9.3: Projection image schematic for light scattering simulations 98

Figure 9.4: Classification results from discriminant analysis for cell surface roughness for (a) the training set and (b) the test set. 106

Figure 9.5: Classification results from discriminant analysis for nuclear size for (a) the training set and (b) the test set. 107

Figure 9.6: Classification results from discriminant analysis for mitochondrial distribution for (a) the training set and (b) the test set. 108

Figure 9.7: Classification results from discriminant analysis for mitochondrial volume density for (a) the training set and (b) the test set. 109

Figure 9.8: Classification results from discriminant analysis for mitochondrial shape and size for (a) the training set and (b) the test set. 110

LIST OF ABBREVIATIONS

2D	Two-dimensional
3D	Three-dimensional
ANOVA	Analysis of variance
AR	Aspect ratio
DDA	Discrete dipole approximation
DFA	Discriminant function analysis
DPL	Dipoles per wavelength
EM	Electromagnetic
FDTD	Finite-difference time-domain
LDR	Lattice dispersion relation
LDF	Linear discriminant function
MPI	Message passing interface
M/C	Mitochondria to cell volume fraction
N/C	Nucleus to cell volume fraction
RMS	Root mean square
TEM	Texture energy measures

CHAPTER 1: INTRODUCTION

The light scattering pattern from biological cells contains rich information regarding the cell structure and its optical properties. Due to the complexity of the internal structure of the cell, the light scattering pattern formed through the interference of the scattering wave fields from various components in the cell is rather complicated, and no simple relation can be established between individual speckles in the scattering pattern and particular components of the cell [1]. A good understanding of the relationship between the morphological and light scattering properties of biological cells is critical in obtaining accurate information regarding the physiological condition of the cells. Due to the close correlation between the scattered light and the cell internal structure, the scattered light signal has the potential to become a very useful tool for providing significant information on the metabolic state of the cells and for the early detection of diseases. For this reason, the interaction between light and biological cells has attracted significant research efforts over the past century.

Early studies approximated biological cells as homogeneous spheres or as coated, or concentric spheres. It was found that the forward scattering was mostly influenced by the volume of the scatterer and that the presence of a nucleus did not significantly influence the forward scatter. It was also discovered that the internal structure of the cell influenced light scattering at larger scattering angles [3, 4, 5]. Several studies also provided some estimation for the cell membrane thickness and the size and index of refraction of the cytoplasm and nucleus [6, 7].

The understanding of the light-cell interaction improved over the years as smaller structural features in biological cells were introduced into the cell models. Some of the models contained various size distributions of spheres and ellipsoids [8], while others used a multilayer cell model

to represent various layers in cells, including the nucleus and mitochondria. The results of these studies suggested that the small structures played a major role in the light scattered from a cell and that the presence of small organelles significantly increased the scattering intensity for all angles, especially for angles above 90° [9]. Additional cell characteristics, such as approximate sizes for the various substructures in the cells, were also obtained [10, 11, 8].

The effects of inhomogeneity in the index of refraction distribution in biological cells have also been considered by some of the more recent studies and several different approaches have been proposed. Kalashnikov et al. used modifications of index tomograms, or three-dimensional (3D) refractive index maps of cells, to systematically examine the effects of the nucleolus and the nucleus on the scattering pattern [12]. Li et al. modeled the fluctuations in the index of refraction fluctuations with the Gaussian Random Field model with 3D realizations implemented using the turning-band method [13]. This latter approach allowed for the modeling of refractive index variations with scales of the same order as those in biological cells.

More recent light scattering studies have used cell models with higher complexity. Red blood cells were modeled as biconcave disks to investigate the effect of changes in orientation, volume and diameter, and each parameter had a noticeable effect on the scattering pattern [14]. Brock et al. constructed realistic cell models composed of a cell membrane and nucleus using z-stacks of confocal microscope images from B-cells [15]. Results indicated that the coated sphere was a poor model for B-cells for scattering at angles larger than 20° and that the small shape features in the realistic model changed the scattering pattern for larger scattering angles [15].

While many light scattering studies focused on analyzing the azimuthally-averaged angular distribution of the scattered light intensity, where only the cell size and some limited information regarding the internal structure of the cell could be obtained [16, 17, 18, 19, 20], recent

developments have focused on analyzing two-dimensional (2D) diffraction images, which contain rich information regarding the cell structure and its optical properties. Various analysis methods have been applied to these images in attempts to extract 3D morphological features from cells. Fourier analysis of the scattering patterns was suggested to obtain information about the distribution of mitochondria as well as the size of biological cells [21, 22]. A label-free speckle analysis technique was developed to discriminate between an aggregate distribution of mitochondria present in normal hematopoietic cells and a randomly-distributed diffuse distribution present in leukemic cells [23]. Other texture analysis techniques such as Haralick features [24] and Laws' energy measures [25] were used to analyze light scattering patterns and differentiate between perinuclear, diffuse, peripheral, and aggregate distributions from simple, spherical cell models [26, 27].

While the results mentioned above have shown promise of quantitative discrimination of cells based on various morphological characteristics, the methods have not been capable of detecting variations in a range of cell properties such as the number and volume density of mitochondria and have only been applied to simplified models with spherical or ellipsoidal mitochondria [23]. The main goal of this research is to utilize a realistic biological cell model in numerical light scattering simulations to quantitatively study the effects of a range of cell morphological characteristics on the light scattering patterns and to classify the patterns based on these characteristics.

Since small morphological changes in cells affect how light scatters from the cells, accurate modeling of biological cells is important for light scattering simulations. The first objective of this dissertation research is to develop a method to create an analytical 3D model of biological cells which is accurate and practical for light scattering simulations. While simple biological cell

models have contributed greatly to the understanding of the light-cell interaction, they do not allow much flexibility for a systematic study of the effect of structural features of a cell on the light scattering pattern. The cell model proposed in this study is based on the literature and on the structural information extracted from stacks of confocal microscopy images of biological cells. It is very flexible and easily allows for changes in cell surface shape, nuclear substructures, and mitochondrial properties.

The second objective is to measure the changes in the light scattering properties of the cell models in response to systematic variation of cell morphological properties. Through this objective, we determine the parts of the light scattering patterns which provide the most pertinent information about the cells, discover the methods most suitable for the analysis of light scattering patterns, and demonstrate the need for realistic cell modeling in light scattering simulations.

The third objective is to classify the scattering patterns from the biological cell models according to various morphological characteristics. This is achieved by analyzing the scattering patterns with Gabor filters and using discriminant analysis to group the images. Results of this study can provide guidance to experimentalists by suggesting the ideal number and position of detectors in flow cytometry measurements depending on the desired information about the scatterer.

The remainder of this document is organized as follows: An overview of cell morphology and its connection to cell physiology is presented in Chapter 2. A physical description of light scattering is presented in Chapter 3, and a description and validation of the method used to simulate light scattering cells is provided in Chapter 4. The techniques used to analyze and classify the light scattering patterns are then introduced in Chapter 5. The final chapters present the results from this study. The procedure and the models created to represent biological cells

are described in Chapter 6. The comparison of the light scattering pattern analysis methods and efforts to correlate the morphology and light scattering patterns of biological cells are provided in Chapters 7-8. The classification of the light scattering patterns based on the morphological characteristics of the cells is presented in Chapter 9. Finally, Chapter 10 summarizes the research and suggests future directions for this research.

CHAPTER 2: CELL MORPHOLOGY

This chapter provides an overview of the optical and structural properties of biological cells with an emphasis on the characteristics of lymphocytes. Lymphocytes are white blood cells found in the immune system that can vary in size from 4.8 to 12.0 μm [11, 28]. They produce antibodies and other molecules to rid the cell of invaders and have the potential to be useful markers for the identification and diagnosis of various diseases.

2.1. Index of refraction

Biological cells are composed of cytoplasm and various organelles such as a nucleus and mitochondria, resulting in an inhomogeneous spatial distribution in their refractive index as well as in their dielectric properties. A wide range of values for refractive indices of the cell components can be found in the literature. The cell membranes, composed mostly of lipids and proteins, have refractive indexes in the range of 1.46 to 1.54; the index of refraction of the cytoplasm varies from 1.35 to 1.37; the refractive index of the nucleus varies from 1.38 to 1.41; and that of the mitochondria ranges from 1.38 to 1.41 [29, 30, 31, 32].

2.2. Cell surface

The cell surfaces of lymphocytes have varying degrees of roughness due to ruffles and folds on the surface [28]. Protrusive structures called microvilli with lengths from 0.3 to 0.4 μm can be seen on the surface of lymphocytes with electron microscopy [33]. The roughness of the cell surface also depends on the cell's environment and physiological condition. One study showed that lymphocytes had folded membranes when placed in isotonic and hypertonic solutions, while the membranes were much smoother and the cells had a nearly spherical shape in hypotonic

solutions [34]. Also, after coculture with a leukemia cell line, lymphocytes appeared much smoother than normal, possibly due to damage to the surface or to changes in the composition of the cell membrane. Before coculture, the average roughness of lymphocytes was approximately 0.35 μm, while after coculture it was 0.1 μm [35]. In addition, percentages of smooth and non-smooth lymphocytes differed in individuals with hepatitis B and C viruses, tick-borne encephalitis, and herpes simplex as compared to healthy individuals [32].

2.3. Nucleus

The nucleus is the cell's most prominent organelle and contains most of the cell's genetic material. It is surrounded by a thin nuclear envelope (~0.1 μm) which separates it from the cytoplasm. A wide range of sizes for the nucleus of lymphocytes has been reported, varying from 4.1 to 8.8 μm, although the ratio of nucleus to cell size tends to stay constant [28]. One study found that there was a positive correlation between the nucleus and cell size and suggested that the nucleus made up approximately 55% of the cell's volume for lymphocytes [28]. The same study also found that in lymphocytes, the nucleus had an ellipsoidal shape and was off-centered in the cell by about 0.3 μm [28]. One of the main structures in the nucleus is the nucleolus, which transcribes ribosomal RNA. The nucleus contains 1-3 nucleoli, which are denser than the nucleus and have sizes in the range 0.5 to 1.4 μm [28].

Changes in nuclear morphology are useful indicators for diagnosing pathological conditions in cells. Fluctuations in the refractive index of the nucleus have been associated with intestinal carcinogenesis and mitosis [10, 36]. Other nuclear morphological changes, including nuclear enlargement, changes in surface shape, and increased number of nucleoli per unit area, have been linked to specific cancer types and can assist in the diagnosis of cancer [10, 37, 31].

Interestingly, a study reported that in lymphocytes of autistic children, the nuclei appeared reduced in size; electron micrographs showed nuclei to be as small as 30% of the cell's volume [38].

2.4. Mitochondria

Mitochondria are present in virtually all animal cells and produce most of the energy needs of a cell. They perform a host of cellular functions and play a central role in differentiation, aging, and apoptosis [39, 40, 41]. Each mitochondrion is bounded by two membranes. The outer membrane encloses the entire contents of the mitochondrion, while the inner membrane has a much greater surface area and forms a series of folds or invaginations [39]. Proteins inside mitochondria cause fission and fusion of the organelle and control mitochondrial morphology [42]. Defects in mitochondrial function are implicated in a number of diseases such as cancer, bipolar disorder, Parkinson's and Alzheimer's diseases [41, 42, 43]. Because these defects are manifested through changes in mitochondrial volume density, shape, size, and spatial distribution, these parameters and their clinical relevance are examined below.

The number of mitochondria in cells varies according to cell type and cell health. Some cells, such as some sperm and yeast cells, have only a few mitochondria. Other cells, such as skeletal muscle and liver cells, may contain thousands of mitochondria [44]. While the mitochondrial volume density for most cells ranges from 15-22% [44], several studies indicate that the density for lymphocytes is smaller. The average number of mitochondria in lymphocytes can be as low as 3.2 mitochondria per cell [32], but the volume density has also been measured to be as high as 9.6% [45].

For any type of cell, the mitochondrial volume density is also affected by the physiological

condition of the cells. For example, increased metabolic activity within a cell tends to generate increased numbers of mitochondria [42]. On the contrary, during some processes such as pyknosis or ballooning that happen during apoptosis, the number of mitochondria can be reduced [42]. Several studies have related differences in the volume density of mitochondria to specific medical conditions. In one study, low-grade benign tumors contained high numbers of mitochondria, while high-grade tumors (tumors with a high proliferation index) had fewer mitochondria [42]. Another study analyzing lymphocytes from schizophrenic patients showed that the volume density of mitochondria in large activated lymphocytes was significantly lower in the schizophrenic patients as compared to the control group [45].

Besides varying in volume density, mitochondria can also be found in many forms. Although mitochondria are typically portrayed as having tubular shapes, they can attain various shapes and form large networks in response to cellular processes and perturbations. During cell division and apoptosis, mitochondria are fragmented and form small ovoid or round structures, while during cell starvation or degradation, mitochondria can elongate and be spared from death [42, 46, 47]. Also, dysfunctional mitochondria have been observed to lose their network structure and become more round compared to normal mitochondria [42]. A study investigating the role of mitochondria in the resistance of tumor cells to anticancer drugs showed that mitochondria in drug-resistant cells displayed a star-lobed morphology in contrast to the filamentous, polymorphic structures of those in drug-sensitive cells [48]. Another study observed mitochondria changing from a tubular shape to a donut and a blob form in response to increased oxidative stress [46].

Likewise, the size of mitochondria also varies. The length has been reported to range from 0.2 μm to more than 2.0 μm [41, 42]. Size variations occur as mitochondria shrink and swell as

a response to their environment, and various reagents cause changes in mitochondrial volume during ATP synthesis [49]. The enlargement of mitochondria has been attributed to a wide range of abnormal conditions, such as ischemia (restriction in blood supply to tissue) and deficiencies of riboflavin or essential fatty acids [44]. For example, a study showed enlarged, swollen mitochondria in peripheral blood lymphocytes from iron-deficient patients [50]. It has also been reported that the mean diameter of mitochondria in cancer cells is up to 15% larger than in normal cells [42]. Sometimes, however, smaller mitochondria are found in patients with various disorders and are seen interspersed with larger mitochondria in normal cells [44, 41, 39].

As mitochondria change in volume density, shape and size in order to meet the different functional needs of the cell, it is not surprising that they are also distributed in the cells in various spatial conformations. Some distributions that have been documented are the diffuse (spread out in the cytoplasm), the peripheral (located near the cell periphery), and the perinuclear (located near the nucleus). Mitochondria tend to locate where the energy is required, so changes in the spatial distributions reflect changes in the metabolic state of the cell and have been linked to a number of cell physiological processes and diseases [51, 43]. In one study, cultured cancer cells sensitive to chemotherapeutic drugs displayed aggregation to the nucleus, while in drug-resistant strains, they displayed increased peripheral activity [48]. In a study where the CO_2 content of the environment was systematically increased, perinuclear mitochondria were found in the low CO_2 content environment, while diffuse mitochondria were found in the high CO_2 environment [51]. However, it is unclear where the mitochondria are located during normal cell function; both the perinuclear and diffuse distributions have been identified during a cell's normal life, while the perinuclear distribution has also been identified for bipolar disorder cells and the diffuse distribution has also been found in cancer cells [42, 41, 10]. The confocal microscopy images

presented in Figure 2.1(a-c) provide examples of diffuse, peripheral, and perinuclear mitochondrial distributions, respectively. These images are from Ramos and Jurkat cells, which are B and T lymphocyte cells, respectively.

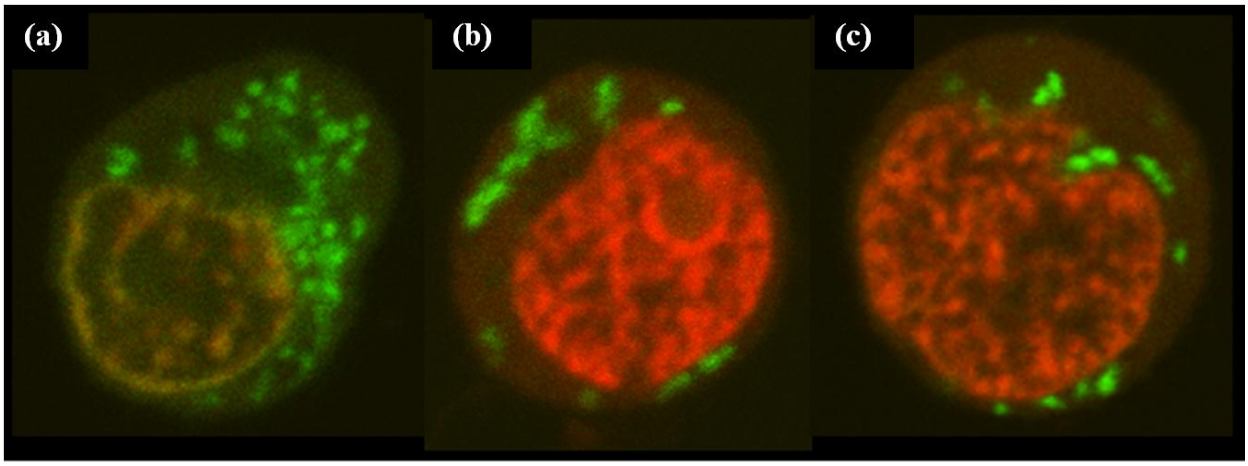

Figure 2.1: Examples of diffuse, peripheral, and perinuclear mitochondrial distributions in cells. (a) Diffuse distribution in a Ramos cell; (b) Peripheral distribution in a Jurkat cell; (c) Perinuclear distribution in a Jurkat cell. The plasma membrane is stained with green dye and the nucleus with red dye. *Confocal images courtesy of Dr. Xin-Hua Hu.*

CHAPTER 3: LIGHT SCATTERING THEORY

The scattering of light occurs when an electromagnetic (EM) wave encounters a particle with variations in its EM properties. Through interactions with the molecules in the heterogeneous particle, the EM wave induces oscillating dipole moments, resulting in the scattered light. The scattered field is dependent on the optical properties of the scatterer and it is thus of great interest to be able to calculate this field in order to learn about the scatterer. For particles much smaller than the wavelength, the Rayleigh theory can be used to solve for the scattered field. In this approximation, the scattering particles are treated as electric dipoles, resulting in the scattering cross section varying inversely with the fourth power of the wavelength. For particles much larger than the wavelength, geometrical optics, or ray optics, can be used [52]. Ray optics treats light as a collection of rays that travel in straight lines and bend when they pass through or reflect from surfaces, but neglects diffraction and polarization. For particles whose size are similar to the wavelength, the method used to solve the light scattering problem must account for the wave nature of light and therefore must be based on Maxwell's equations [53]. In this section, the scattering problem is formulated and solutions for the scattered field are discussed.

3.1. Solving for the scattered field

The light scattered from a single particle of arbitrary shape and size depends on the incident light and the scattering particle. Figure 3.1 illustrates scattering by an arbitrary particle. The direction of scattering ($\hat{e}_r$), i.e., the direction from the particle to the point of interest, is characterized by the angle θ which it makes with the direction of propagation of the incident light ($\hat{e}_i$) and the azimuth angle φ. The unit vectors $\hat{e}_r$ and $\hat{e}_z$ form the scattering plane.

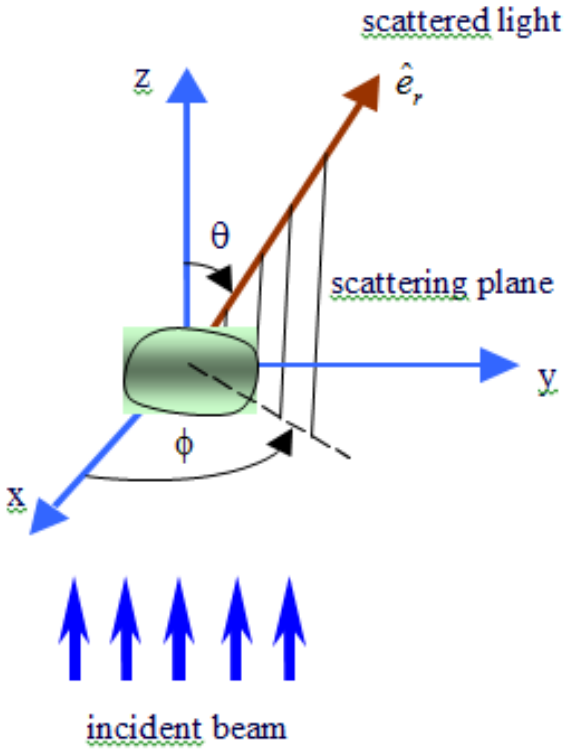

Figure 3.1: Configuration of light scattering from an arbitrary particle. The incident field is a plane EM wave.

The incident beam of light is represented by a harmonically oscillating plane EM wave that propagates in a vacuum without a change in its intensity or polarization state. This wave is described by [54]:

$$\vec{E}_i(\vec{r},t) = \vec{E}_0 \exp(i\vec{k}\cdot\vec{r} - i\omega t)$$
$$\vec{H}_i(\vec{r},t) = \vec{H}_0 \exp(i\vec{k}\cdot\vec{r} - i\omega t) \tag{3.1}$$

where $\vec{E}_i$ is the incident electric field, $\vec{H}_i$ is the incident magnetic field, $\vec{E}_0$ and $\vec{H}_0$ are constant vectors, $k = 2\pi/\lambda$ is the wavenumber, λ is the wavelength of the incident light, ω is the frequency, and *t* is time.

The incident field propagates unchanged through a medium that is unbounded, homogeneous, linear, isotropic, and nonabsorbing [55]. However, the presence of an object with a refractive index different from that of the surrounding medium changes the EM field. The EM field scattered by the object, ($\vec{E}_s$, $\vec{H}_s$), is the difference of the total field in the presence of the object, ($\vec{E}$, $\vec{H}$), and the original field, ($\vec{E}_i$, $\vec{H}_i$), that would exist in the absence of the object [54]:

$$\begin{aligned} \vec{E}_s &= \vec{E} - \vec{E}_i \\ \vec{H}_s &= \vec{H} - \vec{H}_i \end{aligned}. \tag{3.2}$$

The total fields must satisfy Maxwell's equations [56]:

$$\begin{aligned} \nabla \cdot \vec{D} &= 0 \\ \nabla \cdot \vec{B} &= 0 \\ \nabla \times \vec{E} &= -\frac{\partial \vec{B}}{\partial t}, \\ \nabla \times \vec{H} &= \frac{\partial \vec{D}}{\partial t} \end{aligned} \tag{3.3}$$

where $\vec{D} = \varepsilon(\vec{r})\vec{E}$ is the electric displacement, $\varepsilon(\vec{r})$ is the electric permittivity with spatial variation, $\vec{B} = \mu_0 \vec{H}$ is the magnetic induction, and μ_0 is the magnetic permeability of free space. From Maxwell's equations, it is straightforward to obtain the inhomogeneous Helmholtz wave equation for $\vec{E}$ [56]:

$$\nabla^2\vec{E}(\vec{r},\omega)-k^2\vec{E}(\vec{r},\omega)=-4\pi\vec{f}(\vec{r},\omega)$$
$$\vec{f}(\vec{r},\omega)=\frac{1}{4\pi}\left[k^2\left(\frac{\varepsilon(\vec{r})}{\varepsilon_0}-1\right)\vec{E}(\vec{r},\omega)+\nabla\left(\frac{\vec{E}(\vec{r},\omega)}{\varepsilon(\vec{r})}\cdot\nabla\varepsilon(\vec{r})\right)\right], \tag{3.4}$$

where $k^2=\mu_0\omega^2\varepsilon_o$ and ε_o is the permittivity of free space. The solution for $\vec{E}$ has the form [56]:

$$\vec{E}(\vec{r},\omega)=\vec{E}_{inc}(\vec{r},\omega)+\int_V\vec{f}(\vec{r}',\omega)G(\vec{r},\vec{r}',\omega)d^3\vec{r}'$$
$$G(\vec{r},\vec{r}',\omega)=\frac{e^{ik|\vec{r}-\vec{r}'|}}{|\vec{r}-\vec{r}'|}\quad, \tag{3.5}$$

where *V* is the region occupied by the scattering particle and *G* is the Green's function. The second term is the scattered field, and in the far field approximation it becomes [56]:

$$\vec{E}_s(\vec{r},\omega)=\frac{e^{ikr}}{\vec{r}}\int_V\vec{f}(\vec{r}',\omega)e^{-ik\hat{r}\cdot\vec{r}'}d^3\vec{r}'\,. \tag{3.6}$$

In the equation above, the function $\vec{f}(\vec{r}',\omega)$ is integrated over the volume of the scatterer. Since $\vec{f}(\vec{r}',\omega)$ is a function of electric field according to Eq. (3.4), it is apparent that the internal field must be known in order to solve for the scattered field.

For a selective group of highly symmetric scatterers, analytical solutions for the scattering field may be obtained using methods such as Mie theory and the T-matrix method. Both Mie theory and the T-matrix method solve Maxwell's equations by expanding the fields with spherical harmonics. Mie theory provides a solution for homogeneous spheres or concentric homogeneous spheres [52] while the T-matrix method can be applied to nonspherical particles with rotational symmetry such as spheroids [57]. Although these methods are fast and accurate, they are not adequate to describe light scattering from biological cells, which are asymmetric and

have an inhomogeneous spatial distribution in their refractive index [58]. To simulate light scattering from biological cells, numerical methods rather than analytical methods must be employed.

A popular numerical method is the Finite-Difference Time-Domain (FDTD) technique introduced by Yee in 1966. The FDTD technique discretizes Maxwell's time-dependent curl equations by using central-difference approximations for the space and time partial derivatives of the electric and magnetic fields [59]. The scattering particle is placed in a finite computational domain and the technique uses absorbing boundary conditions to model scattering in open space and a marching-in-time procedure to track the evolution of the fields from their initial values [60]. The field values at the previous and current time steps, specified at each grid point, are used to calculate the values at the next time step, so the method avoids solving a large system of linear equations and the memory storage requirement is proportional to the total number of grid points [60]. The FDTD method only solves for the near field, so a near-zone to far-zone transformation must be invoked to obtain the far field in the frequency domain. Because it is conceptually simple and easy to implement, the FDTD method is a very popular method [60].

Another popular numerical method is the discrete dipole approximation (DDA), proposed by Purcell and Pennypacker in 1973. This method discretizes the volume-integral equation for the electric field in the frequency domain [52]. It is based on computing the mutual interactions of N dipoles on a 3D lattice and requires the solution of a system of $3N$ complex linear equations [58]. Although the DDA method has not been used as extensively as the FDTD method to simulate light scattering from cells, a systematic study of two implementations of the methods showed that the DDA performance is superior for scatterers with relatively large size parameters [62].

For this reason, the DDA method is used in this project. A more detailed description of the DDA method is provided in §4.1.

3.2. Polarization properties of the scattered field

The scattered field depends not only on the intensity but also on the polarization of the incident field. As shown in Figure 3.2, the incident and scattered electric fields can be expressed as linearly polarized waves with components parallel ($E_{\|}$) and perpendicular ($E_{\perp}$) to the scattering plane:

$$\begin{aligned} \vec{E}_i &= E_{\|i}\hat{e}_{\|i} + E_{\perp i}\hat{e}_{\perp i} \\ \vec{E}_s &= E_{\|s}\hat{e}_{\|s} + E_{\perp s}\hat{e}_{\perp s} \end{aligned}, \tag{3.7}$$

where, $\hat{e}_{\|}$ and $\hat{e}_{\perp}$ are orthonormal basis vectors for the scattered and incident fields. As shown in Eq. (3.7), the amplitude of the scattered field is a linear function of the amplitude of the incident field. This relation is more conveniently expressed in matrix form [54]:

$$\begin{pmatrix} E_{\|s} \\ E_{\perp s} \end{pmatrix} = \frac{e^{ik(r-z)}}{-ikr} \begin{pmatrix} S_2 & S_3 \\ S_4 & S_1 \end{pmatrix} \begin{pmatrix} E_{\|i} \\ E_{\perp i} \end{pmatrix}, \tag{3.8}$$

where *S* is the amplitude scattering matrix.

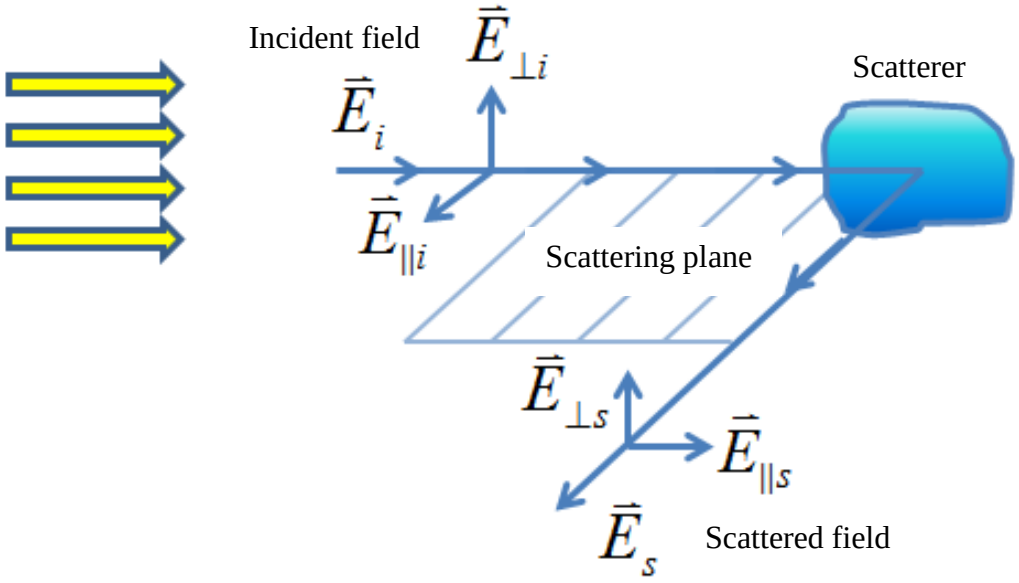

Figure 3.2: The polarization states of the incident and scattered field, measured relative to the scattering plane.

The incident and scattered waves can also be described with the real-valued Stokes parameters, which can be calculated directly from experimental measurements. These parameters are *I*, *Q*, *U* and *V*, where *I* is the total intensity (flow of energy per unit area) of radiation, *Q* is polarization at 0° or 90° to the scattering plane, *U* is polarization at $\pm 45^\circ$ to the scattering plane, and *V* is left or right circular polarization [63]. The Stokes vectors are related to the electric field vectors:

$$\begin{aligned} I &= \left\langle E_{\|}E_{\|}^{*} + E_{\perp}E_{\perp}^{*} \right\rangle \\ Q &= \left\langle E_{\|}E_{\|}^{*} - E_{\perp}E_{\perp}^{*} \right\rangle \\ U &= \left\langle E_{\|}E_{\perp}^{*} + E_{\perp}E_{\|}^{*} \right\rangle \\ V &= \left\langle i\left(E_{\|}E_{\perp}^{*} - E_{\perp}E_{\|}^{*}\right) \right\rangle \end{aligned} , \tag{3.9}$$

where the brackets indicate time averages over time periods longer than the period of the wave. The incident Stokes vector is related to the transmitted vector with the following relation [54]:

$$\begin{pmatrix} I_s \\ Q_s \\ U_s \\ V_s \end{pmatrix} = \frac{1}{k^2 r^2} \begin{pmatrix} S_{11} & S_{12} & S_{13} & S_{14} \\ S_{21} & S_{22} & S_{23} & S_{24} \\ S_{31} & S_{32} & S_{33} & S_{34} \\ S_{41} & S_{42} & S_{43} & S_{44} \end{pmatrix} \begin{pmatrix} I_i \\ Q_i \\ U_i \\ V_i \end{pmatrix}, \tag{3.10}$$

where *i* and *s* stand for the incident and the scattered light, respectively, *k* is the wavenumber, *r* is the distance from the scatterer, and S_{ij}, the elements of the Mueller matrix, are a function of the scattering angle θ [64]. The Mueller matrix elements contain information about the size, shape, structure, and optical properties of the scatterer. For example, S_{11} is proportional to the intensity of the scattered light. The intensity of forward scattering ($\theta \sim 0^\circ$) depends mostly on the size of the cell. For slightly larger angles and backward scattering ($\theta = 180^\circ$) the nucleus has a greater role, while small organelles are responsible for scattering at side scattering angles ($\theta \sim 90^\circ$) [65]. S_{12} normalized to S_{11} represents the degree of linear polarization of the scattered light for polarized incident light [66]. The S_{34} element indicates how effectively the scatterer acts like a quarter wave plate because it connects 45° linear polarization with circular polarization, and it is also very sensitive to the size of the particle. For a single particle, only seven Mueller matrix elements are independent [67]. The number of non-zero elements and the degree of symmetry in the matrix depends on the symmetry of the scattering particle [68].

Since the light intensity is directly related to the Mueller matrix, the polarization properties of a particle can be characterized by its Mueller matrix elements. One can measure the Mueller matrix elements by illuminating a particle and analyzing the scattered light with various

combinations of linear polarizer orientations. For the incident beam, the linear polarizer can have a horizontal, vertical, or 45° orientation. For each of these three options, the scattered beam can have polarizations parallel or perpendicular to the scattering plane. The components of the Mueller matrix are related to the various polarization states of the incident and scattered light by:

$$\begin{aligned}
\frac{I_{\parallel\parallel}}{I_i} &= \frac{1}{2}\left(\left(S_{11}+S_{12}\right)+\left(S_{21}+S_{22}\right)\right)\\
\frac{I_{\parallel\perp}}{I_i} &= \frac{1}{2}\left(\left(S_{11}+S_{12}\right)-\left(S_{21}+S_{22}\right)\right)\\
\frac{I_{\perp\parallel}}{I_i} &= \frac{1}{2}\left(\left(S_{11}-S_{12}\right)-\left(S_{22}-S_{21}\right)\right)\\
\frac{I_{\perp\perp}}{I_i} &= \frac{1}{2}\left(\left(S_{11}-S_{12}\right)+\left(S_{22}-S_{21}\right)\right)\\
\frac{I_{45^\circ\parallel}}{I_i} &= \frac{1}{2}\left(\left(S_{11}+S_{21}\right)+\left(S_{13}+S_{23}\right)\right)\\
\frac{I_{45^\circ\perp}}{I_i} &= \frac{1}{2}\left(\left(S_{11}-S_{21}\right)+\left(S_{13}-S_{23}\right)\right)
\end{aligned}, \tag{3.11}$$

where the subscripts of I on the numerator indicate the polarization of the incident and scattered light, respectively. Thus, several experimental measurements must be made in order to determine all of the Mueller matrix elements and the polarization properties of a sample [68].

3.3. Optical properties of the scatterer

There are several measurable optical properties of the scatterer that can be obtained once the scattered field is known. The anisotropy factor and scattering cross sections can be calculated. The total amount of scattered light is described by the scattering cross section C_{sca} which is the

surface area onto which the scattered energy is incident upon, and can be expressed as a product of the scattering efficiency and the geometrical cross section of the particle [64]:

$$C_{sca} = \frac{1}{k^2} \int_{(4\pi)} S_{11} d\Omega \,. \tag{3.12}$$

The absorption cross section C_{abs} represents the area of the energy absorbed by the particle, and the extinction cross section corresponds to the energy removed from the original beam [67]:

$$C_{ext} = \frac{4\pi}{k^2} \mathrm{Re}\{S(0)\}, \tag{3.13}$$

where $S(0)$ is an element from Eq. (3.8). By conservation of energy, we have [31]:

$$C_{ext} = C_{sca} + C_{abs} \,. \tag{3.14}$$

The cross sections depend on both the orientation of the particle and the state of polarization of the incident light [67]. The anisotropy factor represents the forward-weightiness of scattering [69]. A value of 1 for the anisotropy factor indicates that all radiation is scattered in the forward direction, the value is 0 when the flux of scattered energy is equal in forward and backward hemispheres, and -1 for backward scattering [70].

CHAPTER 4: Light scattering simulations

The DDA is a powerful method to simulate light scattering from particles with large size parameters. In this research, the DDA method is used for all light scattering simulations. The first section introduces the physics of the DDA method. The second section discusses the implementation of the DDA method that is used for this study, ADDA. The final section examines the errors associated with ADDA for light scattering simulations for particles of size parameter similar to biological cells.

4.1. Discrete Dipole Approximation

The basic idea behind the DDA method is to divide a dielectric scatterer into *N* small volumes (called dipoles) which become polarizable. The *N* dipoles make up a simple cubic lattice of spacing $d_0 < \lambda/10$ and they are each exposed to the incident field as well as the field due to all the other dipoles. The electric field at each site *i* is $\vec{E}_i$ and the oscillating dipole moment is [71]:

$$\vec{P}_i = \alpha \vec{E}_i , \tag{4.1}$$

with complex polarizability α . Purcell and Pennypacker assigned the Clausius-Mossotti polarizability to each dipole:

$$\alpha^{CM} = \frac{3d^3}{4\pi} \frac{\varepsilon - 1}{\varepsilon + 2} . \tag{4.2}$$

where ε is the dielectric constant. However, as mentioned below, various radiative correction to the Clausius-Mossotti polarizability have been suggested.

Each dipole contributes an electric field at the site *i* given by the sum of the incident field and the field due to all the other dipoles [71]:

$$\vec{E}_i = \vec{E}_{inc} + \sum_{j \neq i} \frac{\exp(ikr_{ij})}{r_{ij}^3} \left[k^2 \left(\vec{r}_{ij} \times \vec{P}_j \right) \times \vec{r}_{ij} + \frac{\left(1 - ikr_{ij}\right)}{r_{ij}^2} \left(3\vec{P}_j \cdot \vec{r}_{ij} r_{ij} - r_{ij}^2 \vec{P}_j \right) \right], \tag{4.3}$$

where $\vec{r}_{ij}$ is a vector pointing from r_j to r_i and $r_{ij} = \left| \vec{r}_i - \vec{r}_j \right|$. The second term is often written as $\sum_{i \neq j} \vec{A}_{ij} \vec{P}_j$ and the matrix $\vec{A}_{ii} = \alpha_i^{-1}$ so that Eq. (4.3) becomes a single matrix equation [71]:

$$\tilde{A}\tilde{P} = \tilde{E}_{inc}, \tag{4.4}$$

where $\tilde{A}$ is a $3N \times 3N$ matrix and $\tilde{P}$ and $\tilde{E}_{inc}$ are $3N \times 1$ vectors. The scattering problem is reduced to finding the polarization that satisfies the system of equations shown in Eq. (4.4).

To solve for the polarization, Purcell and Penny Packer used an iterative method. Let $\vec{P}_j^{(l)}$ denote the value assigned to $\vec{P}_j$ after the *l*th iteration, then [71]:

$$\vec{P}_i^{(l+1)} = \eta \alpha \vec{E}_i^{(l+1)} + \left(1 - \eta\right) \vec{P}_i^{(l)}, \tag{4.5}$$

where η is a numerical factor set to 0.5 to improve convergence. Iteration begins by setting $\vec{P}_i^{(0)} = 0$. The computing time is proportional to N^2 and convergence is slower for larger values of ε and $\frac{2\pi r_e}{\lambda}$, where the equivalent radius $r_e = \left(3N / 4\pi\right)^{1/3}$ [71].

4.2. ADDA

There are several numerical implementations of the DDA method, the most popular being the DDSCAT and ADDA codes. The various implementations of DDA differ in their discretization of the scatterer, their assignment of the polarizability for each dipole, and in the convergence criteria used for the iteration in the solution for the polarization. DDSCAT is a FORTRAN implementation of DDA made publicly available by Draine and Flatau in 1994 [72]. ADDA [73] is a C implementation of the DDA method developed by Yurkin and Hoekstra which can run on multiple processors using Message Passing Interface (MPI). Since its origin in Amsterdam in 1990, it has evolved into an open-source international project. Due to its accessibility and ability to simulate light scattering from particles with large size parameters, the ADDA implementation was used in all of our light scattering simulations.

The DDA method is very flexible with regards to the geometry of the scatterer, being limited only by the need to use a small dipole size d compared to the scatterer and the wavelength. ADDA uses the criteria [73]:

$$d = \lambda / 10|m|, \tag{4.6}$$

where m is the refractive index of the scatterer and satisfies [73]:

$$|m-1| < 2 \tag{4.7}$$

These requirements, based on simulations for spheres with size parameters smaller than 10, are expected to produce maximum errors in S_{11} on the order of 20-30% when compared to results of Mie theory [73].

The different implementations of DDA use different radiative reaction corrections to the Clausius-Mossotti polarizability. ADDA uses the lattice dispersion relation (LDR) correction as the polarizability option [73]:

$$\alpha^{LDR} = \frac{\alpha^{CM}}{1-\left(\alpha^{CM}/d^3\right)\left[\left(b_1^{LDR}+b_2^{LDR}m^2+b_3^{LDR}m^2S\right)(kd)^2+(2/3)i(kd)^3\right]}$$
$$b_1^{LDR}\approx 1.8915316, b_2^{LDR}\approx -0.1648469, b_3^{LDR}\approx 1.7700004 \quad , \qquad (4.8)$$
$$S=\sum_{\mu}\left(a_\mu e_\mu^0\right)^2$$

where α^{CM} is given in Eq. (4.2). This correction is based on finding the polarizability which produces the same dispersion relation for an infinite lattice of polarizable points as for a continuum of refractive index $m(\omega)$ [72].

There are various iterative methods used for the solution of the system of linear equations in Eq. (4.4) besides the method presented in the previous section. ADDA offers several iterative solvers, the default of which is the quasi-minimal residual method [74]. The default stopping criterion of the iterative method in ADDA is that the relative norm of the residual must be $<10^{-5}$ [73].

4.3. Consideration of errors in ADDA

When simulating light scattering with a numerical method such as DDA, there are discretization errors and shape errors due to representing particles with cubical dipoles. In order to minimize the errors, it is necessary to choose an adequate resolution for the scatterer, specified by the number of dipoles per wavelength (*dpl*). The common approach is to choose the *dpl* based on a comparison of ADDA results to those of Mie theory. Several tests have already been carried out for spheres with

various size parameters and refractive indices [62, 73]. In these tests, the accuracy criteria for S_{11} was for the RMS relative error of S_{11} over the whole range of θ to be less than 25%. It was shown that large *dpl* were required for particles with a relative index of refraction *m* close to one, but the tests were not carried out for the refractive index used in our studies.

We carried out similar simulations in order to determine the lowest *dpl* suitable for ADDA simulations of light scattering from spheres with properties similar to biological cells. We simulated light scattering by homogeneous spheres with $r = 5\mu m$ and $m = 1.03729$ using Mie theory and ADDA. A plane wave with λ=1.0 μm was assumed for the incident light. With ADDA, the simulations used a range of *dpl* from $4-26$. The relative error was computed for S_{11} while the absolute error was computed for $-S_{12}$, S_{33}, and S_{34}, which were all normalized by S_{11}.

In Figures 4.1-4.4, the Mueller matrix elements calculated with ADDA using *dpl* equal to 4, 8, 10, and 26 are presented and compared with exact results of Mie theory. The errors are much more pronounced in the larger scattering angles and in the deep minima, similar to the results in Ref. [73]. For S_{11} in the angular range that our studies are concerned with, mostly $\theta < 110^\circ$, the RMS relative errors are 149.2%, 16.4%, 6.1% and 0.9%, and the maximum relative errors are 1134.6%, 111.2%, 30.6% and 3.1%. Although larger *dpl* values resulted in smaller errors, the errors associated with a *dpl* equal to 10 were deemed acceptable. In addition, the large errors seen in Figures 4.1-4.4 are believed to be mostly due to shape errors and they are expected to be smaller for rough particles such as biological cells.

To test the effect of increasing the resolution of rough particles on the light scattering pattern, we also simulated light scattering from a sample Gaussian random sphere [see §6.2]. The parameters used for the Gaussian sphere were $\nu = 2.53$, $\sigma = 0.064$, $l_{\min} = 2$, and $l_{\max} = 50$. Since exact results

from this nonspherical scatterer are not available, the result obtained by ADDA with a *dpl* equal to 24 was used as a reference. The results for S_{11} are presented in

Figure 4.5 comparing a *dpl* equal to 4, 6, 8, and 10 to a *dpl* equal to 24. It can be seen that a *dpl* equal to 10 yields results much closer to the reference, with a RMS relative error of 28.9% over the whole range of θ.

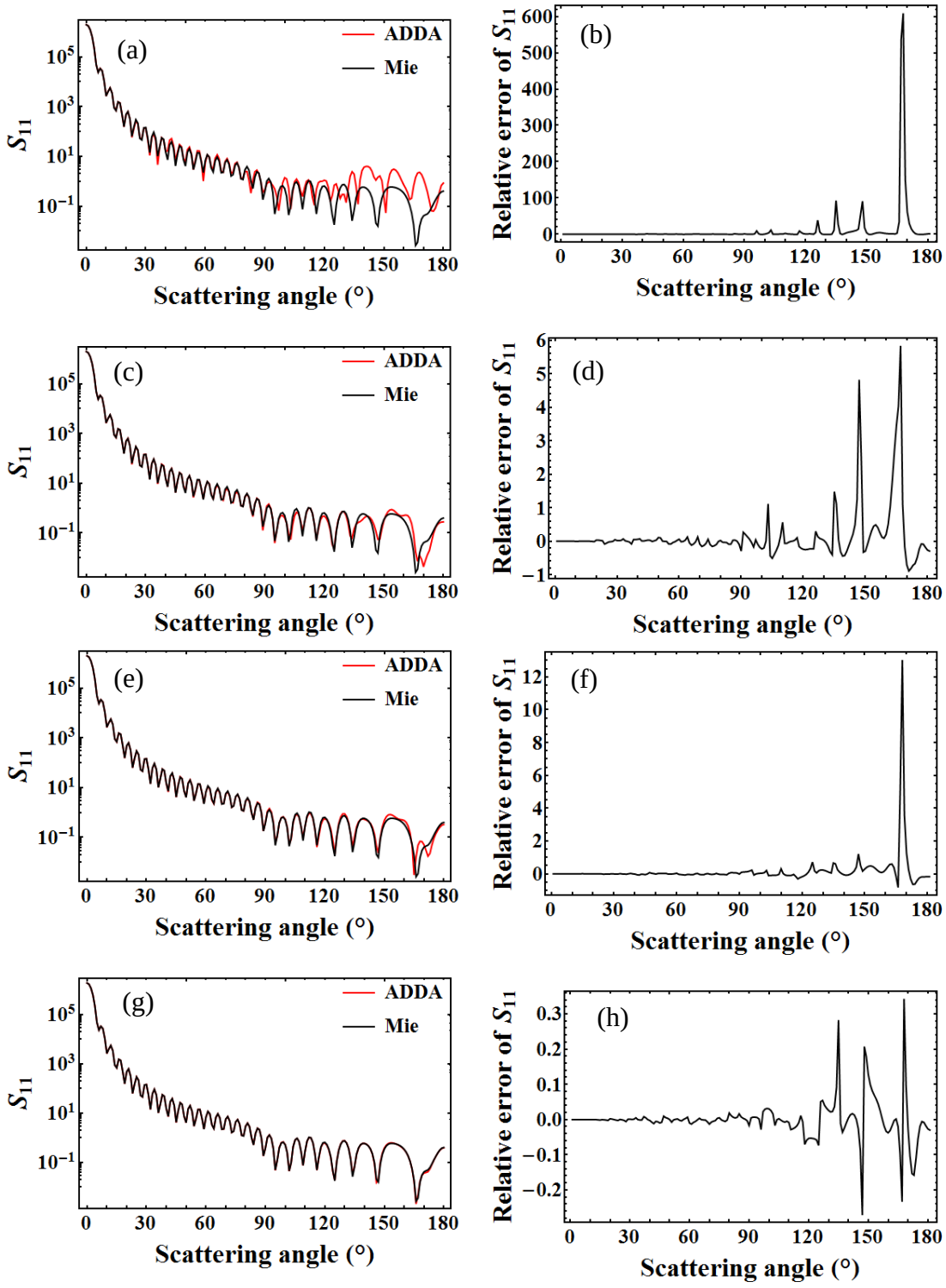

Figure 4.1: Comparison of S_{11} calculated by Mie theory and ADDA for a sphere of $r = 5.0\mu m$ and $m = 1.04$. (a) *dpl*=4, (c) *dpl*=8, (e) *dpl*=10, and (g) *dpl*=26. The relative errors are shown in (b), (d), (f), and (h), respectively.

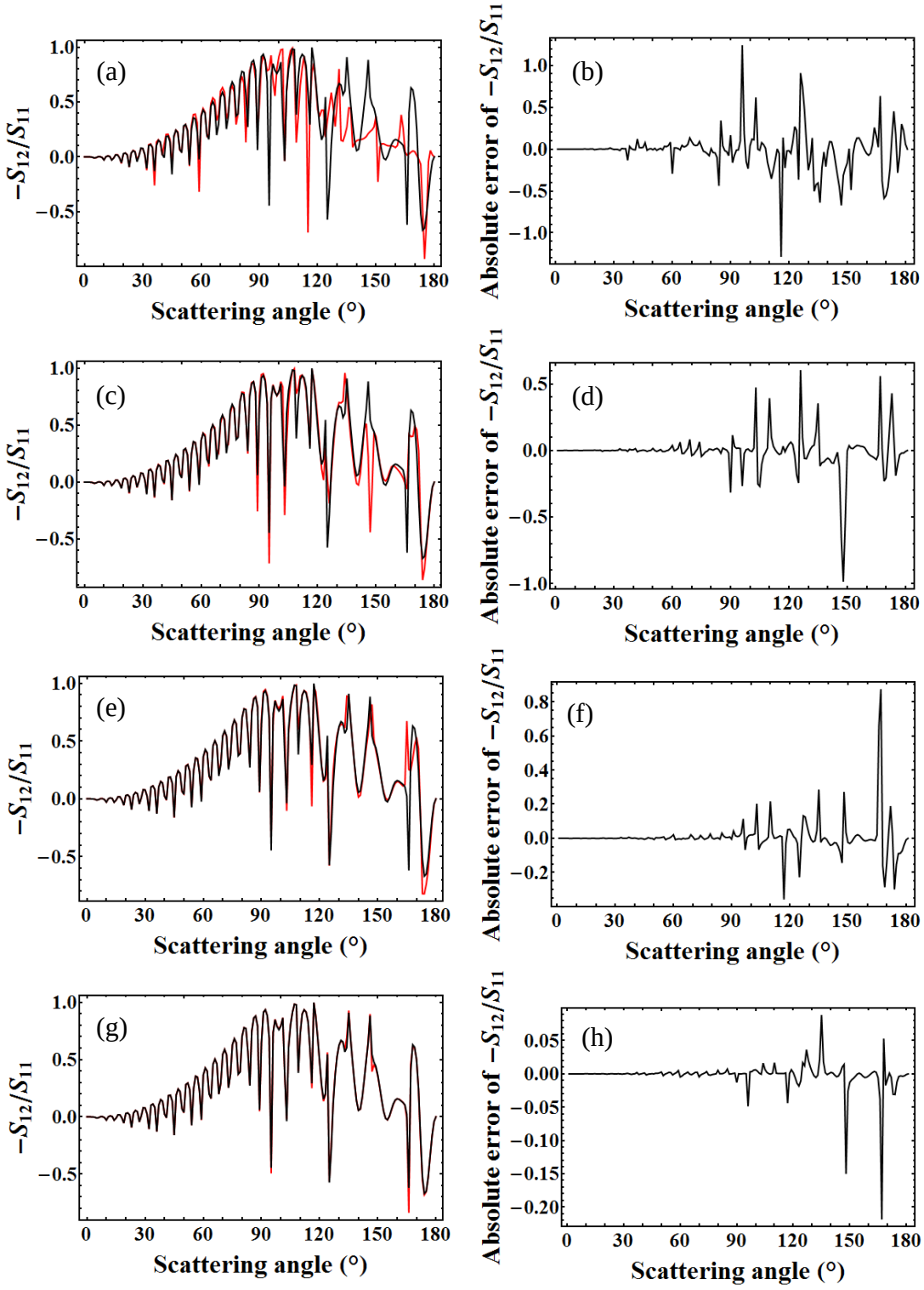

Figure 4.2: Comparison of $-S_{12}/S_{11}$ calculated by Mie theory and ADDA for a sphere of $r = 5.0\mu m$ and $m = 1.04$. (a) *dpl*=4, (c) *dpl*=8, (e) *dpl*=10, and (g) *dpl*=26. The absolute errors are shown in (b), (d), (f), and (h), respectively.

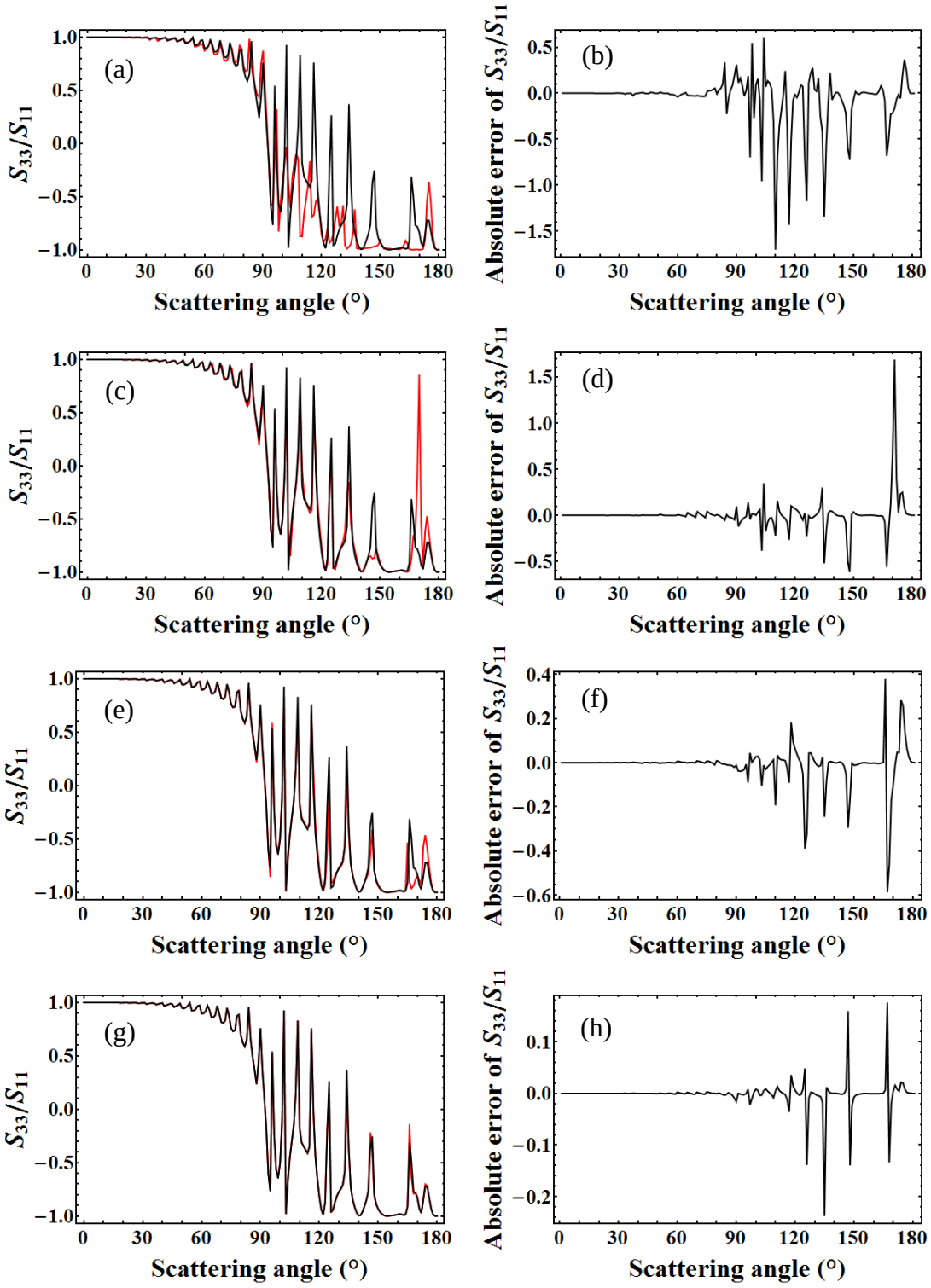

Figure 4.3: Comparison of S_{33}/S_{11} calculated by Mie theory and ADDA for a sphere of $r = 5.0\mu m$ and $m = 1.04$. (a) *dpl*=4, (c) *dpl*=8, (e) *dpl*=10, and (g) *dpl*=26. The absolute errors are shown in (b), (d), (f), and (h), respectively.

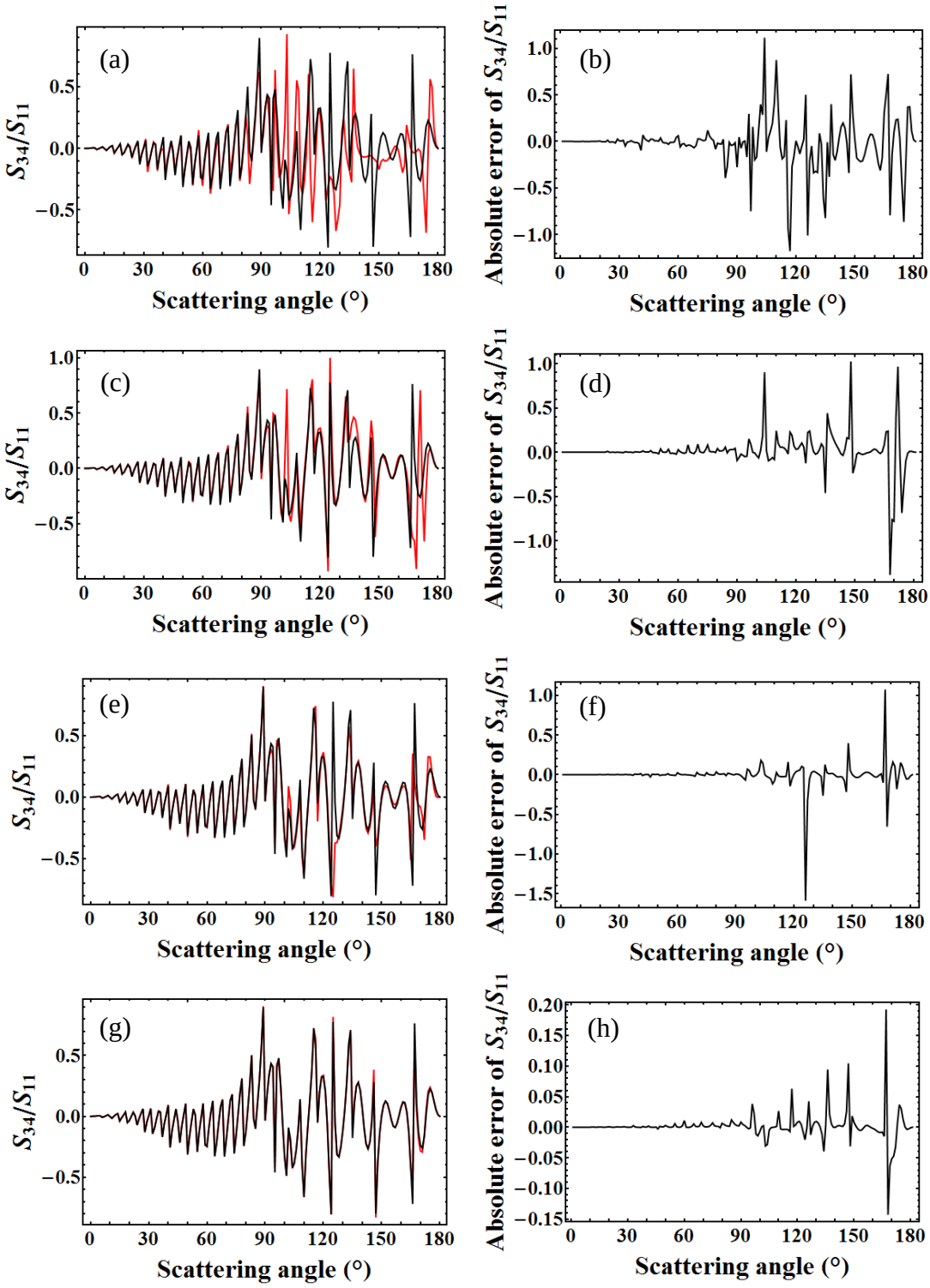

Figure 4.4: Comparison of S_{34}/S_{11} calculated by Mie theory and ADDA for a sphere of $r = 5.0\mu m$ and $m = 1.04$. (a) *dpl*=4, (c) *dpl*=8, (e) *dpl*=10, and (g) *dpl*=26. The absolute errors are shown in (b), (d), (f), and (h), respectively.

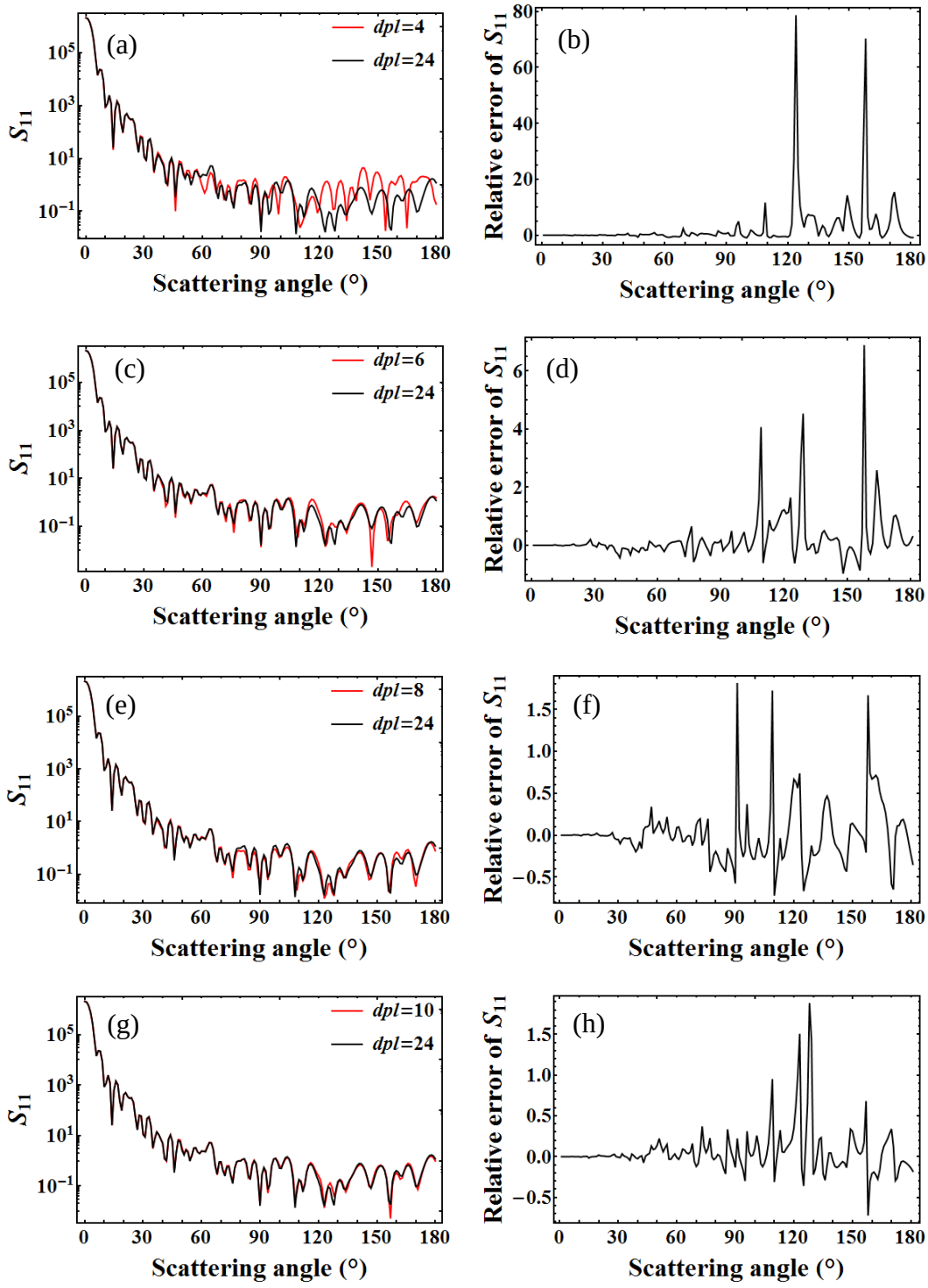

Figure 4.5: Comparison of S_{11} calculated by ADDA with *dpl*=24 and S_{11} calculated by ADDA with various *dpl* for a Gaussian sphere of $r = 5.0\mu m$ and $m = 1.04$. (a) *dpl*=4, (c) *dpl*=6, (e) *dpl*=8, and (g) *dpl*=10. The relative errors are shown in (b), (d), (f), and (h), respectively.

CHAPTER 5: LIGHT SCATTERING PATTERN ANALYSIS AND CLASSIFICATION

Analysis of the light scattering patterns from biological cells with texture analysis methods can provide information regarding the cell structure and its optical properties. Texture is one of the most important properties of images that has been studied at length over the past forty years for the purpose of content-based image retrieval, or grouping images based on certain characteristics. The first three sections describe three common image texture analysis methods: the Haralick features, Laws energy measures, and Gabor filters. The last section provides a description of discriminant analysis, a method used in multivariate analysis for classification purposes.

5.1. Haralick features

Haralick et al. were major contributors in defining textural features used to differentiate between images [24]. The fourteen Haralick texture features provide information such as homogeneity, contrast, and structure of the image. They are derived from co-occurrence matrices, which describe the frequencies of certain gray tones appearing in a specified spatial relationship in an image.

For an image of n gray tone values, the co-occurrence matrix is an nxn matrix whose values p_{ij} stand for the number of times a pixel with value i is found within a certain distance d to a pixel with value j. The distance between pixels can be defined horizontally, vertically, or diagonally ($\alpha = 0^\circ, 90^\circ, 45^\circ$, and 135°), resulting in four co-occurrence matrices that can be computed for a specified distance between pixels [24]. A distance $d = 1$ corresponds to the nearest neighbor to a pixel, as shown in Figure 5.1(a) for the four angles. For example, consider the image in Figure 5.1(b) that has four gray level values, ranging from 0 to 3. The co-

occurrence matrix with $d = 1$ and $\alpha = 45^\circ$ is a 4x4 matrix, shown in Figure 5.1(c), where the first row and column are shown to represent the gray level values of the original image. Thus, the top left value of this matrix corresponds to the six instances of two pixels each with value 0 being diagonal ($\alpha = 45^\circ$) nearest neighbors. The co-occurrence matrix is often normalized by the total number of pairs used in the matrix so that it approximates the probability densities of co-occurring gray levels [75]. The resulting co-occurrence matrix is shown in Figure 5.1(d). The four matrices computed (for each angle α) are often averaged to make the method rotationally invariant. It is from this final matrix that the fourteen Haralick textural features are extracted. For a list of the fourteen Haralick features, the reader is referred to Ref. [24].

(a) 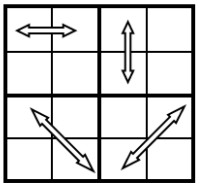

(b)

0	0	1	1	2
0	0	1	2	2
1	1	1	1	0
3	2	1	0	0
3	1	1	0	0

(c)

	0	1	2	3
0	6	3	0	0
1	3	8	3	1
2	0	3	2	1
3	0	1	1	0

(d)

.19	.09	0	0
.09	.25	.09	.03
0	.09	.06	.03
0	.03	.03	0

Figure 5.1: Calculation of the co-occurrence matrix. (a) The four angles for which the distance between pixels can be computed (clockwise from top left, $\alpha = 0^\circ, 90^\circ, 45^\circ$, and 135°). (b) A sample image with four gray level values. (c) The co-occurrence matrix with $d = 1$ and $\alpha = 45^\circ$ for the image in (b). (d) The normalized co-occurrence matrix.

Certain features have a clear physical meaning. For example, the angular second moment measures the homogeneity of the image. In a homogeneous image, there are very few dominant gray-tone transitions. Thus, the co-occurrence matrix for this image will consist of a few entries of large magnitude. On the other hand, a less homogeneous image with various types of transitions between pixels will result in a matrix with a large number of smaller entries, resulting

in a smaller angular second moment value [24]. The contrast is a difference moment of the matrix and measures the amount of local variations present in an image. An image with a large amount of local variation has a higher contrast value. The correlation measures gray-tone linear-dependencies in the image. An image consisting of mostly constant gray-tone values with some noise will have a lower correlation value than image displaying linear structure [24].

5.2. Laws measures

The Laws energy measures are derived from 2D filter masks and have various functions such as detecting edges, spots, and ripples in an image. The Laws filter masks are convolutions of specific vectors of orders three, five, or seven. The set of one-dimensional vectors of order three is displayed in Figure 5.2 (a). The vectors within a set are convoluted with each other to form sets of 9, 25, or 49 independent 2D filter masks. The convolution can be considered a cross product or vector multiplication operation. An illustration of the convolution of the *E3* and *L3* vectors resulting in the *E3L3* filter mask is shown in Figure 5.2 (b).

(a) $L3 = [1 \quad 2 \quad 1]$

$E3 = [-1 \quad 0 \quad 1]$

$S3 = [-1 \quad 2 \quad -1]$

(b) $$E3L3 = \begin{bmatrix} E(1)*L(1) & E(1)*L(2) & E(1)*L(3) \\ E(2)*L(1) & E(2)*L(2) & E(2)*L(3) \\ E(3)*L(1) & E(3)*L(2) & E(3)*L(3) \end{bmatrix} = \begin{bmatrix} 1 & 0 & -1 \\ 0 & 0 & 0 \\ -1 & 0 & 1 \end{bmatrix}$$

(c)

0	0	1	1	2
0	0	1	2	2
1	1	1	1	0
3	2	1	0	0
3	1	1	0	0

×

1	0	-1	
0	0	0	
-1	0	1	

=

		-4		

Figure 5.2: Laws filter masks. (a) The set of Laws vectors of order three. (b) The convolution of *E3* and *L3* vectors. (c) Filtering an image with the E3L3 Laws filter mask.

The first step in extracting textural information using Laws masks is to filter an image using each 2D filter. Each pixel in the filtered image is equal to the sum of the original pixel and its surrounding pixels each multiplied by the corresponding filter values. An example of an image filtered with the *E3L3* filter mask is illustrated in Figure 5.2(c). Once a filtered image is obtained, the absolute value in local neighborhoods (~15 pixels) around each pixel of the filtered image is summed to yield a set of 25 texture energy measures (TEM). This is represented by the following equation:

$$TEM\left(x,y\right)=\sum_{i=-7}^{7}\sum_{j=-7}^{7}\left|I\left(x+i,y+j\right)\right|. \tag{5.1}$$

The energy measures are often normalized for contrast with the *L5L5* TEM image, which is not used further in the analysis. To extract texture information from the filtered image, the variance or standard deviation alone is sufficient [25].

Like the Haralick features, each Laws mask serves a particular purpose. The vectors in each set are named using mnemonics which give some indication of the function of each mask: Level, Edge, Spot, Wave, Ripple, Undulation, or Oscillation. For example, the Level vector gives a center-weighted local average, the Edge vector responds to row or column step edges, and the Spot and Ripple vectors detect spots and ripples, respectively [76]. Laws described the four most important 5x5 masks: "*E5L5* is a horizontal edge mask, enhancing horizontal structure; R5R5 is a high-frequency spot detector; *E5S5* is a peculiar V-shaped mask which responds best to textures with low correlation; *L5S5* is a vertical line detector, enhancing vertical edges" [25].

5.3. Gabor filters

Gabor filters have proved very useful for texture classification and image recognition. Gabor filters can be viewed as complex sinusoidal signals of particular frequency and orientation modulated by a Gaussian envelope. They were originally introduced by Dennis Gabor in 1946 [77]. In the following description of Gabor filters, we use the notation by Manjunath [78].

Gabor filters are obtained by dilations and rotations of the wavelet $\psi(x, y)$:

$$\psi(x, y) = \frac{1}{2\pi\sigma_x\sigma_y} \exp\left[-\frac{1}{2}\left(\frac{x^2}{\sigma_x^2} + \frac{y^2}{\sigma_y^2}\right)\right] \cdot \exp\left[2\pi jWx\right], \tag{5.2}$$

where σ_x and σ_y are the standard deviations which determine the width of the Gaussian, and W is the modulation frequency. The Gabor filters are obtained through the generating function

$$\psi_{mn}(x, y) = a^{-m}\psi(\tilde{x}_n, \tilde{y}_n), \tag{5.3}$$

where $\psi_{mn}(x, y)$ are the Gabor filters for each scale m and orientation n, with $m=0,1,...M-1$, $n=0,1,...N-1$, where M is the number of scales and N is the number of orientations. By applying the generating function, a Gabor filter is thus given by:

$$\psi_{mn}(x, y) = \frac{1}{2\pi\sigma_{x,m}\sigma_{y,m}} a^{-m} \exp\left[-\frac{1}{2}\left(\frac{\tilde{x}_n^2}{\sigma_{x,m}^2} + \frac{\tilde{y}_n^2}{\sigma_{y,m}^2}\right)\right] \cdot \exp\left[2\pi jW_m\tilde{x}_n\right], \tag{5.4}$$

where the variables in the equation are defined as follows:

$$
\begin{aligned}
\tilde{x}_n &= \left(x\cos\theta_n + y\sin\theta_n\right) \\
\tilde{y}_n &= \left(-x\sin\theta_n + y\cos\theta_n\right) \\
\theta_n &= \frac{n\pi}{N} \\
a &= \left(\frac{U_h}{U_l}\right)^{\frac{1}{M-1}} \\
W_m &= a^m U_l \\
\sigma_{x,m} &= \frac{\left(a+1\right)\sqrt{2\ln 2}}{2\pi\left(a-1\right)W_m} \\
\sigma_{y,m} &= \frac{1}{2\pi\tan\left(\frac{\pi}{2N}\right)\left[\frac{W_m^2}{2\ln 2} - \left(\frac{1}{4\pi^2\sigma_{x,m}^2}\right)\right]^{1/2}},
\end{aligned}
\tag{5.5}
$$

To reduce the redundancy due to the nonorthogonality of the Gabor wavelets, Manjunath has designed the filter bank by ensuring that the half-peak magnitude support of the filter responses in the frequency spectrum touch each other. This leads to the notation presented above, in contrast to the common notation by Daugman, who extended the Gabor filter to two dimensions [79].

With the Manjunath notation, a filter is defined by the constants U_l, U_h, M, and N, where the lower and upper frequencies U_l and U_h are constants, specifying the range of frequencies for the filter bank. For an image I(x,y), a 2-D Gabor transform is localized in space and frequency and is given by:

$$
G_{mn}\left(x,y\right) = \sum_s \sum_t I\left(x-s, y-t\right)\psi_{mn}^*\left(s,t\right), \tag{5.6}
$$

where *s* and *t* are the filter mask size variables and ψ^*_{mn} is the complex conjugate of ψ_{mn}. The mean and standard deviations of the Gabor transforms are often used in feature vectors that help distinguish the textures of images [80].

Figure 5.3 shows an image with horizontal and vertical stripes filtered with a Gabor filter with orientation of 90° and frequency equal to that of the stripes. Since the filter has horizontal stripes, it emphasizes the horizontal stripes in the image.

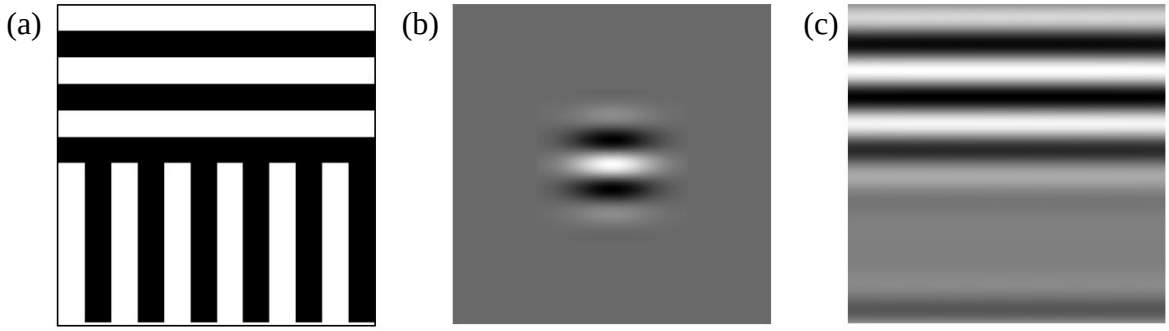

Figure 5.3: Example of Gabor filtering. (a) A sample image with horizontal and vertical stripes. (b) A Gabor filter with orientation of 90° and same frequency as (a). (c) The Gabor-filtered image.

5.4. Discriminant analysis

Discriminant Function Analysis (DFA) is a standard technique that allows one to classify objects or individuals based on a set of measurements on those objects or individuals. Usually the categories of membership (groups) are known ahead of time and the goal is to accurately predict from the measurements the groups to which individuals belong. In order to classify individuals to groups, DFA attempts to find differences in the groups based on the multivariate measurements that define the groups. Specifically, DFA attempts to find linear combinations of the measurements that maximize the test statistics comparing the groups.

The data for DFA usually consists of random samples from *m* different groups and values for *p* independent variables $X_1, X_2, \ldots, X_p$. There are *n* values available for each of the *p* variables. The sample covariance between variables X_j and X_k is given by [81]:

$$c_{jk} = \sum_{i=1}^{n} \left(x_{ij} - \bar{x}_j \right) \left(x_{jk} - \bar{x}_k \right) \Big/ \left(n - 1 \right), \tag{5.7}$$

where x_{ij} is the value for the ith observation of variable X_j and $\bar{x}_j$ is the sample mean for X_j. The main assumptions in DFA are that the variables are normally distributed in each group and that the covariances of the variables in each group are equal.

The number of linear discriminant functions required to discriminate between the *m* groups is the minimum of *p* and *m*-1. The linear discriminant functions (LDF) are given by [81]:

$$Z_i = \sum_{k=i}^{p} a_{ik} X_k + c_i \,, \tag{5.8}$$

where c_i is a constant. The approach is to find the coefficients a_{ik} such that an analysis of variance (ANOVA) comparing the groups on the new variable Z_i has the maximum F-ratio value. The F-ratio is the ratio of the between-groups to the within-groups estimate of variance [81]:

$$F = \frac{B/(m-1)}{W/(n-m)}, \tag{5.9}$$

where $B = T - W$, $W = \sum_{j=1}^{m}\sum_{i=1}^{n_j}\left(z_{ij} - \bar{z}_j\right)^2$, and $T = \sum_{j=1}^{m}\sum_{i=1}^{n_j}\left(z_{ij} - \bar{z}\right)^2$. The first LDF reflects group differences as much as possible, and the rest of the LDFs are subject to the condition that the Z_i are uncorrelated [81].

If individuals are correctly assigned to groups based on a set of measurements, then a set of objects with unknown groupings may be assigned to groups based on their distances from the groups. One method for assessing statistical distance is the Mahalonobis Distance. This distance is computed from an observation $\mathbf{x} = \left(x_1, x_2, ..., x_p\right)$ to the center of each group *i* as follows [81]:

$$D_i^2 = \left(\mathbf{x} - \bar{\mathbf{x}}_i\right)' \mathbf{C}^{-1} \left(\mathbf{x} - \bar{\mathbf{x}}_i\right), \tag{5.10}$$

where $\mathbf{C}^{-1}$ is the inverse covariance matrix and $\bar{\mathbf{x}}_i = \left(\bar{x}_{1i}, \bar{x}_{2i}, ..., \bar{x}_{pi}\right)$ denotes the vector of mean values for the sample from the i^{th} group. The observation is assigned to the group with the smallest distance. The percentage of correct allocations is an indication of how well groups can be separated using the available variables. A good indicator of the predictive power of a model is the cross-validated classification value, which is found by allocating each individual to its group without using that individual to determine the group center. For a discriminant analysis, it

is generally recommended that the number of individuals is at least ten to twenty times greater than the number of independent variables and that there are at least 20 individuals per group.

CHAPTER 6: ANALYTICAL CELL MODELING

This chapter presents an analytical method to model the structure of biological cells. Since most of the cell and nucleus shapes possess characteristics of a deformed ellipsoid, the 3D modeling is divided into two main steps: the base shape is fitted with an ellipsoid and then surface fluctuation is introduced using the Gaussian sphere model. The method presented here to obtain the overall shape of biological cells is based on Ref. [82], in which the authors combined an ellipsoid and Gaussian sphere model to represent potato tubers.

The first section describes the modeling of the base shape of the cells using information extracted from confocal images of biological cells. The second section provides an introduction to the Gaussian sphere model which is used in the third section to describe the surface fluctuation of the cell. The fourth section presents a validation of the procedure to extract the surface fluctuation parameters. The fifth section describes the modeling of cellular organelles, including nuclear substructures and the mitochondria. The final section describes the selection of the parameters used to create the cell models. The parameters used in the cell models were based on the characteristics of lymphocytes as much as possible. They were either based on information available in the literature or derived from confocal images of cells.

6.1. Modeling the base shape

The overall shapes of the biological cell models are extracted from processed 2D confocal microscopic images of biological cells. Confocal images have already been used to obtain 3D structures of cells with nucleus and mitochondria [83, 15] and provide a convenient way to obtain the parameters necessary for analytical modeling of the surface shape. A stack of confocal images and processed images from Ref. [15] are shown in Figure 6.1 (a,b). From these

processed images, sets of points representing the contours of the cell and nucleus surfaces are obtained by selecting the cell points touching the surrounding medium and the nucleus points touching the cytoplasm, respectively. The set of points obtained from the processed stack of images is shown in Figure 6.1(c). These sets of points are not evenly spaced on the surfaces due to the pixelated nature of the processed images. To facilitate the description of the surfaces with the Gaussian sphere model, the surface points are interpolated on a set of 3612 equally-spaced points using bilinear interpolation. The equally-spaced points were generated using the program "Icosahedron" by Max Tegmark [83]. The radius of each point as a function of θ and φ is then determined, with each set of points centered at the center of mass of each surface. An example of a set of equally-spaced points obtained for the cell surface is shown in Figure 6.1(d).

The base shapes of the cell and nucleus are modeled with ellipsoids. In deriving the ellipsoidal base shape, each set of 3D points is fitted to an ellipsoid with principal axes lengths of *a*, *b*, and *c*. The orientation of the ellipsoid is specified by an angle γ rotated about a unit vector *u* in the x-y plane. The ellipsoid is rotated using a rotation matrix derived from Rodrigues' rotation formula,

$$R = \begin{bmatrix} \cos\gamma + u_x^2(1-\cos\gamma) & u_x u_y(1-\cos\gamma) & u_y \sin\gamma \\ u_y u_x(1-\cos\gamma) & \cos\gamma + u_y^2(1-\cos\gamma) & -u_x \sin\gamma \\ -u_y \sin\gamma & u_x \sin\gamma & \cos\gamma \end{bmatrix}, \tag{6.1}$$

where $u_x = \cos\phi$ and $u_y = \sin\phi$. The unit vector *u* is thus defined by the angle ϕ which it makes with the x-axis. The expression derived for the radius *r* of the ellipsoid is a function of the angles θ and φ in spherical coordinates and is provided in Appendix A. There are five parameters (*a, b, c,* γ and ϕ) required for this representation of an ellipsoid in any orientation in

3D space. To find the best-fit ellipsoid for the cell and nucleus, a linear least-squares fitting technique is applied, which involves finding $r_{ellipsoid}$ which minimizes the residual *res*:

$$res = \sum_{i=1}^{N} \left(r_{ell}(i) - r_{orig}(i) \right)^2 . \tag{6.2}$$

To minimize computation time, the surface points are first fitted to an ellipsoid without rotation to obtain the approximate size of the ellipsoid, and then the five parameters are fitted simultaneously.

The ratio of the radius of the cell surface to that of the ellipsoid is used to describe the level of deformation and fluctuation of the cell surface from the ellipsoidal base shape:

$$R(\theta,\phi) = \frac{r_{outline}(\theta,\phi)}{r_{ellipsoid}(\theta,\phi)} . \tag{6.3}$$

To allow for the modeling of a large group of differently-shaped cells with similar characteristics, a statistical approach can be used to model this ratio. For this study, the Gaussian random sphere geometry is adapted to model the statistical properties of the cell shapes. A statistical description of the Gaussian random sphere model is presented in the section below.

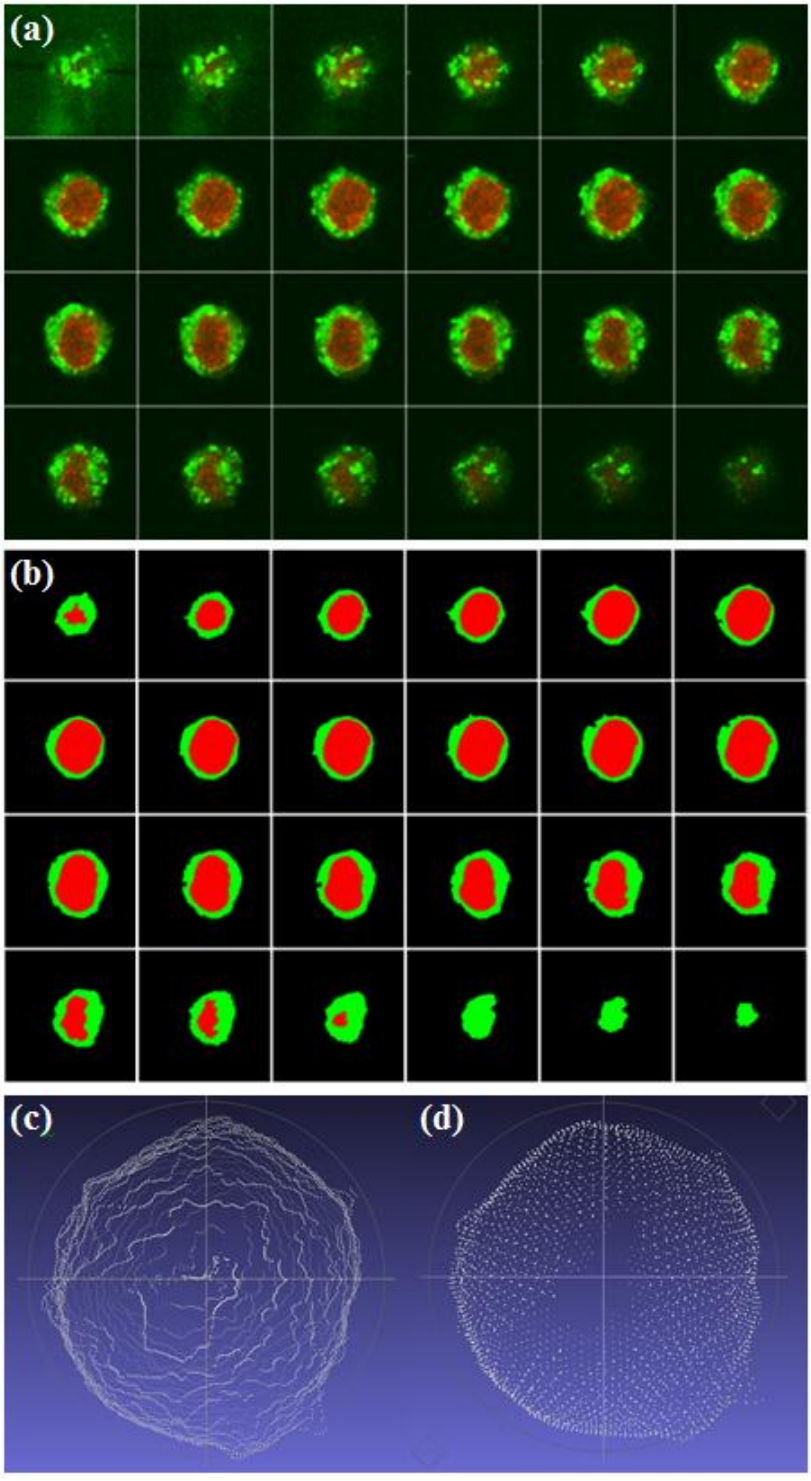

Figure 6.1: Illustration of procedure to obtain cell surface points. (a) A stack of confocal images from B-cell #8. (b) The processed images from the stack in (a). (c) The surface points obtained from the outlines in (b). (d) A set of 3612 equally-spaced points interpolated from those in (c). *Images in (a) and (b) courtesy of Scott R. Brock* [15].

6.2. Gaussian random sphere geometry

In 1996, Muinonen et al. introduced a stochastic shape model known as the Gaussian random sphere geometry that can be used to generate a statistically-related class of irregularly-shaped objects [84]. The Gaussian random sphere geometry has successfully been used to model a variety of objects, such as ice crystals [70], sand particles [69], asteroids, and comets [85], but it has not, to our knowledge, been used to model biological cells.

The radii $\vec{r} = r_N(\theta,\phi)$ of a Gaussian sphere are assumed to follow a multivariate lognormal distribution. The radii are related to the logradii, $s_N(\theta,\phi)$, through the relation [64]:

$$r(\theta,\phi)\hat{e}_r = \frac{\bar{r}\exp\left[s(\theta,\phi)\right]}{\sqrt{1+\sigma^2}}\hat{e}_r, \tag{6.4}$$

where $\bar{r}$ is the mean radius and σ is the relative standard deviation. The logradius naturally follow a multivariate lognormal distribution [86]:

$$f(\vec{s},\Sigma_s) = (2\pi)^{-N/2}\left|\Sigma_s\right|^{-1/2}\exp\left[-\frac{1}{2}\left(\vec{s}^T\Sigma_s^{-1}\vec{s}\right)\right], \tag{6.5}$$

where Σ_s is the covariance matrix of logradius. The logradius can be expanded in terms of spherical harmonics [64]:

$$s(\theta,\phi) = \sum_{l=0}^{\infty}\sum_{m=-l}^{l} s_{lm}Y_{lm}(\theta,\phi), \tag{6.6}$$

where Y_{lm} are the spherical harmonics. The weights s_{lm} are independent Gaussian random variables with zero means and variances. Single realizations of Gaussian spheres are generated by randomizing the weights s_{lm}.

The covariance function of logradius is related to the autocorrelation function through [70]:

$$\sum_s(\gamma) = \beta^2 C_s(\gamma), \tag{6.7}$$

where $C_s(\gamma)$ is the autocorrelation function, γ is the angular distance between two directions (θ_1, ϕ_1) and (θ_2, ϕ_2), and β is the standard deviation of logradius, which is related to the relative standard deviation through the relation:

$$\sigma^2 = \exp(\beta^2) - 1. \tag{6.8}$$

The autocorrelation function can be expanded with a Legendre series with coefficients c_l following a power law:

$$\begin{aligned} & C_s(\gamma) = \sum_{l=0}^{\infty} c_l P_l(\cos\gamma) \\ & c_l \propto l^{-\nu} \\ & \sum_{l=0}^{\infty} c_l = 1 \end{aligned} \quad . \tag{6.9}$$

The coefficients c_l are non-negative and directly related to the weights s_{lm} in Eq. (6.6) [70]. Combining Eqs.(6.9) and (6.9), the covariance function of logradius is obtained:

$$\sum_s(\gamma) = \beta^2 \sum_{l=0}^{\infty} c_l P_l(\cos\gamma) = \ln(\sigma^2 + 1) \sum_{l=l_{\min}}^{l_{\max}} l^{-\nu} P_l(\cos\gamma), \tag{6.10}$$

where the Legendre series has been truncated from the lowest order $l_{\min}$ to the highest order $l_{\max}$. According to the equation above, only a few parameters must be specified to describe a Gaussian sphere: the relative standard deviation σ, the power law coefficient ν, $l_{\min}$ and $l_{\max}$. Each parameter controls different aspects of the surface fluctuation. $l_{\min}$ controls the degree of deformation of the surface from a spherical shape and usually takes the value 2 or 3; ν controls the number of hills and valleys per solid angle, a lower value indicating higher spatial frequency of the fluctuation; $l_{\max}$ truncates the series without losing desired accuracy; and σ describes the range of the valley and hills radially. These parameters make the Gaussian random sphere model a convenient tool for generating an arbitrarily large collection of shapes with distinct but related geometries. A few examples of Gaussian spheres generated with different σ and ν values are shown in Figure 6.2(a-c). $l_{\min}$ and $l_{\max}$ are fixed at 3 and 50, respectively, for each Gaussian sphere. The Gaussian sphere in (a) has a large number of hills and valleys per solid angle but small radial variations, due to the small values of ν and σ. Figure 6.2 (b) displays a smoother Gaussian sphere compared to (a) due to the increase in ν from 1.7 to 3.5. In Figure 6.2 (c), σ increases from 0.06 to 0.09, resulting in much more deformation compared to (b).

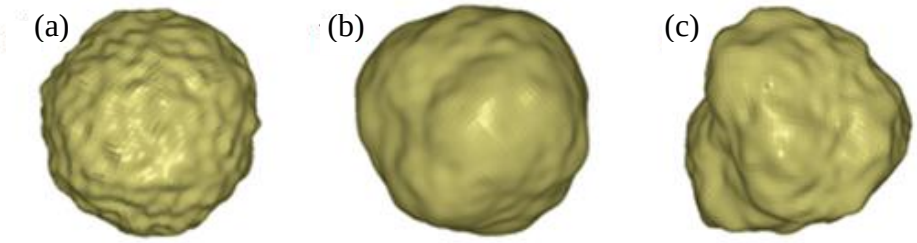

Figure 6.2: Examples of Gaussian random spheres with different values for ν and σ. (a) ν=1.7 and σ=0.06; (b) ν=3.5 and σ=0.06; (c) ν=3.6 and σ=0.09. $l_{\min}$ and $l_{\max}$ are fixed at 3 and 50, respectively, for all cases.

6.3. Modeling the surface fluctuation

To represent the surface fluctuation, the Gaussian sphere parameters mentioned above are extracted from the set of ratio points that describes the surface. First, the autocovariance function is calculated from the set of equally-spaced ratio points derived for each surface. The autocovariance function is a measure of the correlation properties of the surface roughness [87]. A high positive value for the function indicates that a surface feature will repeat itself for that particular lag length, and the value of the function for a lag length of zero is equal to the square of the Root Mean Square (RMS) roughness of the surface. The autocovariance as a function of solid angle is the average of the product of the radii deviations from the mean radius for each pair of points that have the solid angle between them:

$$\sum_r(\gamma) = \frac{1}{N_\gamma}\sum_{i=1}^{N_\gamma}\left(r_i - \bar{r}\right)\left(r_{i+\gamma} - \bar{r}\right), \tag{6.11}$$

where N_γ is the number of points that have an angular distance γ between them. Then, the relative standard deviation σ is calculated using the following expression:

$$\sigma = \frac{\sqrt{\frac{1}{N}\sum_{i=1}^{N}\left(r_i - \bar{r}\right)^2}}{\bar{r}}. \tag{6.12}$$

The covariance function of logradius is calculated using the relation:

$$\sum_s(\gamma) = \ln\left(\frac{\sum_r(\gamma)}{\bar{r}^2} + 1\right). \tag{6.13}$$

This function can be expressed as a Legendre polynomial series with a power law expansion as shown above in Eq. (6.10). Eq. (6.10) is used to obtain $l_{\min}$ and $l_{\max}$ using linear least-squares fitting. The parameters, σ, ν, $l_{\min}$, and $l_{\max}$ are then used to generate a Gaussian sphere representing the fluctuation of the surface radius from the base shape of the ellipsoid.

In order to obtain the radius of the final analytical surface shape model, it is necessary to multiply the radius of the base ellipsoid to the corresponding one of the Gaussian sphere. However, the orientation of the Gaussian sphere is arbitrary and the orientation of the Gaussian sphere that most closely resembles the original shape when multiplied by the ellipsoid must be determined. This orientation is found by comparing three perpendicular cross sections obtained from the surface points derived from the confocal images to three perpendicular cross sections obtained from the Gaussian sphere points. The Gaussian sphere is rotated and the orientation resulting in the greatest correlation between the two sets of cross sections is chosen. The final shape $r(\theta,\varphi)$ is obtained by multiplying the Gaussian sphere point by the ellipsoid for each θ and φ, and the 3D cell structure is formed by putting together the analytical surface models of the cell membrane and the nucleus.

6.4. Validation of surface fluctuation parameter extraction procedure

In the method described in the previous section to extract Gaussian sphere parameters from a closed surface, there are several options that affect the values of the recovered parameters. The calculation of the covariance function is affected by the number of points on the surface and the resolution of γ in the covariance function. Once the covariance function is calculated, the range of γ used to fit the covariance function and the method used to calculate the standard deviation

impact the recovered parameters. In this section, the procedure to determine these options in order to successfully extract parameters from a closed surface is described.

In order to determine the number of points on the surface and the resolution of γ in the covariance function required for successful recovery of the Gaussian sphere parameters, a Gaussian sphere (ν=3, σ=.05, $l_{\min}$=2, $l_{\max}$=50) was generated and interpolated onto three sets of approximately equally-spaced points. The Gaussian sphere had a resolution of 1.0° for the polar and azimuthal angles, while the three sets of points contained 3612, 15212, and 62412 points on the surface with an approximate solid angle γ between adjacent points of 3.2, 1.5 and 0.75° , respectively. For each pair of points on the surfaces, γ was calculated and rounded to the nearest 1.0, 3.0, or 5.0° to provide three resolutions for the covariance function, which was then calculated using Eq. (6.11) for $\gamma = 0 - 180^\circ$. The calculated covariance function was fitted using a linear least-squares fitting technique for four angular ranges: $\gamma = 0 - 45^\circ$, $\gamma = 0 - 90^\circ$, $\gamma = 90 - 180^\circ$, and $\gamma = 0 - 180^\circ$ to recover the parameters ν and $l_{\min}$. Figure 6.3 below shows the covariance functions calculated for Gaussian spheres with 3612, 15212, and 62412 equally-spaced points using a resolution of $\gamma = 1.0^\circ$ for the covariance function. Also shown is the analytical form of the covariance function given by Eq. (6.10) with $\nu = 3.0$, $l_{\min}$=2, and $l_{\max}$=50. The recovered covariance functions lie on top of each other, with more variations in the curve for the Gaussian spheres with fewer surface points due to the angle between adjacent points on the Gaussian spheres being larger than the resolution of the covariance function for those Gaussian spheres. The covariance functions calculated using a resolution of 3.0 and 5.0° are not shown because they are smooth and lie on top of the recovered covariance functions. It can also be seen in

Figure 6.3 that there is closer agreement between the actual and recovered covariance functions for smaller angles.

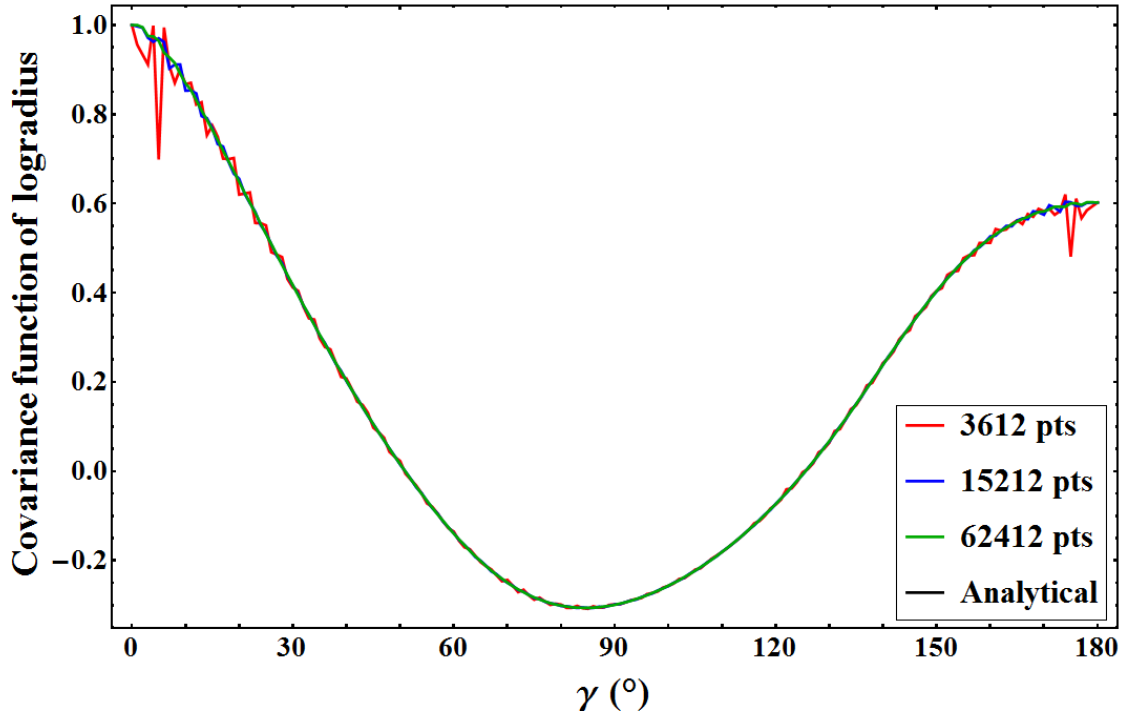

Figure 6.3: Comparison of covariance functions of logradius calculated from Gaussian spheres (ν=3, σ=0.05, l_{min}=2, l_{max}=50) to the analytical form given by Eq. (6.10) (black). The Gaussian spheres were generated with three different surface resolutions of 3612, 15212, and 62412 equally-spaced points, represented by red, blue, and green lines, respectively. The angular resolution for the covariance functions is 1.0°.

Based on the previous figure, it would seem that increasing the number of evenly-spaced points on the surface would improve the results especially when using a 1.0° resolution for the covariance function. However, the ν and l_{min} values recovered for the three surfaces were very similar regardless of the number of points on the surface or the resolution of the covariance function, although further tests (not shown) did reveal that reducing the number of points any further resulted in poorer results. Table 6.1 presents the average ν and l_{min} recovered when

fitting the covariance functions mentioned above with four angular ranges. The best parameters are recovered when using the range $\gamma = 0 - 90°$.

Table 6.1. Average (s.d) Gaussian sphere parameters recovered for a Gaussian sphere (ν=3, σ=.05, l_{min}=2, l_{max}=50)

Angular range of covariance function $(°)$	ν	l_{min}
0-45	2.90 (0.00)	2 (0.00)
0-90	2.99 (0.03)	2 (0.00)
90-180	4.40 (0.09)	3 (0.00)
0-180	3.42 (0.04)	2 (0.00)

To determine whether to allow l_{max} to vary or to fix it at a certain value when fitting the covariance function to recover the Gaussian sphere parameters, several Gaussian spheres were generated for different values of the parameters ν, σ, and l_{min} and the covariance function was calculated for each Gaussian sphere using Eq. (6.11). The residuals between this covariance function and the analytical form of the covariance function given by Eq. (6.10) were computed as a function of l_{max} for fixed values of ν and l_{min}. We observed that the behavior of the residual as a function of l_{max} depended on the value of ν. For low values of ν, the minimum in the residual occurred at low values of l_{max} ($l_{max} < 20$), while for values of ν approaching and exceeding the original ν value, the residual converged and reached its minimum value at high values of l_{max} ($l_{max} > 50$). Thus, to avoid recovering low values for l_{max} and because higher order terms ($l_{max} > 50$) do not have a noticeable effect on the appearance of the recovered Gaussian sphere, l_{max} was fixed at 50 for the fitting procedure. Figure 6.4 shows an example of the

residual as a function of l_{max} for fixed values of ν computed for a Gaussian sphere (ν=3, σ=.05, l_{min}=2, l_{max}=50). For $\nu < 2.9$, the residual has a minimum at $l_{max} < 10$, while for $\nu \geq 2.9$, the residual converges at $l_{max} > 50$.

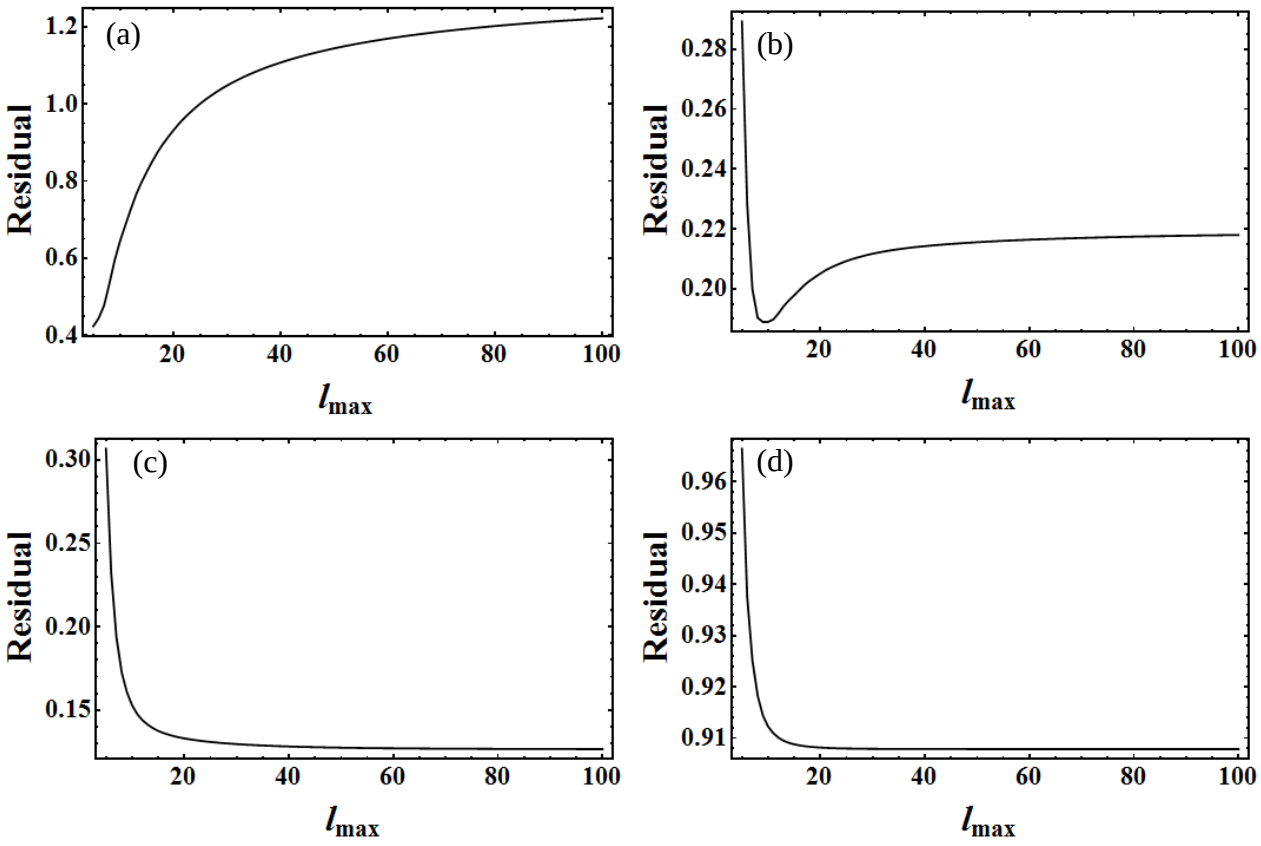

Figure 6.4: The residual as a function of l_{max} in the covariance function fitting for a Gaussian sphere (ν=3, σ=.05, l_{min}=2, l_{max}=50) with different fixed values for ν: (a) $\nu = 2.0$, (b) $\nu = 2.6$, (c), $\nu = 2.9$, and (d) $\nu = 5.0$.

Finally, there are two ways to calculate the relative standard deviation. It can be obtained by taking the square root of the covariance function at $\gamma = 0°$ and dividing by the mean. This is because the value of the covariance function for a lag length of zero is equal to the square of the RMS roughness of the surface, and the RMS value is related to the relative standard deviation

through $r_{rms}^2 = \sigma^2 \bar{r}^2$, where $\bar{r}$ is the mean radius. Or, it can be directly calculated using Eq. (2.13). It was found that direct calculation yielded better results because it reduced error due to rounding of the solid angle in the calculation of the autocovariance function.

The method just described was then used to recover the parameters from different realizations of Gaussian spheres with known parameters in order to determine the accuracy of the method for different ν, σ, and $l_{\min}$ values. Fifty realizations of Gaussian spheres were generated with various ν, σ, and $l_{\min}$ values. The original and average recovered values for each set of parameters are reported in Table 6.2. When finding the best fit for ν and $l_{\min}$, the range of the parameters was limited as follows: $\nu = 0.0 - 10.0, \Delta\nu = 0.1$, and $l_{\min} = 2 - 4$. This range for ν was chosen because larger values for ν do not have a noticeable effect on the shape. Also, $l_{\min} = 0$ and 1 were excluded from the fitting procedure because $l_{\min} = 0$ varies the size while $l_{\min} = 1$ varies the location of the origin, and higher values for $l_{\min}$ were omitted because they result in unrealistic biological shapes due to the lack of the lower spherical harmonics.

Table 6.2. Original and average recovered parameters (s.d. in parenthesis) for 50 realizations of Gaussian spheres

Original Gaussian sphere parameters			Average recovered Gaussian sphere parameters		
ν	σ	l_{min}	ν	σ	l_{min}
1.50	0.050	2	1.55 (0.22)	0.049 (0.005)	2.22 (0.42)
2.00	0.050	2	2.04 (0.32)	0.048 (0.007)	2.18 (0.39)
2.00	0.075	2	2.04 (0.32)	0.072 (0.010)	2.18 (0.39)
2.00	0.050	3	2.00 (0.29)	0.049 (0.004)	3.12 (0.33)
2.50	0.050	2	2.44 (0.47)	0.048 (0.008)	2.08 (0.27)
3.00	0.050	2	2.87 (0.62)	0.047 (0.010)	2.04 (0.20)
3.00	0.075	2	2.87 (0.63)	0.070 (0.014)	2.04 (0.20)
3.00	0.050	3	2.91 (0.45)	0.048 (0.006)	3.04 (0.20)
4.00	0.050	2	3.69 (0.93)	0.046 (0.012)	2.00 (0.00)
4.00	0.075	2	3.69 (0.95)	0.069 (0.017)	2.00 (0.00)
4.00	0.050	3	3.81 (0.70)	0.047 (0.007)	3.00 (0.00)

For all trials, ν and σ were recovered within 10% of the original value. If not exact, the recovered value for l_{min} was 1 greater than the actual value. The standard deviations (s.d.) of the recovered ν and σ tend to increase as ν increases for each l_{min} value because as ν increases, small changes in ν and σ have less impact on the resulting shape.

As can be expected due to the close agreement between the original and average recovered parameters, the original Gaussian spheres and those generated with the average recovered parameters all appear almost identical. Figure 6.5 shows an example of an original Gaussian sphere (ν=3, σ=0.05, l_{min}=2, l_{max}=50), a Gaussian sphere generated with the average recovered parameters (ν=2.87, σ=0.047, l_{min}=2, l_{max}=50), and Gaussian spheres generated with one standard deviation added to or subtracted from the average recovered ν and σ values.

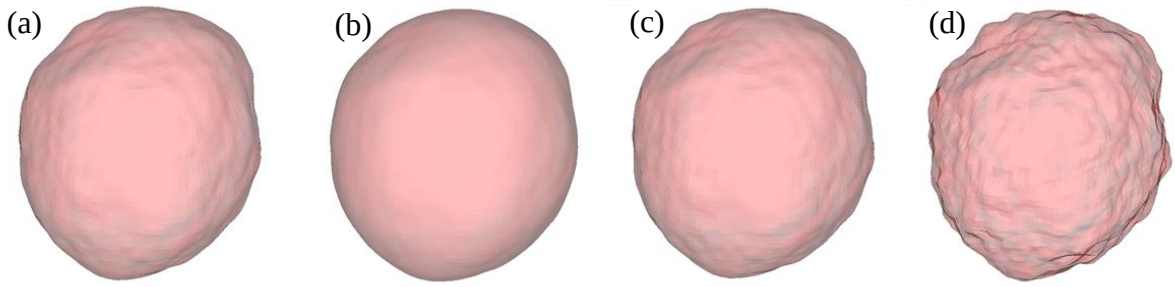

Figure 6.5: Comparison of original Gaussian sphere (ν =3, σ =0.05, l_{min} =2, l_{max} =50) with Gaussian spheres generated with average recovered parameters. (a) original Gaussian sphere and Gaussian spheres generated with (b) l_{min} =2, l_{max} =50, ν =3.49, σ =0.037, (c) l_{min} =2, l_{max} =50, ν =2.87, σ =0.047, and (d) l_{min} =2, l_{max} =50, ν =2.25, σ =0.057.

Figure 6.6 presents an example of a covariance function calculated using Eq. (6.11) for one Gaussian sphere (ν =3, σ =.05, l_{min} =2, l_{max} =50) and the analytical form of the covariance function given by Eq. (6.10) with the original parameters ($\nu = 3.0$, l_{min} =2, and l_{max} =50) and with the recovered parameters for one realization of the Gaussian sphere ($\nu = 3.8$, l_{min} =2, and l_{max} =50).

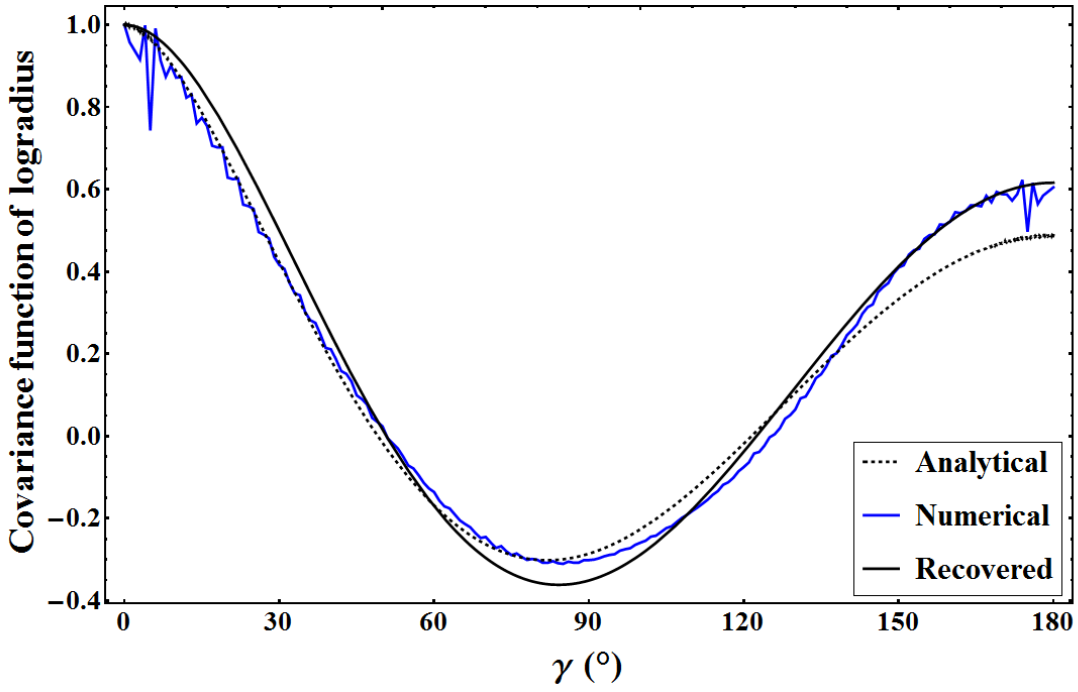

Figure 6.6: Examples of covariance functions calculated using Eq. (6.11) for a Gaussian sphere (ν =3, σ =.05, l_{min} =2, l_{max} =50) (blue line) and analytical forms of the covariance function given by Eq. (6.10) with the original parameters (dashed line) and with the recovered parameters (ν =3.8, l_{min} =2, and l_{max} =50) (black line).

6.5. Modeling cellular organelles

In addition to the cell and nucleus surfaces, the cellular substructures, including nuclear substructures and the mitochondria, are also modeled. As described in §2.3, the nucleus is heterogeneous due to the presence of various organelles. In the nucleus model presented here, the inhomogeneity is modeled as variations in index of refraction. The model is flexible in terms of the sizes of the organelles and the number of different indices that can be modeled. Small and large structures in the nucleus are modeled as ellipsoids of various sizes (voxel value equal to one) placed at random locations in the nucleus (voxel value equal to zero). After a certain number of ellipsoids are placed without overlap, some ellipsoids are allowed to overlap in order

to represent larger nuclear substructures. Regardless of the overlap between ellipsoids, all of the ellipsoidal structures have voxel values equal to 1. The ellipsoids fill up the desired percentage of the nucleus and then a window average is computed around each voxel in the nucleus to obtain more gradual transitions from the nucleus base to the refractive index fluctuations. The voxel values are then rounded to obtain the number of indices desired.

Figure 6.7 illustrates the effect of changing the percentage of ellipsoidal fluctuations and the number of nearest neighbors used in the window average when modeling the nuclear substructures. In each model, the ellipsoid fluctuations fill up 20% of the nucleus without overlap and the values are rounded to obtain five indices of refraction in the nucleus. Also, a nuclear membrane modeled as a thin shell of width 0.1 μm has been added to each nucleus model. From left to right in Figure 6.7(a-c and d-f), the ellipsoidal fluctuations fill up 40%, 50%, and 60% of the nucleus prior to the window average, respectively. From top to bottom in Figure 6.7, the window average around each voxel is computed using a 3x3x3 and a 5x5x5 box surrounding each voxel. A higher percentage of ellipsoidal fluctuations results in higher overall intensity, while increasing the number of nearest neighbors for the window average decreases the intensity.

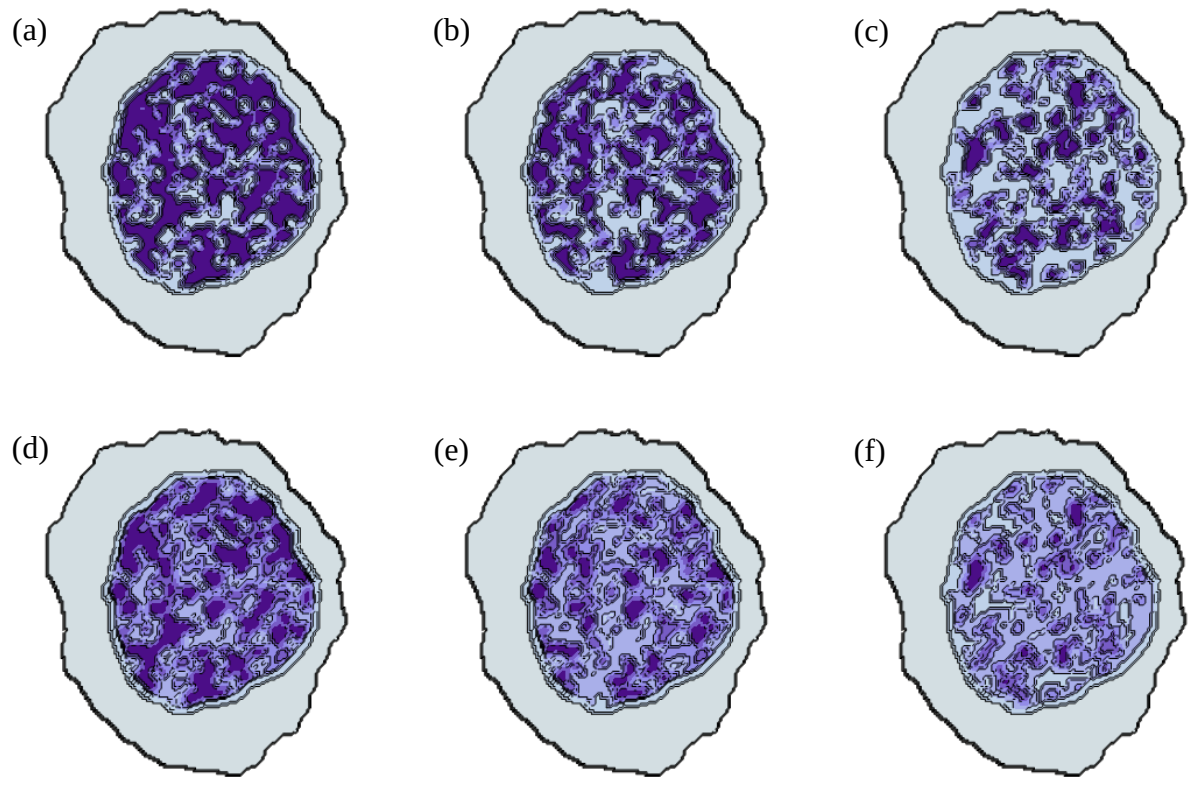

Figure 6.7: Cell models showing the effect of changing the percentage of ellipsoidal fluctuations and the number of nearest neighbors used in the window average when modeling the nuclear substructures. (a-c) The ellipsoidal fluctuations fill up to 40%, 50%, and 60% of the nucleus prior to the window average, respectively, and the window average around each voxel is computed using a 3x3x3 box surrounding each voxel. (d-f) Same as (a-c) but with a 5x5x5 box.

Mitochondria are modeled as ellipsoids of various sizes and shapes. The modeling of mitochondria as ellipsoids allows for flexibility in their placement in the cytoplasm according to specific spatial distributions, and the number of mitochondria is only limited by the size of the mitochondria and the available volume in the cytoplasm. The specific mitochondrial characteristics modeled differ in each study and are discussed on a case by case basis.

6.6. Selection of cell model parameters

This section describes the selection of the specific parameters that were selected for the construction of the analytical cell model. To model the cell and nucleus surfaces, the procedure described in §6.3 was applied to four stacks of confocal images from biological cells. Specifically, they were B-cell precursors derived from the peripheral blood of a patient with acute lymphoblastic leukemia [15]. The recovered Gaussian sphere parameters for each B-cell are given in Table 6.3 below.

Table 6.3. Recovered Gaussian sphere parameters for four B-cell surfaces and nuclei

B-cell	Ellipsoid semi-major axis (μm)			Gaussian sphere parameters		
	a	b	c	$l_{\min}$	ν	σ
#7 cell	5.00	5.32	4.64	2	1.7	0.048
#7 nucleus	4.36	4.44	3.32	3	3.4	0.095
#8 cell	5.12	4.88	5.96	2	2.3	0.068
#8 nucleus	3.32	4.04	4.76	2	2.6	0.072
#1 cell	4.56	4.64	4.96	3	2.1	0.036
#1 nucleus	3.48	4.16	4.24	3	2.4	0.054
#2 cell	4.56	5.84	4.76	2	1.9	0.063
#2 nucleus	4.04	3.88	4.48	2	1.7	0.059

The mean values of the ratio of the major and minor axes for the cell and nucleus are 1.13 and 1.18, respectively, which agree well with values of 1.1 and 1.2 found in the literature [28]. The value of ν ranges from $1.7-3.4$ while the value for σ ranges from $0.036-0.094$. Figure 6.8 presents the 3D reconstruction of two B-cell models [15] along with the analytical shape models.

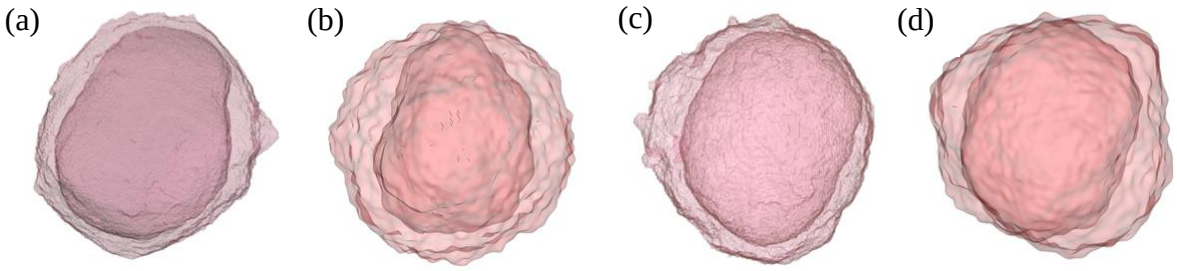

Figure 6.8: Comparison of reconstructed and analytical 3D models of biological cells. (a,c) models reconstructed from confocal images for B-cell #7 and #8, respectively. (b,d) Analytical models for each cell. *Images in (a) and (c) courtesy of Scott R. Brock* [15].

For all of the cell models that contain inhomogeneous nuclei, the parameters were chosen based on a visual inspection of confocal microscope images from Jurkat and Ramos cells. These confocal images were chosen due to the various pixel intensities present, which were assumed to correspond to various refractive indices due to the nuclear structures. Based on these images, the major structures were modeled as ellipsoidal index of refraction fluctuations with mean axes of length 0.3 ± 0.05 μm. Ellipsoids were added without overlap to fill out approximately 20% of the nucleus volume, allowing the fluctuations to be dispersed throughout the nucleus. More ellipsoids were then added, this time allowing overlap, until the fluctuations filled out approximately 50% of the nucleus volume. The window average around each voxel was computed using a 5x5x5 box surrounding each voxel. The values were rounded to obtain five indices of refraction in the nucleus. Additional examples of cell models created with the parameters just described will be presented in Chapters 8-10.

Figure 6.9 provides a visual comparison of (a) simulated and (b) experimental $\perp\perp$ polarization images. The incident wavelength was 532 nm and the scattering angle ranges were $\theta_s \approx 90 \pm 18^\circ$ and $\theta_s \approx 90 \pm 14^\circ$, respectively. Figure 6.9 (a) shows the light scattering pattern

obtained using ADDA with *dpl* equal to 10 for a cell model created as described above. The surface fluctuation for the cell model used the Gaussian sphere parameters derived for B-cell #8 shown in Table 6.3. The cell and nucleus volumes were 624 μm^3 and 268 μm^3, respectively. Mitochondria were modeled as ellipsoids with major axis size equal to 0.5 μm. A diffuse mitochondrial distribution was modeled and the ratio of mitochondria to cell was 0.05. The nucleus contained five levels of refractive index fluctuations. Figure 6.9 (b) depicts the image obtained experimentally from a Jurkat cell using a diffraction imaging flow cytometer [88]. The speckles in both images have similar sizes and spatial configurations.

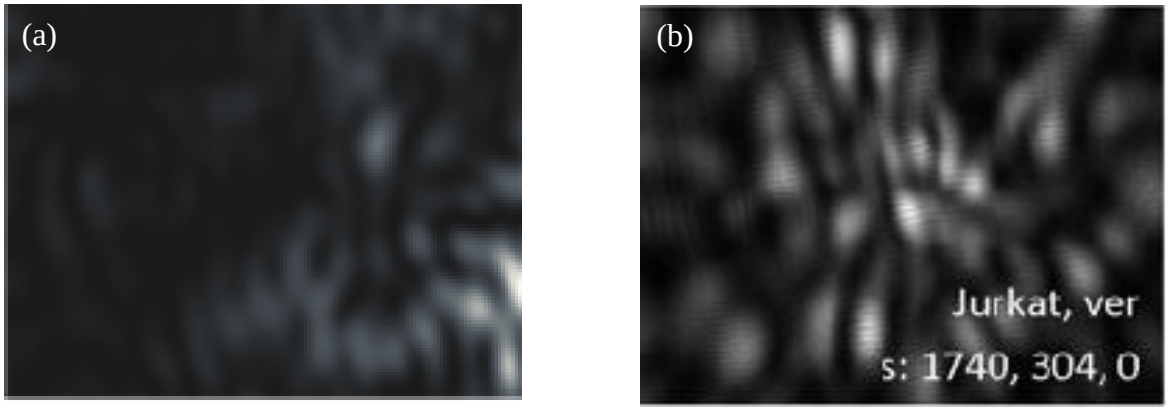

Figure 6.9: Comparison of (a) simulated and (b) experimental $\perp\perp$ polarization images for a cell. The incident wavelength was 532 nm and the scattering angle ranges were $\theta_s \approx 90 \pm 18^\circ$ and $\theta_s \approx 90 \pm 14^\circ$, respectively. *Image in (b) courtesy of Dr. Xin-Hua Hu.*

CHAPTER 7: COMPARISON OF LIGHT SCATTERING PATTERN ANALYSIS METHODS

In this study, several methods to analyze light scattering patterns from realistic biological cell models were examined. The azimuthally-averaged angular distribution of the scattered light intensity, two bi-parameter scatter plots, the Haralick features, the Laws energy measures, and Gabor filters were compared for their effectiveness in correlating changes in light scattering patterns from biological cells to variations in their morphological features. To evaluate the capabilities of these methods, the structure of a cell model was systematically altered to determine how well each method could detect the corresponding changes in the light scattering patterns. Cell structural variations were introduced in the cell shape and surface fluctuation, nuclear size, and mitochondrial characteristics (shape, spatial distribution, and volume density). The results suggest that two bi-parameter plots combined with the Gabor filter approach provide substantial information regarding the major structural features and mitochondrial properties of the cell.

7.1. Simulation methodology

A series of analytical cell models were created for a controlled study relating biological cell components to features in light scattering patterns. These cell models were divided into five groups based on their basic structure, which ranged from simple to more complex with the gradual introduction of realistic features into the cell structure. Group #1 consisted of the simplest cell models where the basic cell structure was approximated by a concentric spherical nucleus and cell. In group #2, the basic cell structure was modeled by an off-centered, ellipsoid-shaped nucleus and cell. In group #3, surface fluctuation was added to both the nucleus and cell.

In these three groups, the mitochondria population was approximated by equal-sized spheres. Group #4 introduced size variation among the spherical mitochondria, and group #5 replaced the spherical mitochondria by ellipsoidal mitochondria with various sizes and axis ratios.

The specific parameters used for the size and shape of the cell models in this study were based on the procedure described in §6.3 applied to B-cell #8. The axial lengths of the cell surface shapes in groups #2 to #5 were 5.13, 4.58 and 5.33 μm and those of the nuclei were 2.83, 2.10, and 2.63 μm. The nuclear size was scaled down to produce a volume ratio of nucleus to cell of approximately 12.5% in order to leave space for the mitochondria. The radii of the spherical cell and nucleus of the models in group #1 measured 5.03 and 2.55 μm to match the cell and nucleus volumes of the models in the other groups. The parameters for the surface fluctuations were set to be $\nu = 4.2$ and $\sigma = 0.0814$ for the cell and $\nu = 3.1$ and $\sigma = 0.0963$ for the nucleus. An extra small-scale fluctuation was also added to the cell base shape to provide finer surface roughness with $\nu = 2.0$ and $\sigma = 0.03$.

Within each of the cell groups described above, the mitochondria were placed in the cytoplasm according to a specific combination of spatial distribution and volume density. Three distributions were selected for this study: the diffuse, the peripheral, and the perinuclear. The dimensions of the peripheral and perinuclear zones, limited by the size range and density of the mitochondria, were set to be 0.8 μm along the radius direction. The mitochondrial volume density, defined as the ratio of the total volume of the mitochondria to that of the cell, was chosen to be 1.0, 4.0, and 7.0%. The number of mitochondria was allowed to vary among the three densities.

The size of the mitochondria varied in each cell group in order to keep the number of mitochondria at a specified density similar among different distributions. The radii of the

spherical mitochondria in cell groups #1 to #3 varied slightly among cell models with different densities and distributions in the range of 0.29 μm – 0.31 μm. The radius range of the spherical mitochondria of various sizes in model #4 was 0.19 μm - 0.42 μm. The axial lengths for the ellipsoidal mitochondria in model #5 were adopted from the literature [16, 17] with the major axis in the range 0.3 μm - 0.8 μm and the minor axes in the range 0.15 μm - 0.3 μm. A total of forty-five analytic cell models were created with three spatial distributions and three densities for mitochondria in each of the five cell groups.

All of the light scattering calculations used the DDA method. The incident field was modeled as a plane wave with wavelength λ = 1.0 μm. The cell was assumed to be immersed inside a host medium of index of refraction n=1.35. The indices of refraction of each cell component were chosen based on the literature: $n_{cytoplasm}$=1.3675, n_{nuc}=1.40, and n_{mito}=1.42. Each cell component had an imaginary index of refraction n=0.000015. For each scatterer, the Mueller matrix elements as a function of the scattering angle θ_s and the azimuthal angle φ_s were calculated for eight different incident electric field directions spanning all space. This was equivalent to simulating the scattering from eight orientations of the scatterer with the incident direction fixed. The set of eight incident angles (θ_s, φ_s) used are {(9.7°, 315.0°), (65.9°, 71.6°), (66.0°, 198.4°), (80.3°, 315.0°), (99.7°, 135.0°), (114.1°, 18.4°), (114.1°, 251.6°), (170.3°, 135.0°)}. The scattering patterns were obtained by projecting the S_{11} Mueller matrix element onto a plane 500 μm away in the side angle direction. The center location of the plane, denoted by the polar angle θ and azimuth angle φ, was $\theta = 90^\circ$ and $\varphi = 90^\circ$, and the half angle subtended by the detector at the lens was 30.0° with angular resolution of 1.0° along each direction. A schematic is shown in Figure 7.1.

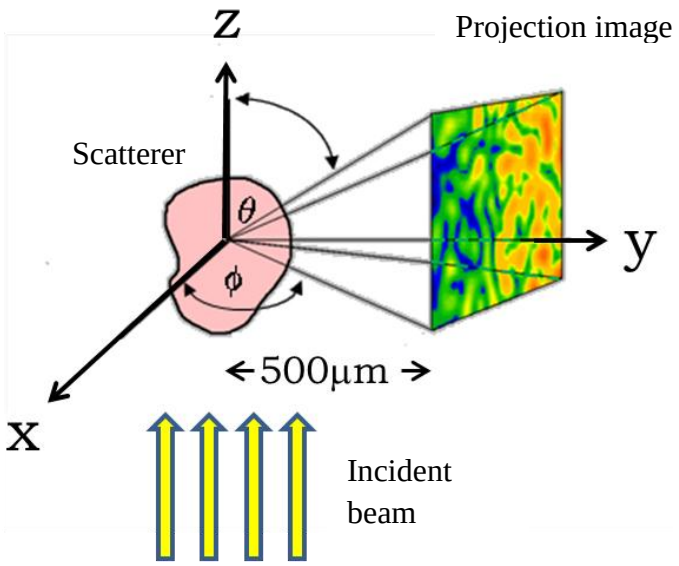

Figure 7.1: Projection image schematic for light scattering simulations. The S_{11} Mueller matrix element is projected onto a plane 500 μm away in the side angle direction ($\theta = 90^{\circ}$ and $\varphi = 90^{\circ}$).

Examples of the cell models in groups #1 and #5 with perinuclear, diffuse, and peripheral mitochondrial distributions and their corresponding projected scattering images are shown in Figure 7.2. The mitochondrial density is 4.0% for these cell models. It is clear that the projected images are very different among cell models with different structure characteristics; there are less variations in intensity in the models from group #5 (bottom) compared to those from group #1 (top) and the speckle size decreases as the mitochondrial distribution is closer to the membrane (left to right).

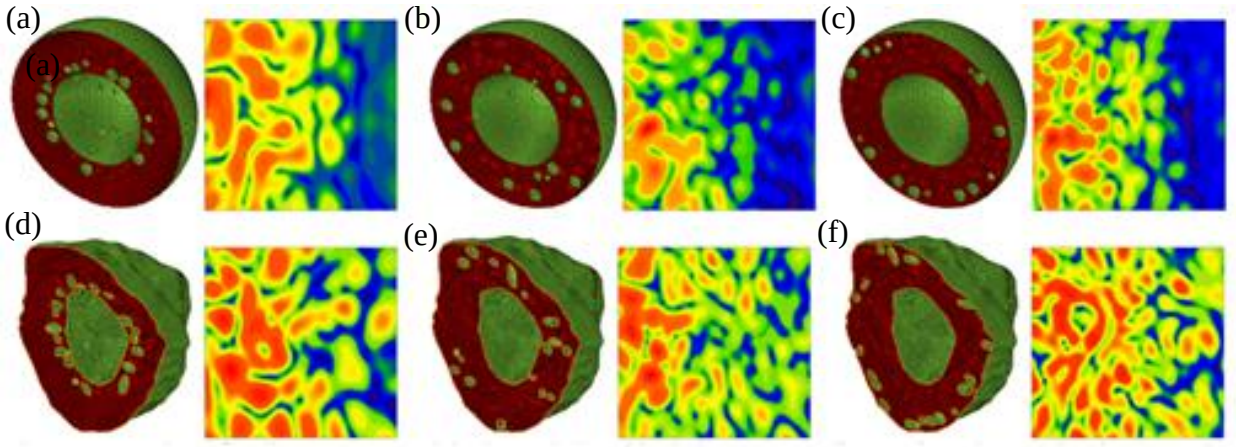

Figure 7.2: Examples of cell models and their corresponding projected scattering images. (a-c) Concentric spherical cell model with equal-sized spherical mitochondria from cell group #1. (d-f) Cell model with ellipsoidal base shape, surface fluctuation, and ellipsoidal mitochondria of various sizes in cell group #5. Models are shown with (a,d) perinuclear, (b,e) diffuse, and (c,f) peripheral mitochondrial distributions.

As discussed above, the Haralick features, Laws energy measures, and Gabor filters were applied to analyze the projected images. When calculating the Haralick features, a moving window of size 15x15 pixels was chosen and the gray levels of the images were quantized to eight values, as common in the literature [89]. The co-occurrence matrix was calculated for nearest neighbors (d=1) and averaged over the four directions. Furthermore, only 11 out of the 14 Haralick features were calculated due to computational difficulties in features #12-13 and instability in #14. For the analysis with the Laws masks, the absolute value in local neighborhoods (15x15 pixels) around each pixel of the filtered image was summed to yield a set of 24 texture energy images. The arithmetic mean of these images was calculated to yield a set of 24 energy measures for each original image. For the Gabor filters, the frequencies and orientations chosen were based on the characteristics of the scattering images from the cell models. Three frequencies (0.1, 0.2 and 0.4 pixel^{-1}) and four orientations evenly spaced from 0° to 135° were chosen, producing a set of 3x4 Gabor filters. The size of the filter was set to be

21x21 pixels. The arithmetic mean of each Gabor-filtered image was computed. The notation G_{mn} represents the arithmetic mean of the Gabor-filtered image produced by applying the filter with the m^{th} frequency and n^{th} orientation to an image. For example, G_{33} represents the arithmetic mean of the Gabor-filtered image produced by applying the filter with frequency 0.4 $pixel^{-1}$ and orientation 90° to an image.

Each of the three texture analysis methods yields a feature vector consisting of a set of values that represents a scattering image. To find an accurate and efficient way to differentiate images using these vectors, we explored the combinations of the vector components that would best characterize each scattering image when plotted in a scatter plot. For the various cases studied in the section below, the best combinations were found to be; Difference Variance vs. Sum Average for the Haralick features; *S5R5* vs. *E5W5*, a convolution of the Spot and Ripple vectors versus that of the Edge and Wave vectors for Laws measures; and G_{33} vs. G_{13} for the Gabor measures. These combinations are displayed in scatter plots which are referred to as Haralick, Laws, or Gabor scatter plots in the discussions below.

7.2. Analysis of angular distribution of the scattered light intensity

For an initial analysis of the light scattering data, the azimuthally-averaged angular distribution of the scattered light intensity averaged over the eight incident orientations for the entire scattering angle range of 0° - 180° was examined. Results for cell groups #1-5 are displayed in Figure 7.3 (a-e), respectively, and results for all cell groups together are shown in Figure 7.3 (f). In the following figures, the results for cell models with different mitochondrial spatial distributions are represented by blue (diffuse), red (peripheral), and green (perinuclear) symbols,

and the mitochondrial densities are indicated by the shade of the color, from light (1%) to dark (7%).

In Figure 7.3, the curves group according to different cell characteristics in separate regions of the scattering angle. Since all of the models have the same cell and nucleus volume, all of the curves overlap very well in the first 10° when plotted together, demonstrating the well-known fact that the forward scattering is closely related to the cell volume and cell scattering power, and it also shows that the forward scattering is not very sensitive to cell structure variation. From 10° to 25°, the curves appear to group according to mitochondrial spatial distribution with the perinuclear distribution (green curves) well separated from the other two distributions, especially in Figure 7.3 (c-e). In this angular range, the curves in Figure 7.3 (a-b) display more pronounced oscillations, due to the spherical and ellipsoidal symmetry, respectively, in the main cell structure. These oscillations obstruct the distinction between mitochondrial distributions in this angular range.

The curves group according to mitochondrial density in the region from 40° to 180°. In all of the cell groups, the curves for cell models with a density of 1% are better separated from the others. In the region from 90° to 130°, the curves in Figure 7.3 (a-c) are significantly lower with a dip at 120° while those in Figure 7.3 (d-e) are relatively level in this region. This dip seems to be due to the change from spherical to ellipsoidal mitochondria in the cell models.

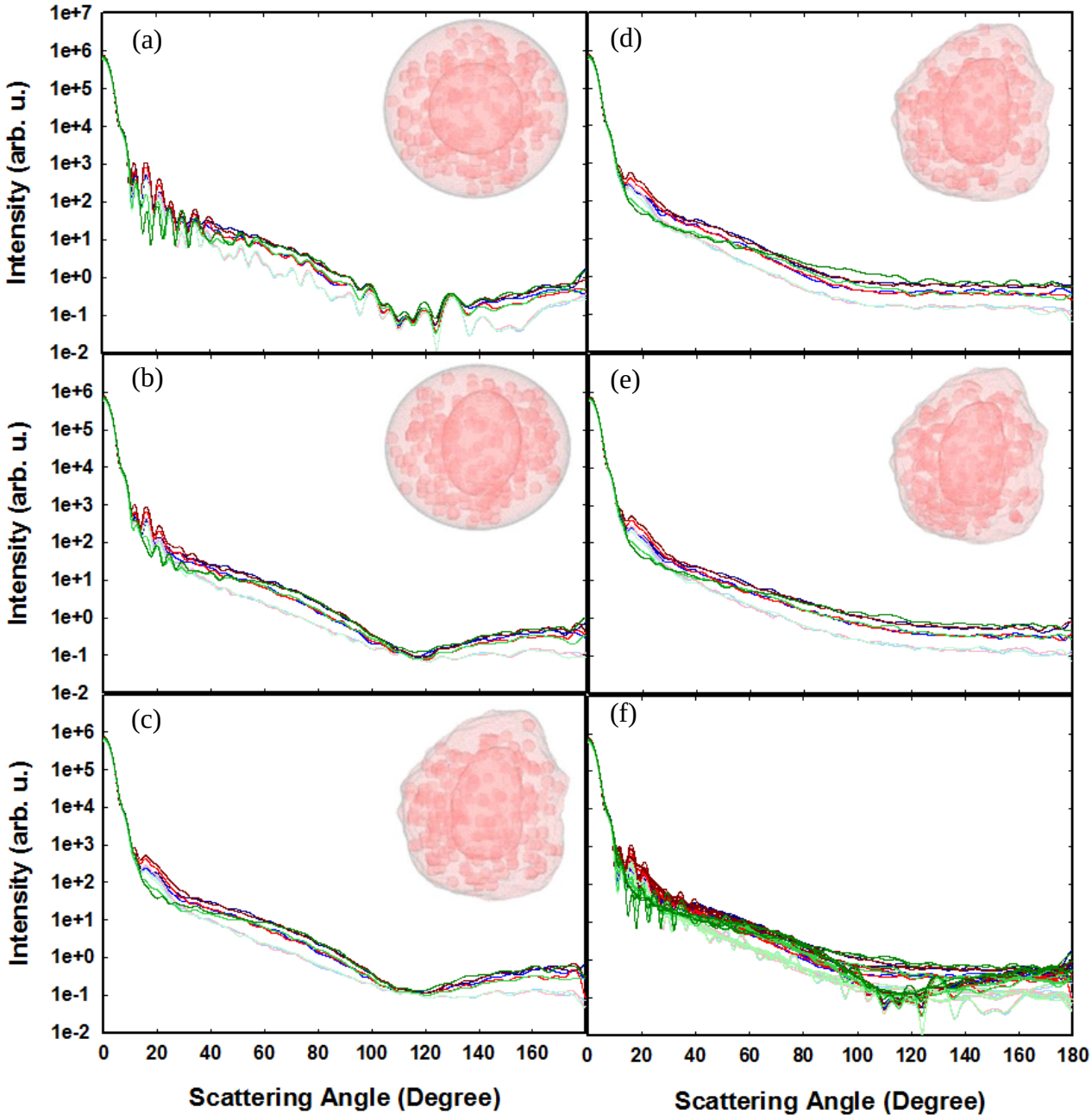

Figure 7.3: The azimuthally-averaged angular distribution of the scattered light intensity averaged over the eight incident orientations. (a-e) Results of cell models in groups #1 - #5, respectively. (f) Results for all cell models. Cell models with diffuse, peripheral, and perinuclear distributions are represented by blue, red, and green lines, respectively. Mitochondrial density is indicated by the shade of the color, from light (1%) to dark (7%).

Next, several ways of differentiating the cell models were explored utilizing data from the various scattering angle regions discussed above. Figure 7.4 presents the bi-parameter scatter plots of the forward scatter, $S_{11}(0°)$, versus the integral of S_{11} over the range (a-e) θ_s = 25° - 45° and (f-j) θ_s = 90° - 110°. Instead of the orientation-averaged data presented in Figure 7.3, data for the eight individual orientations of each cell model are displayed here, with each orientation represented by a data point. Data for the cell models of the five different basic structure groups are plotted separately from top to bottom.

The bi-parameter scatter plots of $S_{11}(0°)$ vs. $\int_{90°}^{110°} S_{11}(\theta_s)\,d\theta_s$ in Figure 7.4 (a-e) clearly show that data points for each cell model respond strongly to changes in the mitochondrial characteristics. Figure 7.4 (a) contains three distinct subgroups corresponding to the three mitochondria densities (increasing from left to right) and within each sub-group, the spatial distributions of the mitochondria can be separated vertically by the forward scatter intensity. In Figure 7.4 (b) and (c), as the complexity of the cell and nucleus base shapes increases, the gaps between the distribution subgroups practically disappear as the data points spread out vertically, while the distinction between the mitochondrial densities is still present. In Figure 7.4 (c-e), as mitochondrial size and shape variations are introduced, the scatter plot undergoes more dramatic changes. The sub-groups of different densities display a horizontal shift to the right and also have a better defined separation between them.

In Figure 7.4 (d), a shift to the right of the data points from the cell models with a perinuclear distribution and larger mitochondria densities is noticed. This shift is caused by the relatively larger number of smaller mitochondria used for these cell models, a consequence of space limitation in the perinuclear zone for spherically-shaped mitochondria. The same shift to the

right was noticed in other models (data not shown) where the number of mitochondria was purposely increased while the density was kept constant. The space limitation issue is not as severe in the case of cell group #5 where the shape is replaced by ellipsoids, thus no such effects are observed in Figure 7.4 (e). This observation further demonstrates the capability of this type of bi-parameter scatter plot of detecting variations within the mitochondria population.

A different grouping pattern of data points and different response to cell structural changes are observed in Figure 7.4 (f-j), the bi-parameter scatter plot of $S_{11}(0°)$ vs. $\int_{25°}^{45°} S_{11}(\theta_s)\,d\theta_s$. Figure 7.4 (f) shows clear subgroups of different mitochondrial densities and spatial distributions. In Figure 7.4 (g-h), the gaps between the subgroups disappear due to the changes in the base shape of the cell models. This is especially apparent in Figure 7.4 (h), where surface fluctuation is introduced. No significant changes in the plots are observed in Figure 7.4 (i-j), where modifications are made to the size and shape of the mitochondria. Overall, the results suggest that the signal in the angular range from θ_s = 25° - 45° is more sensitive to changes in the overall structure rather than mitochondrial changes.

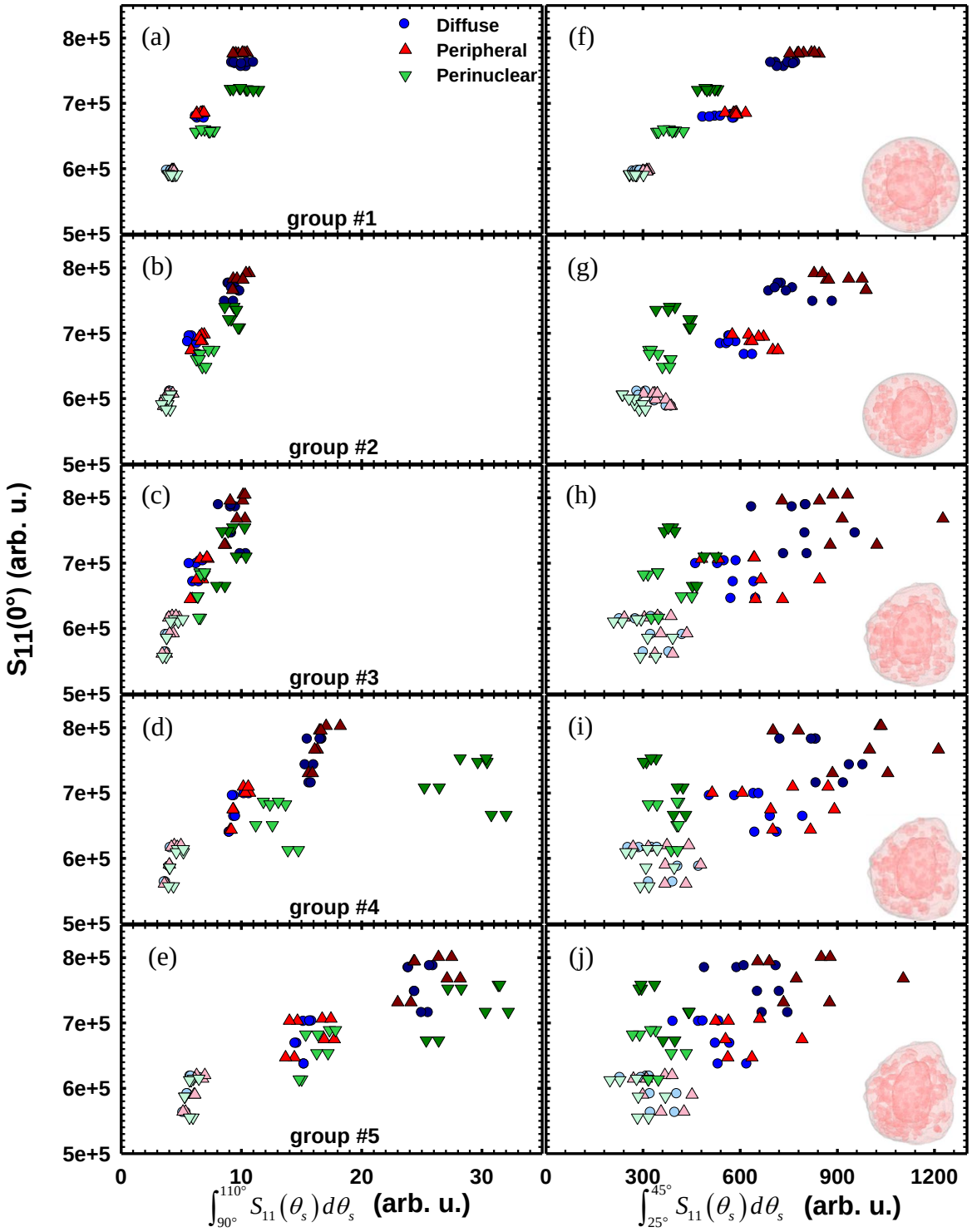

Figure 7.4: Bi-parameter scatter plots of the forward intensity versus the azimuthally-averaged intensity integrated over the scattering angle range of (a-e) 90°–110° and (f-j) 25°–45°. Data for the cell models in groups #1–#5 are plotted separately from top to bottom. Mitochondrial spatial distributions are represented by blue (diffuse), red (peripheral), and green (perinuclear) color, and the shade of each color indicates mitochondrial density, from light (1%) to dark (7%).

In summary, the azimuthally-averaged angular distribution of the scattered light intensity provides valuable insight into the surface and internal structure of the cell model. Signals in different angular regions provide information about different aspects of the cell structure: the forward scattering region relates to the cell size, the θ_s = 10° - 25° range to the mitochondrial distribution, the θ_s = 25° - 45° range to the main cell structure, θ_s = 90° - 110° range to mitochondrial size and shape, and the region from θ_s = 40° - 180° to mitochondrial volume density. Although it has been suggested that the forward scatter can differentiate between mitochondrial spatial distributions [28], this is only reaffirmed in the scatter plots of the simplest cell models in Figure 7.4 (a and f). Increasing the complexity of the model diminishes the distinction between the distributions, as is evident in the rest of the plots in Figure 7.4.

7.3. Analysis of light scattering diffraction image

The 2D projected scattering images were analyzed using the image texture analysis methods described in Chapter 5. The images were first analyzed with Gabor filters. The arithmetic means G_{33} and G_{13} of the Gabor-filtered images were computed for each orientation of the cell models. Figure 7.5 (a) presents the Gabor scatter plots of G_{13} vs. G_{33} for all forty-five models combined. Due to the lack of significant differences between the results of the individual cell groups, the plots for each cell group are not shown separately as in Figure 7.4. The data points of the cell models with the same mitochondrial distribution appear to cluster linearly. The clustering indicates that the Gabor scatter plot may provide a quantitative way of differentiating cells with different mitochondrial distributions. In addition, Figure 7.5 also shows that Gabor filters may be a useful tool for separating cell models with different mitochondrial densities.

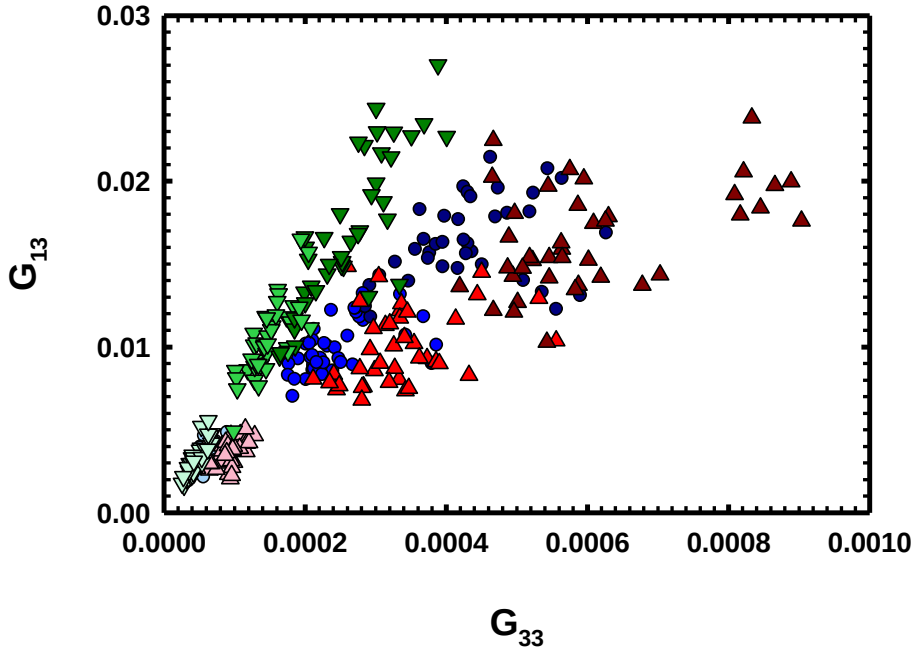

Figure 7.5: Gabor scatter plot with data from all cell models in groups #1 - #5. Results with all eight incident orientations for each cell model are shown. Mitochondrial spatial distributions are represented by blue (diffuse), red (peripheral), and green (perinuclear) color, and the shade of each color indicates mitochondrial density, from light (1%) to dark (7%).

Next, the same set of images was analyzed using the Haralick and Laws methods. The Haralick and Laws scatter plots for cell group #5 are displayed in Figure 7.6 (a) and (b), respectively. There were no significant differences in the scatter plots of the cell models associated with the other cell groups (not shown). The data points in Figure 7.6 are closely packed and there is a significant amount of overlapping among the cell models with different mitochondrial distributions and densities. There is an exception in Figure 7.6 (b), where the cell models with a perinuclear distribution are well separated from the rest, agreeing with the results from previous studies [3]. Several other pairs of Law energy measures, such as R5E5 and W5E5 (not shown), are capable of separating the cell models with a perinuclear mitochondrial distribution, but only when the simplest cell structure model #1 is used. Overall, it is evident that

these two methods are not as effective in relating changes in the light scattering patterns to variations in the cell morphological characteristics as the bi-parameter S_{11} scatter plot in Figure 7.4 and the Gabor scatter plot in Figure 7.5. Thus, the Haralick and Laws methods were not considered further in the rest of the studies presented in this dissertation.

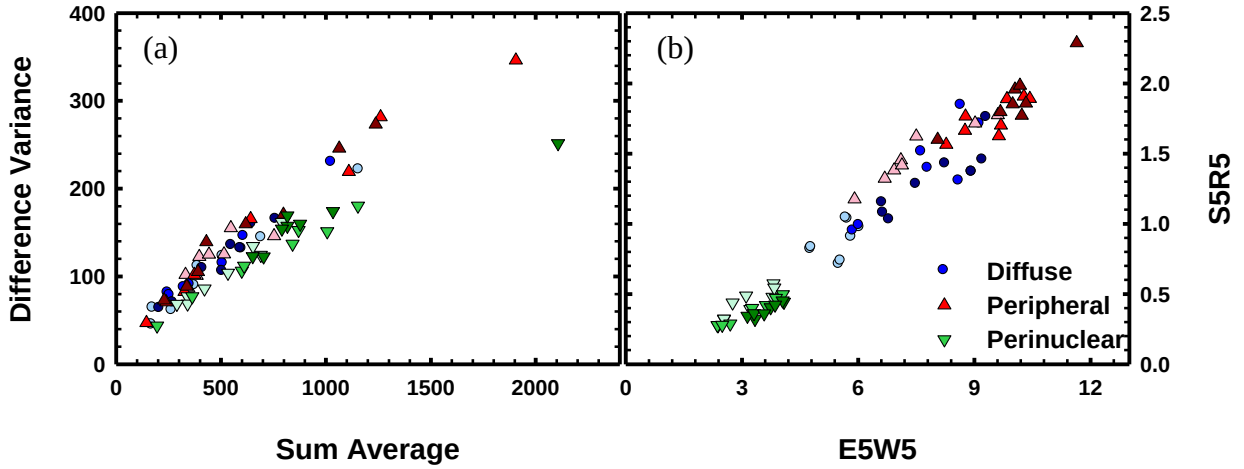

Figure 7.6: (a) Haralick and (b) Laws scatter plots for cell models in group #5. Mitochondrial spatial distributions are represented by blue (diffuse), red (peripheral), and green (perinuclear) color, and the shade of each color indicates mitochondrial density, from light (1%) to dark (7%).

The last part of this study compares the ability of the angular distribution of the scattered light intensity and Gabor filters in detecting differences in nuclear size in the cell models. Here, the volume of the nucleus in the cell models in group #5 was increased from 12.5% of the total cell volume to 25.0% and 50.0%. A larger nucleus reduces the available space for the mitochondria in the cytoplasm; consequently, the cell models were limited to a diffuse mitochondrial distribution for the 50.0% case. Results for cell models in group #5 are presented in the form of the bi-parameter scatter plot of the forward scatter versus the integral of S_{11} over

the range θ_s =90° - 110° in Figure 7.7 (a) and the Gabor scatter plot in Figure 7.7 (b). The results in both plots are orientation-averaged. The effect of nuclear size is most evident in Figure 7.7 (a) as greater nuclear volume increases forward scatter. The points are well grouped vertically according to nuclear size and horizontally according to density, and the points are closely packed within each group. The Gabor scatter plot in Figure 7.7 (b), similarly to Figure 7.5, is responsive to mitochondrial distribution, but is less dependent on the volume of the nucleus, with only a slight shift to the right with an increase in nuclear size. The latter behavior further confirms the observation discussed earlier that the Gabor scatter plot for images at this scattering angle is not very sensitive to changes in the main structure of the cell.

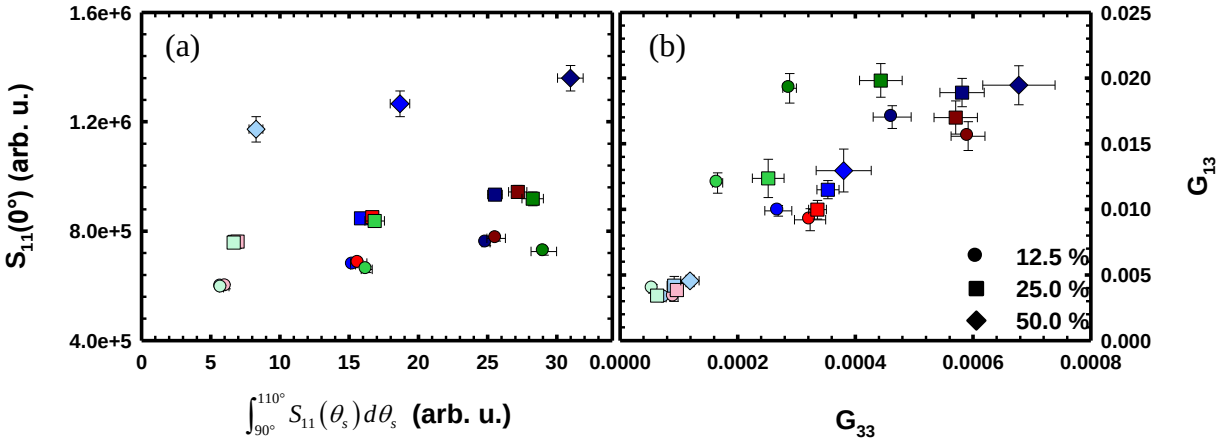

Figure 7.7: (a) The forward intensity versus the azimuthally-averaged intensity integrated over the scattering angle range of 90°–110° and (b) the Gabor scatter plot for cell models with different nucleus-to-cell volume ratios. The data in each plot is averaged over the eight incident orientations (±1 standard deviation). Mitochondrial spatial distributions are represented by blue (diffuse), red (peripheral), and green (perinuclear) color, and the shade of each color indicates mitochondrial densities, from light (1%) to dark (7%).

This study investigated the capabilities of various light scattering pattern analysis methods in correlating variations in cell models to changes in the light scattering patterns. The complexity

of the cell model was gradually increased, from the standard spherical cell model with spherical mitochondria to an off-centered ellipsoidal base shape with surface fluctuation and ellipsoidal mitochondria of various sizes. The influence of these structural variations on light scattering patterns was examined through analysis with the bi-parameter plots and the Gabor, Haralick, and Laws image texture analysis methods. It was found that the bi-parameter plots responded strongly to an increase in the complexity of the cell model, allowing changes in the main structure of the cell and in the mitochondria to be identified. In particular, the bi-parameter plot of S_{11} with an angular range of 90° - 110° is well suited for characterization of mitochondrial density and nuclear size. The results of texture analysis on diffraction images show that Gabor filters have the potential to provide a new and quantitative approach to distinguish different mitochondrial distributions, while the Laws and Haralick texture measures are not very efficient in discriminating structure variations in realistic cell models. As a result of this study, the Laws and Haralick methods were not pursued further.

CHAPTER 8: CORRELATING THE MORPHOLOGY AND LIGHT SCATTERING PATTERNS OF BIOLOGICAL CELLS

This chapter presents a study of the correlation between the morphology and light scattering properties of biological cells. Here we analyze the changes in the light scattering patterns in response to the systematic alterations in the cell models. The effects of nuclear structure and mitochondria on the light scattering patterns are examined.

For this study, seven cell models were created. The first model consisted of concentric spheres with radii 3.9 and 5.3 μm for the nucleus and cell, respectively. In the second model and in the rest of the models, the nucleus was placed off-centered by 0.35 μm. In the third model, a thin nuclear membrane of approximate thickness of 0.1 μm was added, while in the fourth model, nucleoli of radius 1.1 μm were added to the nucleus. In the fifth model, both a thin membrane and nucleoli were added to the nucleus. In the sixth model, index of refraction fluctuations were added to represent nuclear substructures as described in §6.3. Each nucleus had a random spatial configuration of refractive indices that corresponded to five levels of index of refraction fluctuations. The seventh model combined a thin membrane, nucleoli, and index of refraction fluctuations in the nucleus. Cross-sections of the seven models are shown in Figure 8.1 (a-g).

All of the light scattering calculations used the DDA method. The incident field was modeled as a plane wave with wavelength $\lambda = 1.0$ μm. The cell was assumed to be immersed inside a host medium of water with index of refraction n=1.334. The indices of refraction of each cell component were: $n_{cytoplasm}$=1.3675, n_{nuc_mem}=1.41, $n_{nucleolus}$=1.44, and n_{mito}=1.42. The nucleus was modeled with five levels of index of refraction fluctuations ranging from 1.38 to

1.42 with an average $n_{nucleus}$=1.4. Each cell component had an imaginary index of refraction n=0.000015. For each scatterer, the Mueller matrix elements were calculated for the same eight different incident electric field directions spanning all space listed in §7.1. Projection images for the six polarization combinations described in §3.2 were obtained.

Sets of || || and ||⊥ polarization images corresponding to the seven cell models are also shown in Figure 8.1. The images are normalized to the maximum to emphasize the structure of the image and the values at the bottom of each image represent the minimum, maximum, and mean values of each image. There are noticeable changes in the scattering patterns due to the nuclear structural changes. The || || images show a disruption of the vertical bands for models #6 (f) and #7 (g) with index of refraction fluctuations. In the ||⊥ polarization images, the speckle size increases with the addition of nucleoli (d) and then again with the addition of index of refraction fluctuations (f), although the small speckles in the (a-c) can be considered to be calculation errors as the intensity should be zero due to the symmetry of the scatterer.

Next, the effects of modeling the nucleus with increasing complexity in a cell model with surface fluctuation for both cell and nucleus surfaces were examined. Cross-sections of the seven models and sets of || || and ||⊥ polarization images corresponding to the cell models are shown in Figure 8.2. There are less dramatic visible changes in the scattering patterns. The more obvious changes are those in the ||⊥ polarization images due to the addition of index of refraction fluctuations (f).

The nuclear structure effects in a cell model with mitochondria were also examined. A diffuse distribution of spherical mitochondria of radius 2.5 μm was added to the seven cell models with mitochondrial volume densities of 2.0, 5.0 and 8.0%. Cross-sections of the seven

models with surface fluctuation and 8.0% mitochondrial volume density and sets of ∥∥ and ∥⊥ polarization images corresponding to the cell models are shown in Figure 8.3. There is a visible change from (a) to (b), but this most likely due to the rearrangement of the mitochondria rather than the nucleus being placed off-center. There are no other visible changes in the light scattering patterns.

A Gabor analysis of the polarization images discussed above revealed measurable changes in the patterns. Figure 8.4 (a) shows the analysis of the ∥⊥ polarization images with a Gabor filter with frequency of 0.08 pixels^{-1} and orientation of 45°. Results are shown for eight cell models. Models 1-4 correspond to the first, second, sixth, and seventh spherical cell models described above, and models 5-8 represent the same models with surface fluctuation. Analysis of the scattering images shows an increase in the Gabor energy due to addition of nuclear substructures in both the simple spherical cell model and the one with surface fluctuation.

Figure 8.4 (b) shows the Gabor energy for the ⊥⊥ polarization images for the same eight cell models with four options for mitochondrial volume density: 0% (models #1-8), 2.0% (models #9-16), 5.0% (models #17-24), and 8.0% (models #25-32). The Gabor filter had a frequency of 0.04 pixels^{-1} and orientation of 90°. In both the simple cell model and the one with surface fluctuation, there is a measureable increase in Gabor energy as a result of the increase in complexity of the nuclear model. Figure 8.4 (b) also shows a measureable increase in Gabor energy as a result of the increase in mitochondrial volume density in the cell models.

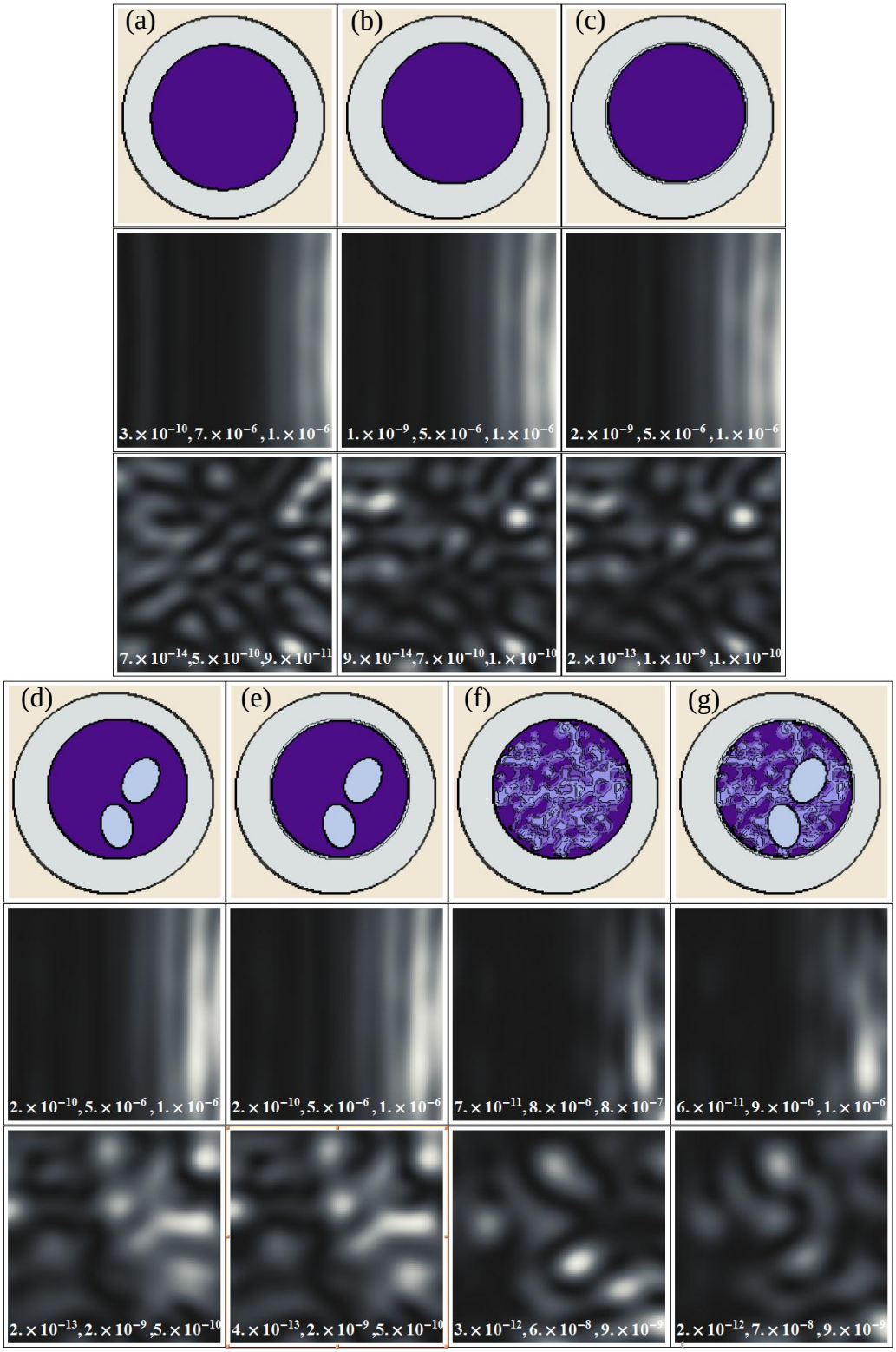

Figure 8.1: (a-g) Cross sections of the seven smooth cell models with increasing nuclear complexity and their corresponding $\parallel \parallel$ and $\parallel\perp$ polarization images. The minimum, maximum, and mean intensity are shown on each image.

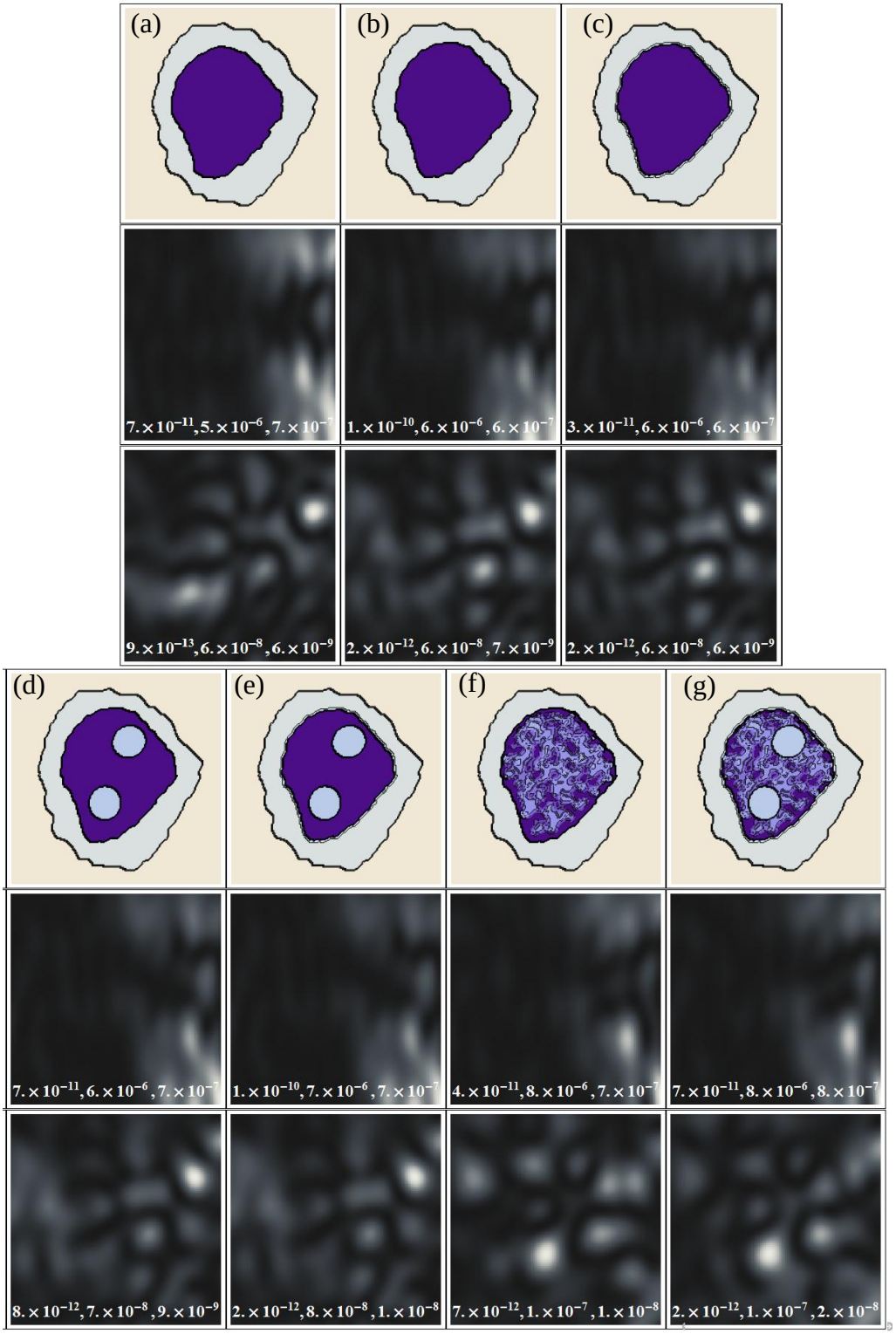

Figure 8.2: (a-g) Cross sections of the seven cell models with surface fluctuation with increasing nuclear complexity and their $\parallel\parallel$ and $\parallel\perp$ polarization images. The minimum, maximum, and mean intensity are shown on each image.

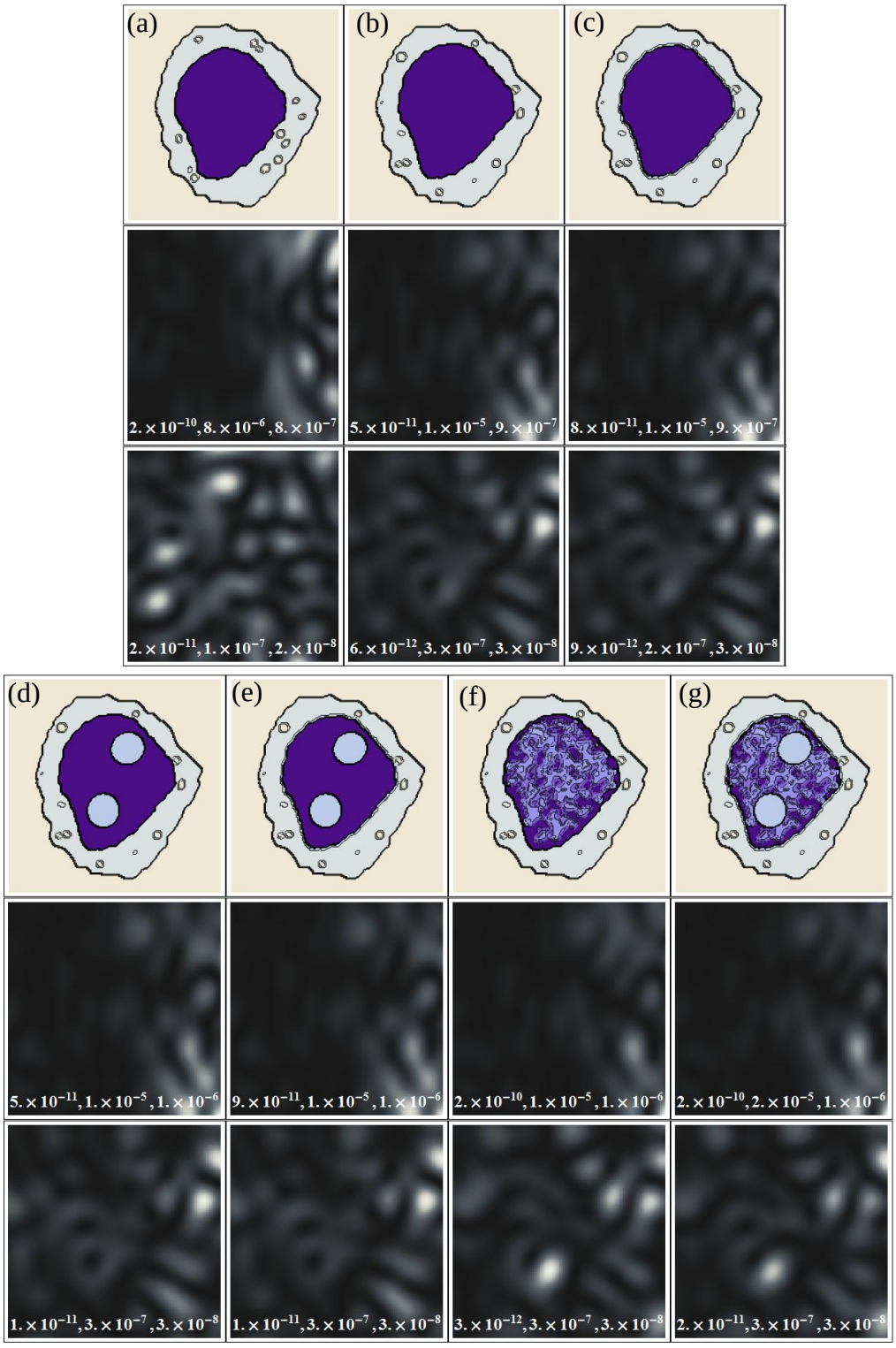

Figure 8.3: (a-g) Cross sections of the seven cell models with surface fluctuation and mitochondria with increasing nuclear complexity and their $\parallel\parallel$ and $\parallel\perp$ polarization images. The minimum, maximum, and mean intensity are shown on each image.

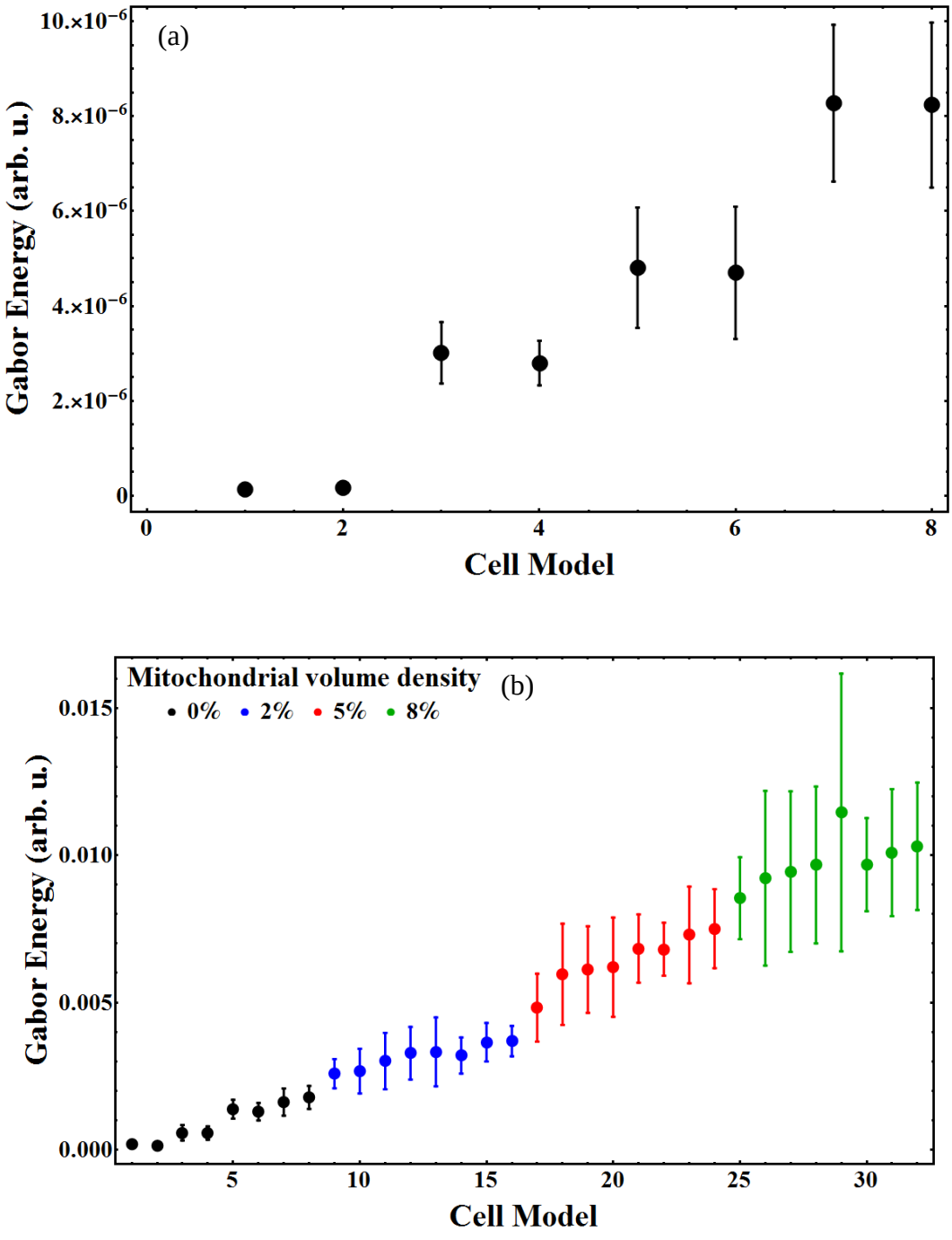

Figure 8.4: Analysis with Gabor filters of polarization images for eight cell models depicted in the previous figure. Gabor energy results for (a) ||⊥ and (b) ⊥⊥ polarization images. In (b), models are shown with increasing mitochondrial volume density.

For a more in-depth look at the influence of mitochondria, the light scattering patterns from the cell models with a mitochondrial volume density of 0, 2.0%, 5.0%, and 8.0% presented above were compared to light scattering patterns from cell models with an equivalent homogeneous index of refraction for the cytoplasm. The cell models and corresponding $\parallel\parallel$ and $\parallel\perp$ polarization images are shown in Figure 8.5. The images for the three cell models with an equivalent index in the cytoplasm are not shown because they appear identical to those from the model without mitochondria. For the models with an increase in mitochondrial density, the texture has a similar pattern in all of the $\parallel\parallel$ images while the $\parallel\perp$ images show visible differences in the number of speckles and organization of the speckles.

For a quantitative analysis of the images, the scattering cross section for each cell model and the average intensity of each image was calculated. The plots in Figure 8.6 show the (a) cross section and (b) the average intensity for the $\parallel\perp$ image. The scattering cross section, which provides an indication of the total scattering power of the particle as discussed in §3.3, does not differentiate between the models with and without mitochondria, but it does increase due to the increase in index of refraction of the cytoplasm. The average intensity of the image, however, increases with the addition of mitochondria but remains constant with the increase in index of refraction of the cytoplasm.

This study correlated changes in cell morphology to changes in the light scattering patterns through a visual inspection and quantitative analysis. It showed the effects on the size and configuration of the speckles in the light scattering patterns of increasing the complexity of the nucleus in a smooth cell model, a model with surface fluctuation, and a model with mitochondria. Although the light scattering patterns responded strongly to the nuclear

substructure changes in the smooth models, less dramatic changes were observed in the light scattering patterns from the models with surface fluctuation and mitochondria. However, quantitative analysis revealed an increase in Gabor energy of the light scattering patterns due to the increased complexity of the nucleus model. In addition, the study revealed that the light scattering patterns are very sensitive to the number of mitochondria in the cell and that the average intensity of the polarization images can provide an indication of mitochondrial volume density. These results suggest that a complex nuclear structure and mitochondria should be included when modeling biological cells for light scattering simulations.

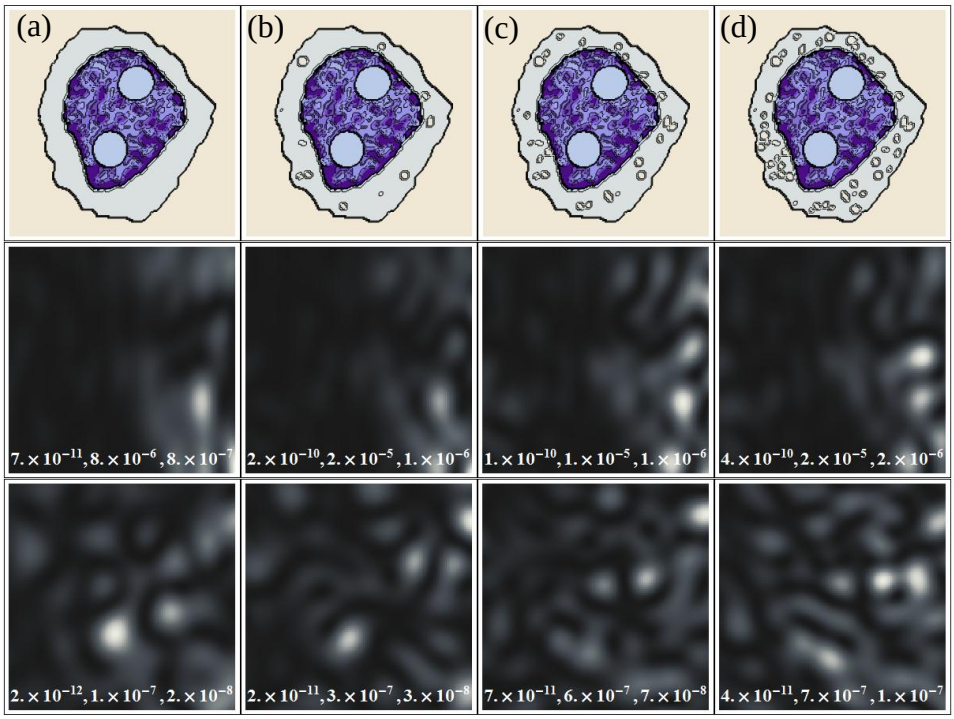

Figure 8.5: (a-d) Cross sections of cell models with increasing mitochondrial density and their $\parallel$ $\parallel$ and $\parallel\perp$ polarization images. The models have 0%, 2.0%, 5.0%, and 8.0% mitochondrial volume density, respectively.

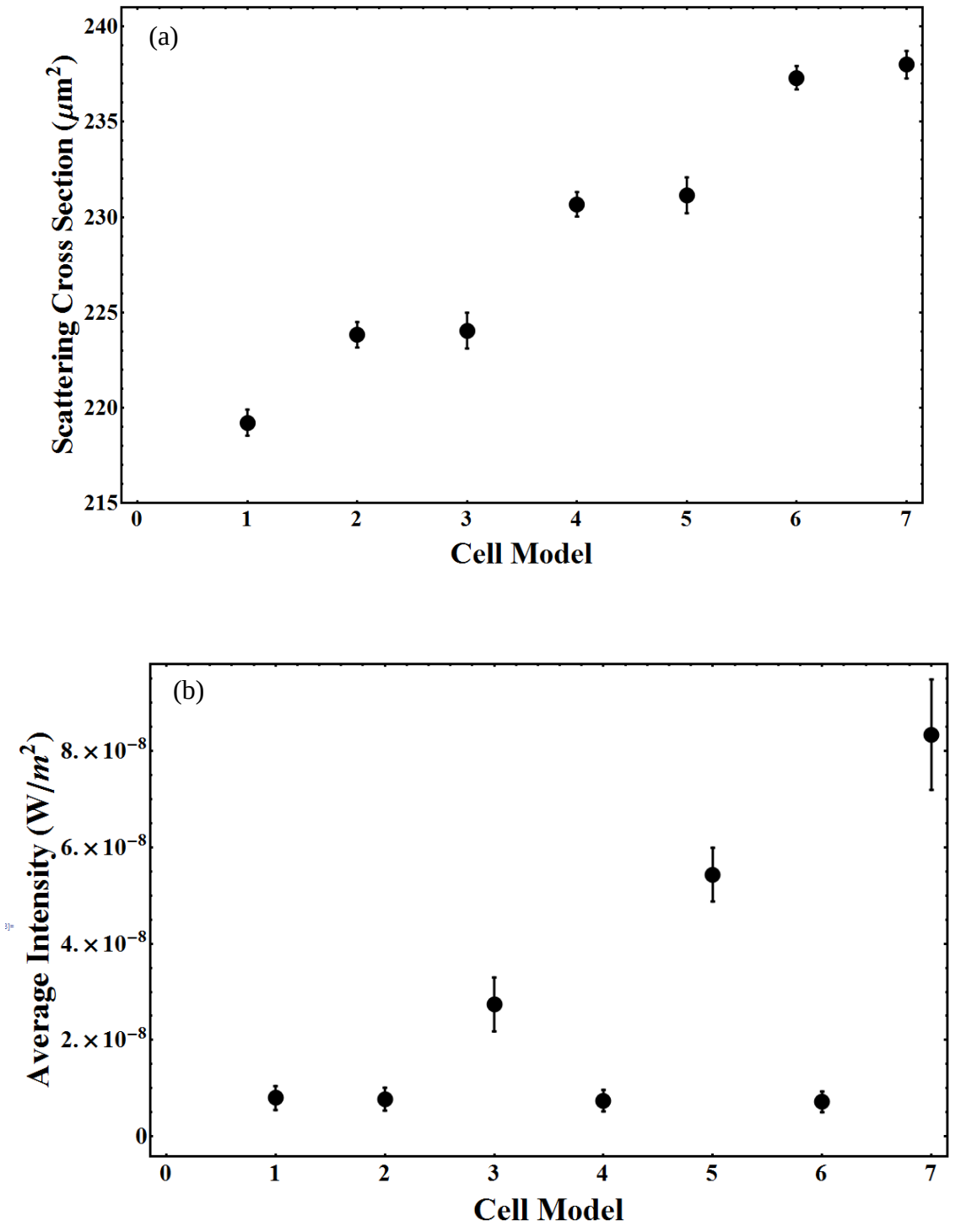

Figure 8.6: Analysis of polarization images for the seven cell models showing the effect of increasing mitochondrial volume density. Results for (a) cross section and (b) the average intensity of the ||⊥ polarization image.

CHAPTER 9: CLASSIFICATION OF CELLS BASED ON MORPHOLOGICAL PARAMETERS

In this chapter, we extend our efforts on correlating light scattering patterns to cell morphology by classifying light scattering patterns according to various morphological characteristics of the cells using discriminant analysis. To accommodate this study, a large set of cell models were created with different cell surface roughness, nuclear size, and mitochondrial distribution, volume density, size, and shape. Light scattering patterns were obtained with ADDA and analyzed with a set of Gabor filters. The results of this study show promise for classifying cells based on a number of morphological characteristics. The following sections describe the methodology and results from the classification of the scattering patterns.

9.1. Simulation methodology

The cell models created for this study were allowed to vary slightly from one another in order to represent the variations in size, shape and optical properties inherent in cell populations. This was achieved through modeling most parameters as random variables with normal distributions, whether or not the particular cell characteristics were a focus of the study.

The cell and nucleus surfaces were modeled as ellipsoids with surface fluctuation. The ellipsoidal shape, controlled by the aspect ratio (AR), the ratio of the major axis to the minor axis, was normally distributed with mean 1.13 ± 0.0339 for the cell and 1.18 ± 0.0354 for the nucleus. These AR values are an average of the values derived from the four B-cells mentioned in §6.6. The cell surface roughness was varied among the cell models to represent relatively smooth, normal, and rough cells. For the cells with normal surface roughness, the parameters chosen for the Gaussian spheres were averages of the parameters derived from the four B-cells.

These parameters were $\ell_{\min} = 2$, $\ell_{\max} = 50$, $\nu = 2.06$, and $\sigma = 0.058$. The differing amounts of surface roughness for the relatively smooth and rough cells were achieved by using Gaussian spheres with different values of σ, based on the roughness parameters given in Ref. [35] as mentioned in §2.2. The values chosen for σ were 0.022 and 0.078 for the smooth and rough surfaces, respectively. The values chosen for the relative standard deviations multiplied by the average cell radius of 5.0 μm yield surface roughness equal to 0.11, 0.29, and 0.39 μm for the three cell surfaces. The surface roughness of the nuclei was kept constant: the Gaussian sphere parameters were $\nu = 2.53$ and $\sigma = 0.064$, based on the parameters derived from the four B-cells. For each model, four different realizations of the Gaussian spheres were used for the cell and nuclei to provide variety while retaining the same statistical features in the shape.

The cell size was modeled with a normal distribution. The mean major axis size was calculated to yield an ellipsoidal volume of 524 μm^3 (corresponding to the volume of a sphere with radius of 5.0 μm) and the standard deviation was such that one standard deviation equaled 3.0% of the volume of the ellipsoid, in order to allow the volume of the cell to vary by approximately $\pm 10\%$.

Three nuclear sizes were modeled to represent small, medium, or large nuclei. The nucleus-to-cell volume fraction expressed as a percentage (N/C) was chosen to be normally distributed with mean of 30%, 40%, or 50%. The standard deviation was such that one standard deviation equaled 2.5% of the N/C. The nucleus was placed at a distance of 0.31 μm from the center of the cell for cells that had a N/C of 0.30 and 0.40 but was placed in the center for cells that had a N/C of 0.50 in order to ensure that the nucleus fit inside the cell.

The nucleus was modeled with a membrane, nucleolus, and optical fluctuations as described in Chapter 6. The nuclear membrane was approximately 0.1 μm thick. The nucleolus was modeled as an ellipsoid with mean axis sizes of 0.6 μm ± 0.1 μm. Each nucleus had a random spatial configuration of refractive indices that corresponds to five levels of index of refraction fluctuations.

The mitochondria in the cell models were modeled with diffuse, peripheral, and perinuclear spatial distributions. For the diffuse distribution, mitochondria were randomly placed in the cytoplasm. For the peripheral distribution, 80.0% of mitochondria were randomly placed within 0.4 μm of the cell periphery (zone 1), 10.0% between 0.4 μm to 0.6 μm (zone 2), 5.0% between 0.6 μm to 0.8 μm (zone 3), and 5.0% between 0.8 μm to 1.2 μm (zone 4) of the cell periphery. The size of zone 1 was sometimes increased up to 0.5 μm to accommodate large mitochondria and high volume densities. The perinuclear distribution was created similarly to the peripheral distribution; it had the same proportions of mitochondria in each zone, but the respective distances were from the nucleus rather than the cell periphery. With this model for the distribution, a cell with a peripheral distribution still had a few mitochondria near the nucleus, and vice versa.

Three mitochondrial volume densities and two mitochondrial sizes and shapes were also modeled. The mitochondria-to-cell volume fraction expressed as a percentage (M/C) was chosen to be normally distributed with mean of 2.0, 5.0, and 8.0%. The standard deviation was such that one standard deviation equaled 5.0% of the M/C. The sizes of the mitochondria were modeled with modified lognormal distributions rather than normal distributions, to restrict the sizes to either mostly small or mostly large and still allow some separation between the two groups. The

lognormal distribution for the semi-major axis a of the small mitochondria, $\ln N(-1.2, 0.3)$, was stretched horizontally by 2.0 and translated on the x-axis by 0.2 μm to allow the smallest mitochondria to have non-zero lengths. The distribution for the large mitochondria $\ln N(-1.2, 0.3)$ was stretched horizontally by 2.0, reflected across the y-axis, and then translated on the x-axis by 1.2 μm to restrict a to be smaller than 0.6 μm. With these distributions for mostly small or mostly large mitochondria, the mean semi-major axes lengths were 0.26 and 0.44 μm, respectively. The shapes of the mitochondria were also modeled with modified lognormal distributions to represent two degrees of elongation. For the less elongated mitochondria, the distribution $\ln N(-1.2, 1.21)$ was translated by 1.0 on the x-axis, resulting in a mean AR of 1.6. For the more elongated mitochondria, the distribution $\ln N(0.3, 0.063)$ was reflected across the y-axis and then translated on the x-axis by 5.0 resulting in a mean AR of 3.6. The probability density functions for the two mitochondrial sizes and shapes are shown in Figure 9.1; the mean for each distribution is represented by a vertical line.

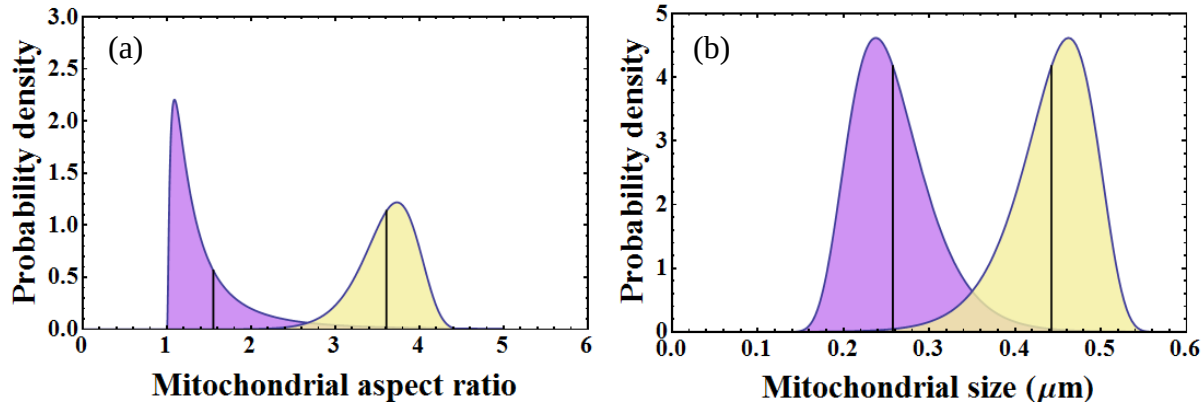

Figure 9.1: Probability density functions used for the modeling of mitochondrial (a) shape and (b) size. The mean for each distribution is represented by a vertical line.

Figure 9.2 presents some examples of the cell models used in this study. Figure 9.2 (a-c) shows the cross sections of a cell model with a 2%, 5%, and 8% mitochondrial volume density, respectively, a relatively smooth surface, a 50% nucleus, and a diffuse mitochondrial distribution with small and less elongated mitochondria. Figure 9.2 (d-f) shows a model a diffuse, peripheral, and perinuclear distribution, respectively, a rough surface, a 30% nucleus, 5% volume density, and large and more elongated mitochondria.

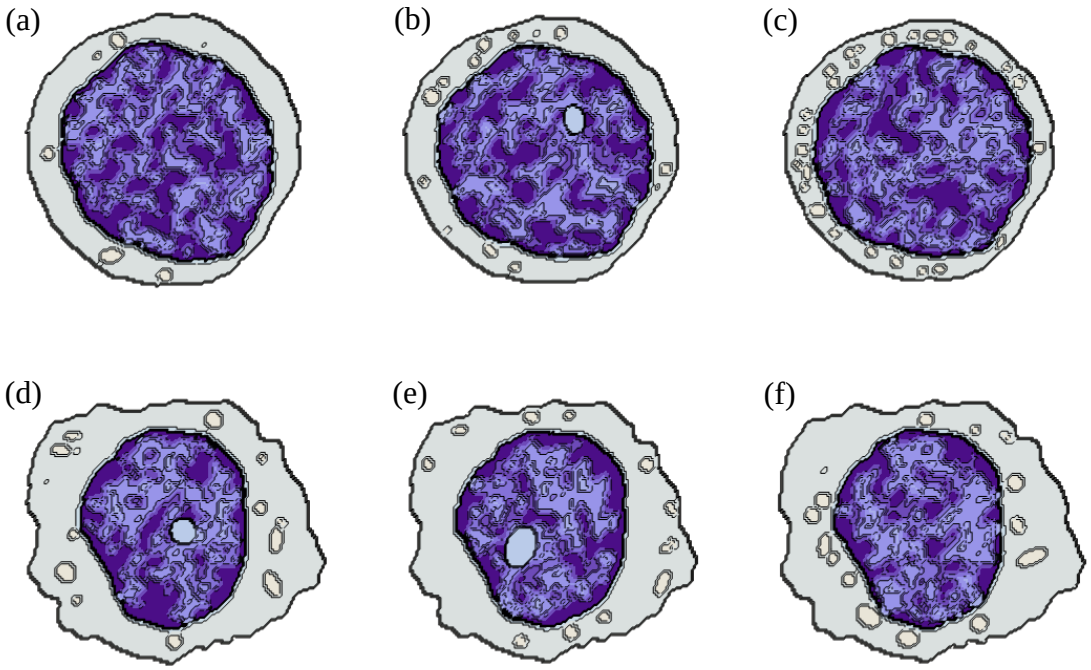

Figure 9.2: Examples of cell models used in simulations. (a,b,c) M/C = 2%, 5%, and 8%, respectively, surface roughness=0.11 μm, N/C = 50%, diffuse distribution, *a*=0.26 μm, and AR=1.6. (d,e,f) Diffuse, peripheral, and perinuclear mitochondrial distributions, respectively, surface roughness=0.39 μm, N/C=30%, M/C=5%, *a*=0.44 μm, and AR=3.6.

In all, with three choices for each of the surface roughness, nuclear size, mitochondrial distribution and volume density, and two choices for each of the mitochondrial sizes and shapes, there were 324 possible cell model combinations. However, due to space limitations in the

peripheral and perinuclear distributions when a large nucleus was modeled, only small mitochondria were modeled for these distributions combined with this nuclear size. Also, again due to space limitations, the rough cell surfaces were only modeled for cells with small and medium nuclei. These limitations reduced the number of cell models to 264. As mentioned above, four Gaussian sphere realizations were used for each cell model; thus, there were a total of 1056 distinct cell models.

For the light scattering simulations using ADDA, the incident field was modeled as a plane wave with wavelength λ = 1.0 μm. The cell was assumed to be in a host medium of water with index of refraction n=1.334. The indices of refraction of each cell component were: $n_{cytoplasm}$=1.3675, n_{nuc_mem}=1.41, $n_{nucleolus}$=1.44, and n_{mito}=1.42. The nucleus was modeled with five levels of index of refraction fluctuations ranging from 1.38 to 1.42 with an average $n_{nucleus}$=1.4. Each cell component had an imaginary index of refraction n=0.000015.

For each scatterer, the Mueller matrix elements were calculated for twenty-four different incident electric field directions. The set of twenty-four incident angles used is listed in Table 9.1.

Table 9.1. Set of twenty-four incident angles for electric field used in simulations

θ_i (°)	ϕ_i (°)	θ_i (°)	ϕ_i (°)	θ_i (°)	ϕ_i (°)	θ_i (°)	ϕ_i (°)
28.4	13.7	127.4	8.1	132.0	171.3	32.9	168.1
40.2	236.7	77.5	326.4	147.0	277.6	85.7	212.8
45.0	135.0	68.3	32.6	146.7	65.5	94.6	149.9
72.0	306.5	127.7	285.0	95.5	230.2	49.9	271.2
77.5	70.2	111.3	80.3	95.2	112.8	66.7	91.4
88.3	187.9	14.1	325.7	111.5	351.5	147.5	194.7

Each of the four realizations for each cell model used a different subset of six orientations from the set of twenty-four orientations presented. Simulating the light scattering from our cell models with twenty-four different incident electric field directions allowed a more realistic representation of cell populations by allowing for differences in cell orientations and also providing an adequate number of samples per cell model for statistical significance when performing discriminant analysis.

In flow cytometry, a single detector is usually placed at the side scattering angle and scattering information in all other directions is lost. Ideally, flow cytometers would contain detectors in directions spanning all space to capture as much 2D scattering information as possible. In this study, polarization scattering patterns were obtained by projecting each Mueller matrix element combination described in §3.2 onto planes 500 μm away in the side angle (center location of plane at $\theta = 90^\circ$ and $\varphi = 90^\circ$) and acute angle ($\theta = 45^\circ$ and $\varphi = 90^\circ$) directions. The half angle subtended by the detector at the lens was approximately 20.0° for the side and acute angle planes. The S_{11} Mueller matrix element was projected in the forward plane with $\theta \approx 1.0 - 5.0^\circ$; this range was chosen to account for the beam-stop present in the experimental setup to prevent the incident light from reaching the detector. The total intensity was calculated for the forward plane. A schematic is shown in Figure 9.3.

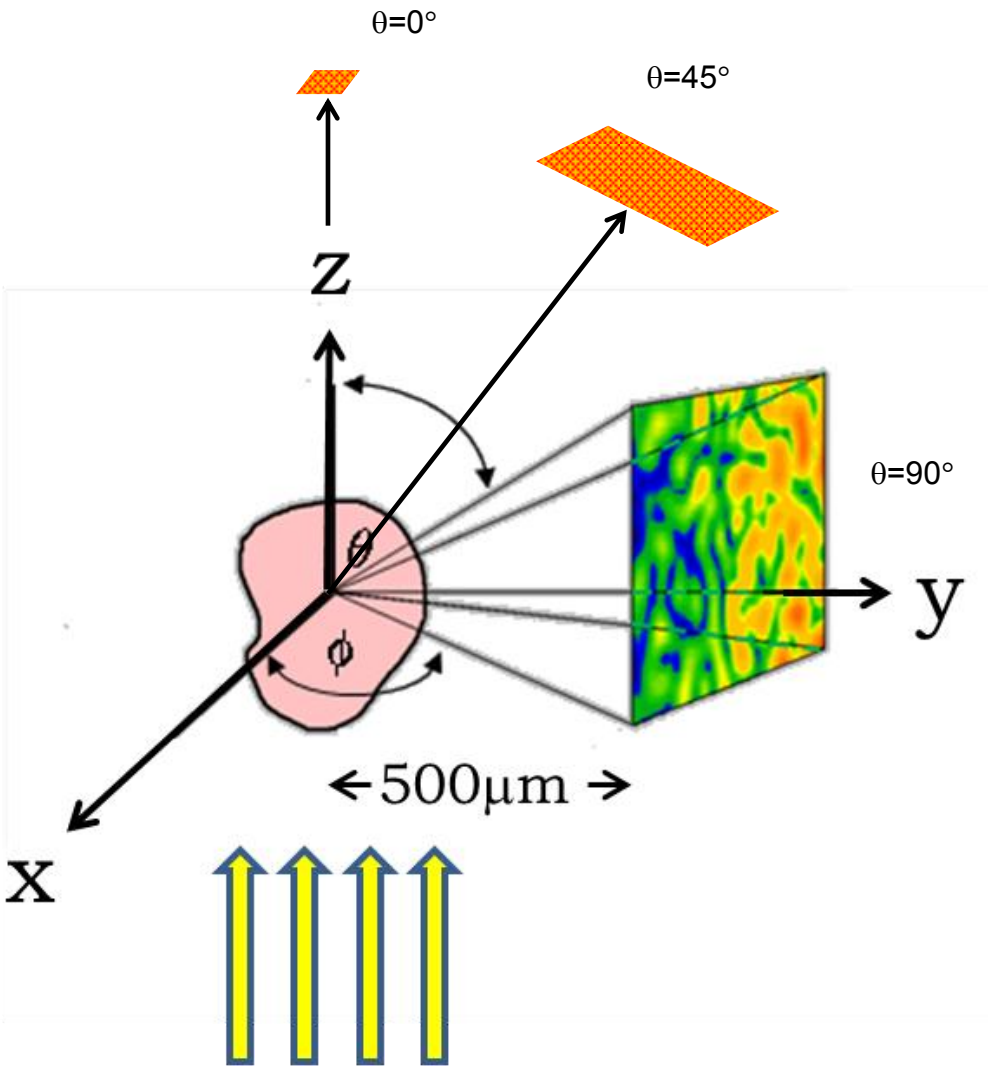

Figure 9.3: Projection image schematic for light scattering simulations. The Mueller matrix elements are projected onto a plane 500 mm away in the side angle ($\theta = 90^{\circ}$ and $\varphi = 90^{\circ}$) and acute angle ($\theta = 45^{\circ}$ and $\varphi = 90^{\circ}$) directions. The total forward intensity is calculated for the forward plane.

The projection images for the six polarization combinations for the side and 45° directions were each analyzed with a set of Gabor filters. Based on the characteristics of the images, four frequencies (0.02, 0.04, 0.08, and 0.16 pixel^{-1}) and four orientations evenly spaced from 0° to

135° were chosen, producing a set of 4x4 Gabor filters. The size of the filter was set to be the size of the image, 101x101 pixels. The arithmetic mean of each Gabor-filtered image was computed. The analysis of each projection image with Gabor filters yielded a 16-element feature vector for each image. Since four projection images (two incident polarizations for each of the side and 45° plane) could be used simultaneously for each cell model, each cell model was represented by a 65-element feature vector, including one element for the forward intensity calculation.

9.2. Results and discussion

Discriminant analysis was performed in order to differentiate between the groups for each cell characteristic. There were a total of 6336 cell models for each analysis. The number of cell models in the groups for each cell characteristic is listed in Table 9.2. The assumptions of DFA were tested. Examination of the variables with histograms of frequency distributions indicated that the variables were either normally distributed or slightly skewed. It was assumed that the large sample sizes made the DFA sufficiently robust that moderate departure from normality could be ignored. Box's M test was found to be significant ($p<0.05$), violating the assumption of homogeneity of covariance matrices. A second analysis was run using the separate-groups covariance matrix. The classification results for both analyses were all within 1%; thus, the results using the pooled covariance matrix were interpreted in the discussion below.

A stepwise analysis was used in determining the LDFs in order to eliminate redundant variables. In this procedure, variables were added to the LDFs one at a time using the method of minimizing Wilk's lambda. Variables were added to the model if the significance level of its F-ratio value was greater than 0.05 and they were removed if it was less than 0.10. For each cell

characteristic grouping, classification accuracies and cross-validated classification accuracies were obtained.

As a check on the classification accuracy values generated by discriminant analysis, we applied each model generated by discriminant analysis to a different data set that was not part of the training sample. The cell models used for the reclassification were similar to the models in the training sample except for the following differences: for the mitochondria spatial distributions, the mitochondria were slightly more spread out in the peripheral and perinuclear distributions; in each cell model, the AR for the mitochondrial shapes was fixed to 2.0 or 3.0; and two mitochondrial sizes were modeled with normal distributions with semimajor axis means of 0.2 and 0.5 μm and standard deviation equal to 2.5% of the respective mean. The number of cell models reclassified for each cell characteristic is also listed in Table 9.2. The scoring wizard in SPSS was used to generate the predicted value for the outcome of interest.

Table 9.2. Summary of number of cell models and groupings

Cell characteristic	Number of cell models in training set	Number of cell models reclassified
Cell surface roughness (μm)		
0.11 (smooth)	2304	72
0.29 (normal)	2304	2280
0.39 (rough)	1728	72
Nuclear size (%)		
30.0 (small)	2592	336
40.0 (medium)	2592	2016
50.0 (large)	1152	72
Mitochondrial distribution		
Diffuse	2304	1080
Peripheral	2016	672
Perinuclear	2016	672
Mitochondrial volume density (%)		
2.0	2112	1080
5.0	2112	672
8.0	2112	672
Mitochondrial size *a* (μm)		
0.26 (small)	3456	648
0.44 (large)	2880	216
Mitochondrial shape AR		
1.6 (less elongated)	3168	1176
3.6 (more elongated)	3168	624

In the results that follow, we present the cross-validated classification accuracies for the training sample, which were all within 1.0% of the classification accuracies. The cross-validated classification accuracies for the various cell parameters were very similar for incident linear polarizations parallel, perpendicular, or at a 45° angle to the scattering plane. Thus, we examine only the results that use the incident perpendicular polarization since they were slightly better overall. Results for incident linear polarizations parallel and at a 45° angle to the scattering plane are presented in Tables B1 and B2 in Appendix B.

Figures 9.4-9.8 present the discriminant analysis classification results for cell surface roughness, nuclear size, and mitochondrial distributions, volume densities, sizes, and shapes, respectively, for the training sample (a) and the test sample (b). As mentioned above, scattering images were obtained and analyzed for the side, 45°, and forward (fwd) scattering planes. For the training sample, the results presented used six different combinations of the scattering planes (side/45°/fwd, side/45°, side/fwd, side, 45°/fwd, and 45°) in order to show the capabilities of the method depending on how much information is available from each scattering plane. For the test set, results are shown for the side/45°/fwd and side scattering planes. For the training sample, the classification accuracies presented are averaged for each grouping of the cell characteristic, while for the test set, the classification accuracies for reclassifying cell models into each group are shown. For the four cell characteristics that have three groupings, i.e., the cell surface roughness, nuclear size, and mitochondrial distributions and volume densities, all possible grouping combinations are presented. For example, for the cell surface roughness, there are results for roughness equal to 0.11/0.29/0.39 μm, 0.11/0.29 μm, 0.29/0.39 μm, and 0.11/0.39 μm. The data labels above the bars are the percentages of correctly-classified subjects and the horizontal line at 50% classification accuracy illustrates the baseline accuracy for two-group classification.

Figure 9.4 compares the classification results for the various groupings of the cell surface roughness. As shown in Figure 9.4(a), there is a decrease in performance when fewer planes are used. In this case, the 45° plane provides slightly better results than the side plane. The classification accuracy is over 70% for all groupings when both the side and 45° planes are used in the analysis, and it is over 75% regardless of the number of planes used when differentiating between roughness equal to 0.11/0.29 μm and 0.11/0.39 μm. The results suggest that cells that

are relatively smooth can successfully be separated from cells that have either average or high levels of surface roughness. The classification results for the individual groups in Figure 9.4(b) support this finding. Reclassification into two groups of smooth and non-smooth cells (roughness values of 0.11/0.29 μm and 0.11/0.39 μm) is over 70% and the reclassification of relatively smooth cells ranges from 81-100% regardless of the number of groups in the classification.

Figure 9.5 presents the classification results for the nuclear size. In Figure 9.5(a), it is evident that the forward plane helps to distinguish between the groups as the results that include the forward plane are consistently higher than those without the forward plane. For the two-group classifications, the results with the forward plane are all above 70%. The results for the side and 45° planes are comparable. Like in the previous figure, the results increase by over 20% when only classifying between the extremes of the three groups (N/C= 30% and 50%) rather than classifying three sizes of the nucleus. The results in Figure 9.5(b) for the test set are very poor for reclassifying both the medium and large nuclear sizes. A closer look at the data (not shown) revealed that the nuclear size was usually reclassified one size smaller. For example, in the 3-group classification, there was a 98% chance that the medium nucleus was reclassified as either small or medium using the side/45°/fwd scattering planes, compared to a 28% chance that it was reclassified as medium. There was a 78% chance that the large nucleus was reclassified as medium or large rather than an 8% chance that it was reclassified as large.

The results of mitochondrial distribution classification are shown in Figure 9.6. Like the results for the cell surface roughness, the inclusion of all planes produces better classification accuracies and the 45° plane performs better than the side plane, as shown in Figure 9.6(a). The classification results are higher for distinguishing between a peripheral and perinuclear

distribution, since in these two groups the mitochondria have more separation between them. Again, the classification of these two outermost groups increases the performance by over 20% compared to the classification of the three groups. The results also suggest that the peripheral distribution is easier to classify since the results for diffuse/peripheral are higher than for diffuse/perinuclear. This implies that the mitochondria have a more significant effect on the light scattering pattern when they are located near the cell periphery. The results for the reclassification of cell models in the test set in Figure 9.6(b) follow the same trend as those in (a). The performance is poor when attempting to classify the three mitochondrial distributions but it increases for the two-group classification, especially for the peripheral/perinuclear grouping.

Figure 9.7 presents the classification results for mitochondrial volume density. In this case, the results from the side plane are higher than those from the 45° plane, as shown in Figure 9.7 (a). Again, the results increase significantly when only mitochondria with M/C=2.0 and 8.0% are classified rather than all three volume densities. Also, the classification of M/C = 2.0/5.0% is significantly higher than that of M/C=5.0/8.0%. This could be due to the larger separation between the 2.0 and 5.0 % groups, since these groups have smaller variances than the 8.0% group. Overall, the model is effective in distinguishing between mitochondrial volume density, with a classification accuracy over 75% when all scattering planes are used in the analysis regardless of the grouping. The results in Figure 9.7 (b) are consistent with those in Figure 9.7 (a). Cell models are reclassified with over 85% accuracy for the M/C = 2.0/5.0% and M/C = 2.0/8.0% and the inclusion of all the planes produces better results.

The classification results for both the shape and size of the mitochondria are shown in Figure 9.8. Both of these cell characteristics have only two groupings; less (AR=1.6) or more (AR=3.6)

elongated for the shape, and small (a=.26 μm) or large (a=0.44 μm) mitochondria for the size. The model does a poor job of classifying mitochondrial shape; regardless of the number of planes, the accuracy for both sets of data ranges from 42-63%. However, the model excels at classifying mitochondrial size; even with only one scattering plane used for the analysis, the classification accuracy is above 75% and 80%, respectively, for the training and test sets.

In summary, classification of cell models in the sample set and reclassification of cell models based on the models generated from the training set was highly successful for the cell surface roughness grouping of 0.11/0.39 μm, the mitochondrial volume density groupings of M/C=2.0/5.0% and M/C=2.0,8.0%, and mitochondrial size grouping: over 80% of the cell models were correctly classified into their original categories using either all the scattering planes or the side scattering plane. The average classification accuracy for each possible grouping combination for each cell characteristics is presented in Table 9.3. Results are shown for the training set and the test set using data from all scattering planes or the side scattering plane. Overall, the reclassification of the test set was comparable to the classification of the training set, with the exception of the reclassification of the nuclear size. Overall, discriminant analysis performed well using all of the scattering planes in classifying all the cell characteristics except for the mitochondrial shape.

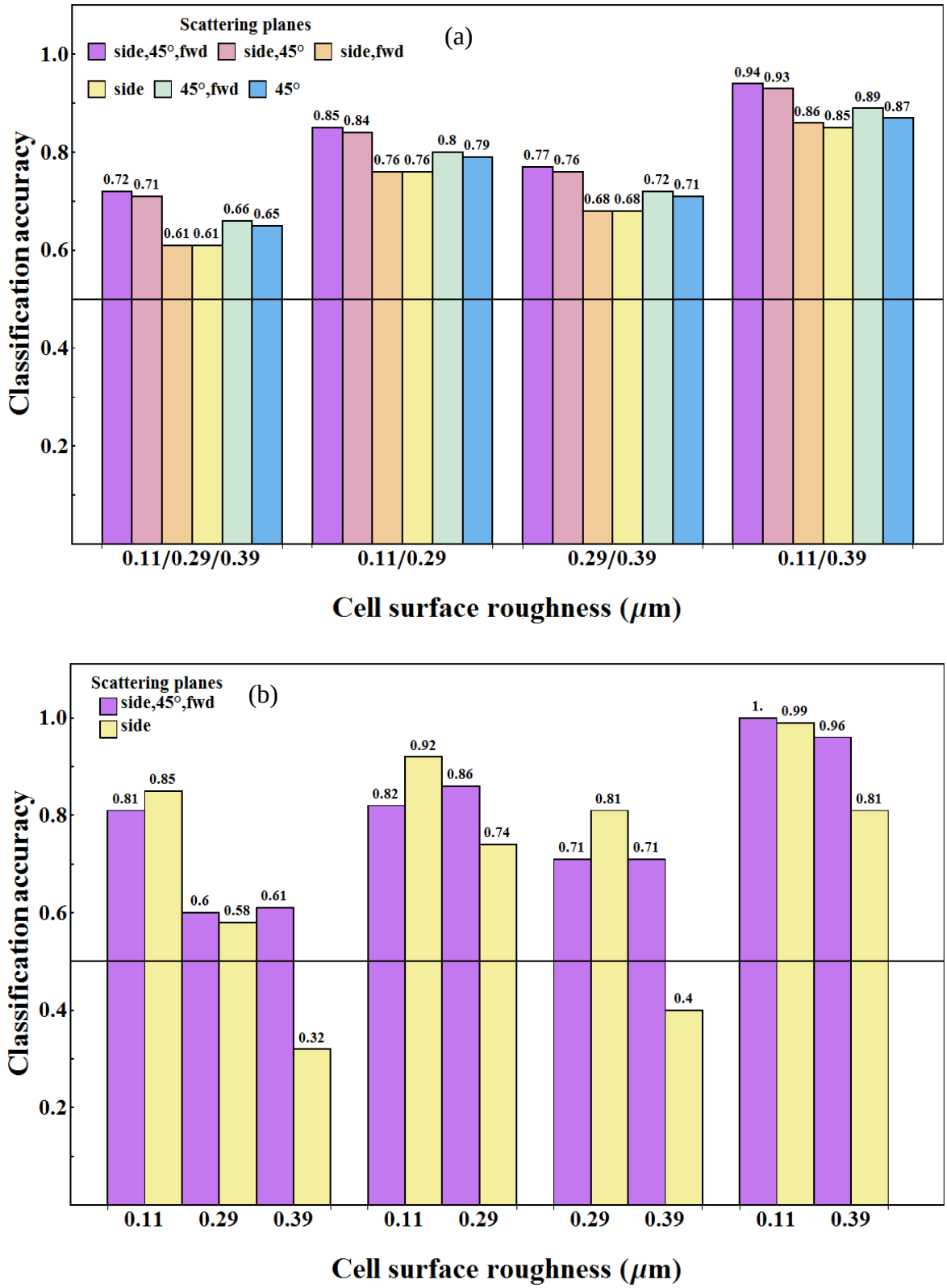

Figure 9.4: Classification results from discriminant analysis for cell surface roughness for (a) the training set and (b) the test set.

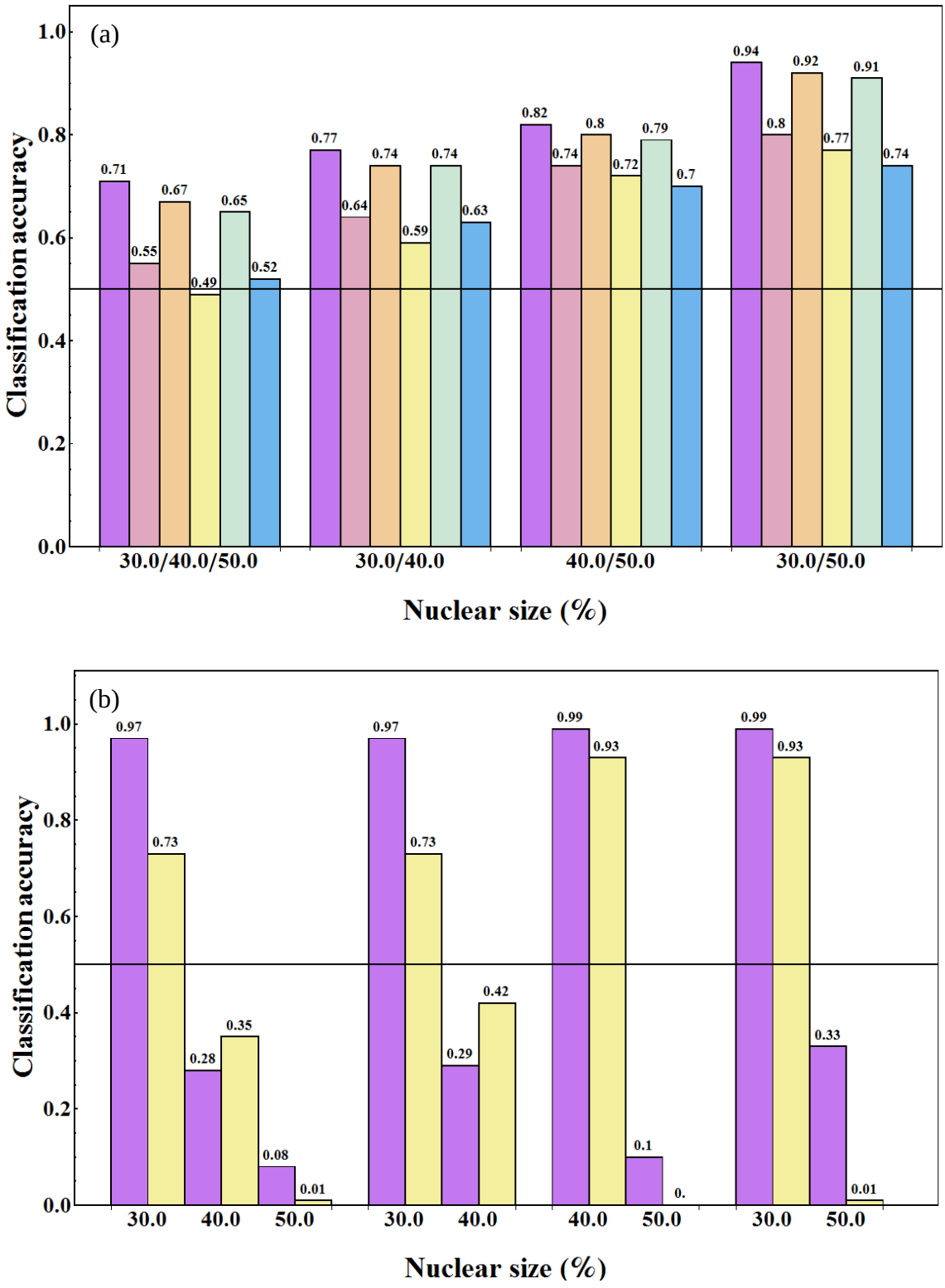

Figure 9.5: Classification results from discriminant analysis for nuclear size for (a) the training set and (b) the test set.

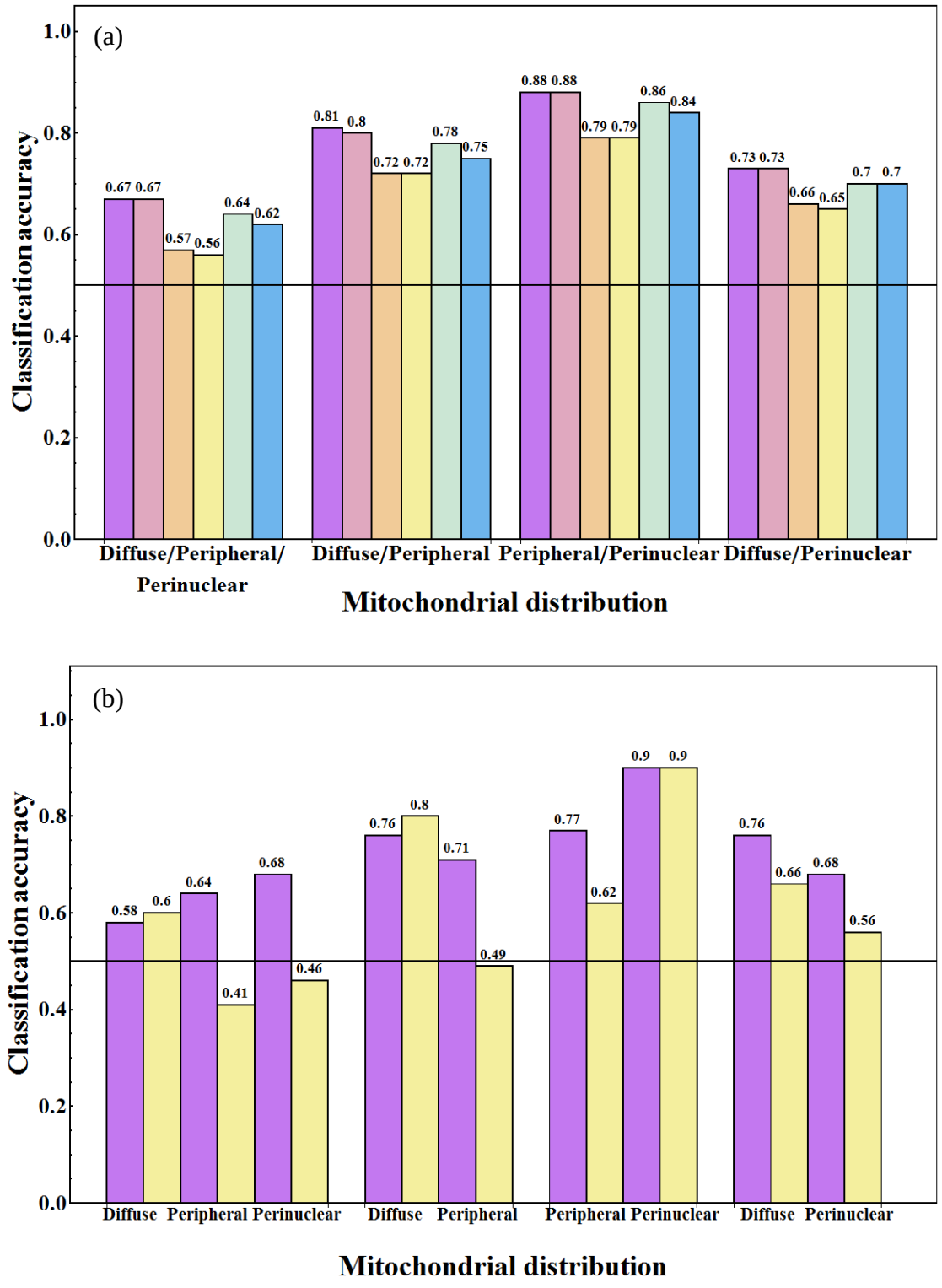

Figure 9.6: Classification results from discriminant analysis for mitochondrial distribution for (a) the training set and (b) the test set.

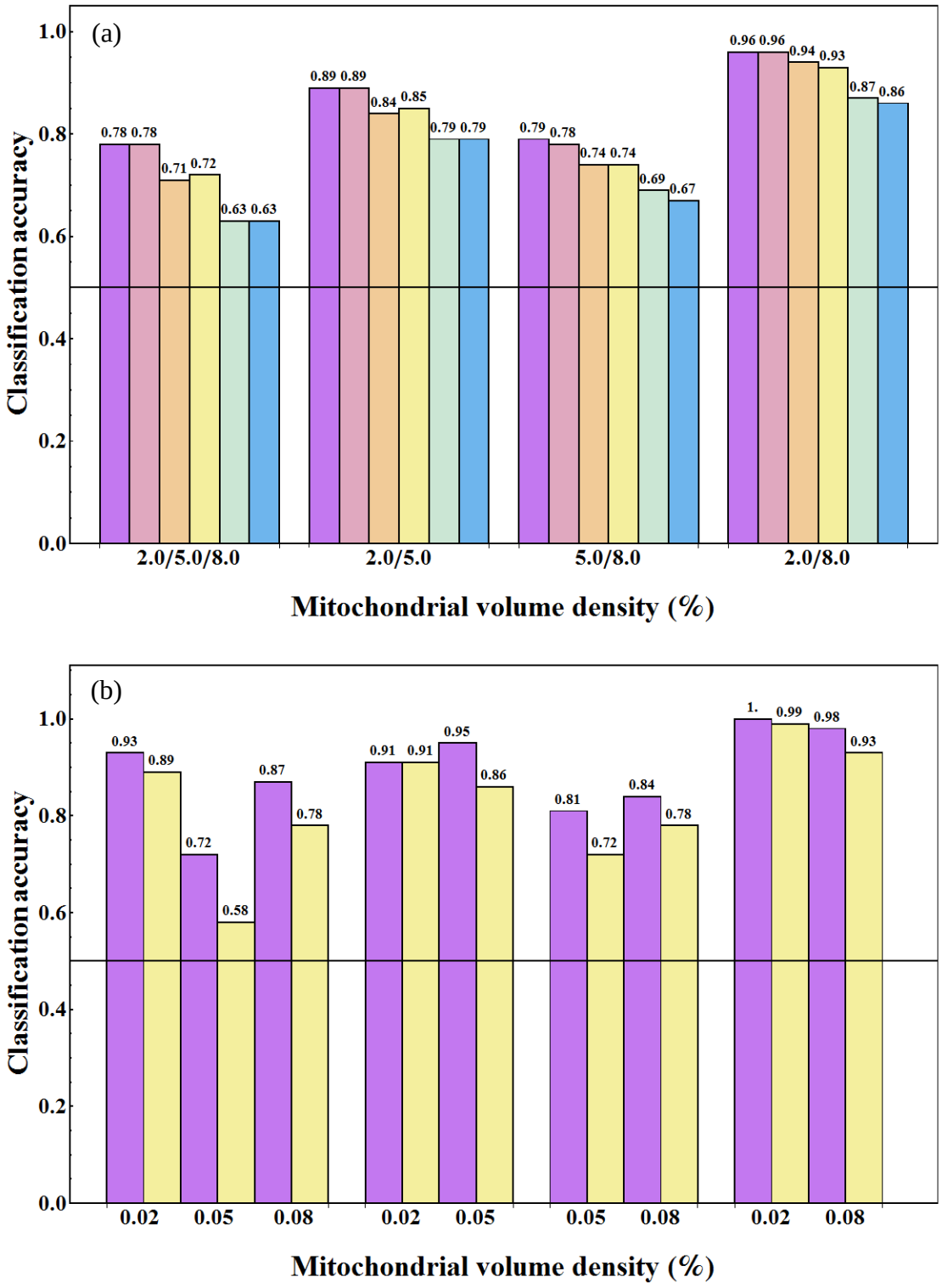

Figure 9.7: Classification results from discriminant analysis for mitochondrial volume density for (a) the training set and (b) the test set.

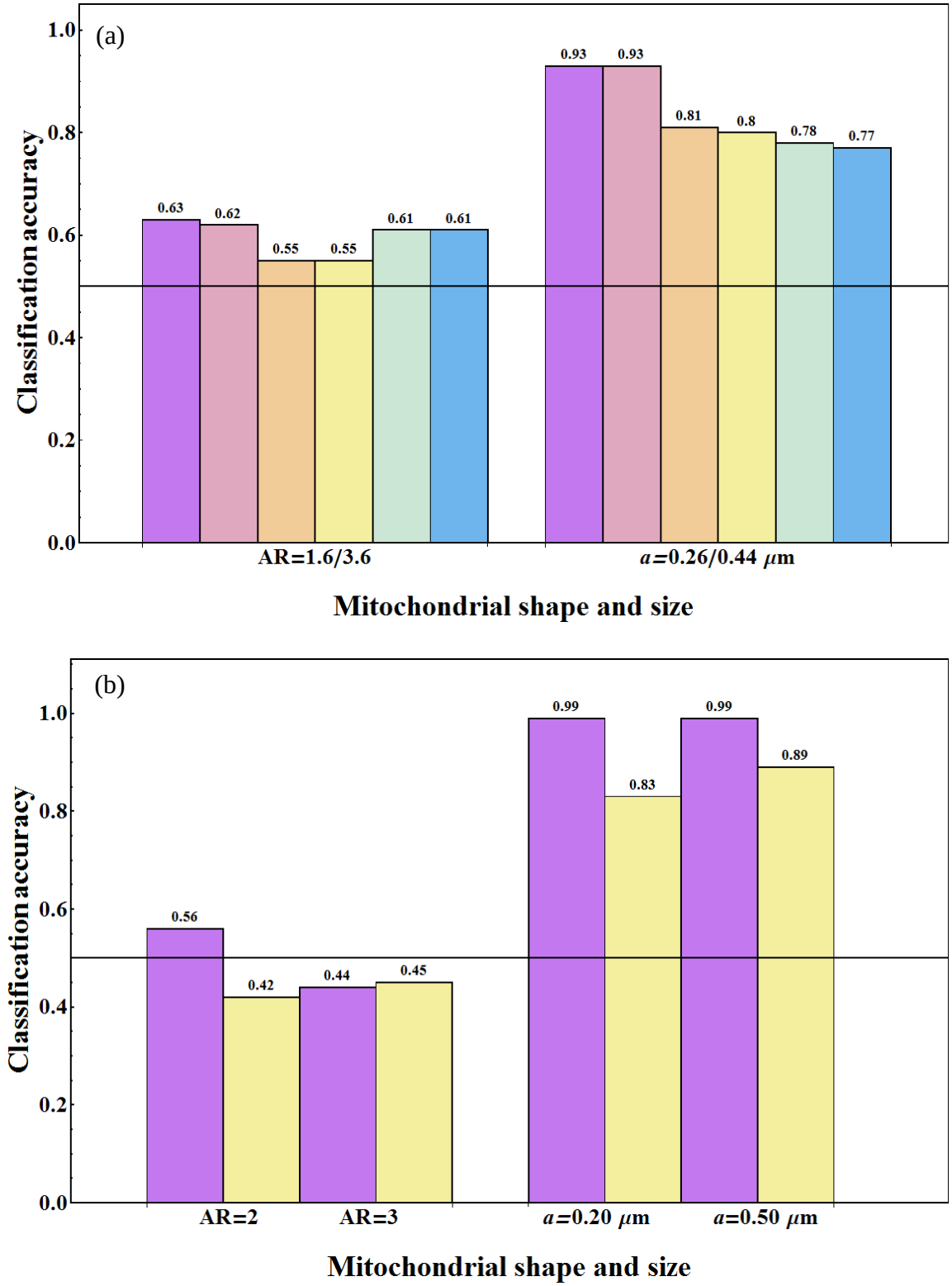

Figure 9.8: Classification results from discriminant analysis for mitochondrial shape and size for (a) the training set and (b) the test set.

Table 9.3. Classification accuracy for training set and test set for various cell characteristics

Cell characteristic	All scattering planes		Side scattering plane	
	Training set	Test set	Training set	Test set
Cell surface roughness (μm)				
0.11/0.29/0.39	0.72	0.67	0.61	0.58
0.11/0.29	0.85	0.84	0.76	0.83
0.29/0.39	0.77	0.71	0.68	0.60
0.11/0.39	0.94	0.98	0.85	0.90
Nuclear size (%)				
30.0/40.0/50.0	0.71	0.44	0.49	0.36
30.0/40.0	0.77	0.63	0.59	0.57
40.0/50.0	0.82	0.54	0.72	0.46
30.0/50.0	0.94	0.66	0.77	0.47
Mitochondrial distribution				
Diffuse/Peripheral/Perinuclear	0.67	0.63	0.56	0.49
Diffuse/Peripheral	0.81	0.74	0.72	0.64
Peripheral/Perinuclear	0.88	0.84	0.79	0.76
Diffuse/Perinuclear	0.73	0.72	0.65	0.61
Mitochondrial volume density (%)				
2.0/5.0/8.0	0.78	0.84	0.72	0.75
2.0/5.0	0.89	0.93	0.85	0.88
5.0/8.0	0.79	0.82	0.74	0.75
2.0/8.0	0.96	0.98	0.93	0.96
Mitochondrial size *a* (μm)				
0.26/0.44 (training)	0.93	0.99	0.8	0.86
0.20/0.50 (test)				
Mitochondrial shape AR				
1.6/3.6 (training)	0.63	0.50	0.55	0.44
2.0/3.0 (test)				

CHAPTER 10: CONCLUSION

This research project investigated the relationship between the light scattering patterns from cells and their morphology. Through realistic analytical cell modeling and analysis of light scattering patterns with various techniques, this study demonstrated the potential of the light scattering signal as a tool for differentiating cells based on particular morphological characteristics.

The procedure presented to create analytical cell models used structural information extracted from confocal microscopic images of biological cells. The shapes of the cell and nucleus membranes were constructed by combining an ellipsoidal base shape with a Gaussian random sphere model for the surface fluctuation, and nuclear substructures and mitochondria populations with specific densities, distributions, sizes, and shapes were also added to the cell model. The procedure to extract the surface fluctuation was validated through the generation of a large set of Gaussian spheres and the successful recovery of the Gaussian sphere parameters within 10% of the original parameters. In addition, light scattering patterns obtained through simulation from the cell models and experimentally from lymphocytes showed similar characteristics such as speckle size and configuration, indicating strong similarities between the analytical models and biological cells. The analytical cell models allowed systematic variations in cell structural features in a controlled manner and made the systematic study of the relationship between light scattering patterns and cell morphology possible.

To determine the best way to extract cell morphology information from the light scattering patterns, methods to analyze the light scattering patterns were compared for their ability to distinguish between cell models with different shapes and mitochondrial characteristics. It was found that the analysis of the angular distribution of the scattered light combined with Gabor filter analysis were most helpful in differentiating between the cell characteristics. Additionally,

it was shown that different scattering angle ranges from the angular distribution of the scattered light provided information about different parts of the cell, such as the main cell structure and the mitochondrial spatial distribution, volume density, size and shape. In particular, the light scattering intensity in the scattering angle range of 25° - 45° responded to changes in the surface fluctuation of the cell and the range of 90° - 110° was well suited for characterization of mitochondrial density and nuclear size. Gabor analysis of the diffraction images produced from side angle scattering suggested that Gabor filters could distinguish between different mitochondrial spatial distributions. This part of the study identified relevant scattering angle ranges and demonstrated the effectiveness of different analysis methods for analyzing light scattering patterns from realistic cell models.

The study of the correlation between changes in cell morphology to changes in the light scattering patterns was achieved through a visual inspection and quantitative analysis of the scattering patterns. By systematically increasing the complexity of nuclear substructures and modeling the cells with surface fluctuation and mitochondria, we were able to relate the changes in the scattering patterns to variations in particular cell characteristics. In particular, there was a noticeable change in the size and formation of the speckles in the light scattering patterns due to increasing the complexity of the nucleus in cell models with smooth surfaces and introducing mitochondria in cell models with surface fluctuation. Quantitative analysis revealed an increase in Gabor energy of the light scattering patterns for high filter frequencies due to the increased complexity of the nucleus model in all cell models. Results also indicated that the average intensity of the polarization images can provide an indication of mitochondrial volume density. These results suggested that a complex nuclear structure and mitochondria should be included when modeling biological cells for light scattering simulations.

The last part of this project examined the capabilities of discriminant analysis and Gabor filters in classifying light scattering patterns according to various cell morphological characteristics. Cell models were created with different surface roughness, nuclear size, and mitochondrial spatial distribution, volume density, size, and shape and sets of polarization images for different incident field directions were obtained in the side and 45° scattering angle directions. With the light scattering data from the forward, 45°, and side planes combined for the discriminant analysis, polarization images from realistic cell models with different cellular characteristics were classified with over 87% accuracy. The best classification results were obtained for discriminating between cell surface roughness and mitochondrial size, while the only parameter that was not classified successfully was the mitochondrial shape. The study showed that regardless of the polarization of the incident field, a Gabor filter analysis of polarization images from the side and 45° scattering angle combined with the forward light scattering intensity provided variables with significant discriminatory power in a discriminant analysis to classify the cells according to the different cell characteristics.

The methods proposed in this study for the cell modeling and light scattering pattern analysis have proved useful in elucidating more specific relationships between the cell characteristics and the light scattering patterns. It is expected that these methods could be utilized in flow cytometry to sort cells according to the desired characteristics. For example, experimentalists could use the results of this study to decide on the location of the detector(s) that would be most useful to them depending on the information desired from the cell. If one is studying the mitochondrial distribution in cells due to its association with cancer and only one detector is available, for instance, results of this study suggest placing the detector at the 45° scattering angle to obtain the most relevant information.

Additional work is suggested for improving the realistic cell model and the classification of cells based on morphological characteristics. Further directions for realistic cell modeling include modeling additional structures in the cytoplasm, such as the Golgi complex and the endoplasmic reticulum. The procedure presented in this work can be directly applied to model these substructures provided that cross sectional images are available. Also, it would be very helpful to relate the findings in this study to experimental results. Current work is underway comparing light scattering images from biological cells obtained through experiment to those simulated from the analytic cell models presented in this study. In addition, the classification study can be expanded. For each cell characteristic, two or three groups were created based on the information available in the literature relating these characteristics to the cell physiological condition. Thus, the discriminant models could only be used to classify cell models that belonged to the groups rather than any cell model from the cell population. For a more complete study, it is suggested that a number of cell models in the hundreds of thousands be created to encompass a wider variety of cells. As the relationship between cell morphology and certain diseases becomes clearer, the methods presented in this work may have wide possibilities for clinical applications.

REFERENCES

[1] K. Dong, Y. Feng, K. M. Jacobs, J. Q. Lu, R. S. Brock, L. V. Vang, F. E. Bertrand, M. A. Farwell and X. H. Hu, "Label-free classification of cultured cells through diffraction imaging," *Biomed. Opt. Express,* vol. 2, pp. 1717-1726, 2011.

[2] V. Backman, *Early Diagnosis of Cancer Using Light Scattering Spectroscopy,* Ph.D. Thesis, Massachusetts Institute of Technology, 2001.

[3] P. J. Wyatt, "Differential light scattering: a physical method for identifying living bacterial cells," *Appl. Opt,* vol. 7, pp. 1879-1896, 1968.

[4] P. F. Mullaney and P. N. Dean, "The small angle light scattering of biological cells," *Biophys. J.,* vol. 10, pp. 764-772, 1970.

[5] A. Brunsting and P. F. Mullaney, "Light scattering from coated spheres: model for biological cells," *Applied Optics,* vol. 11, pp. 675-680, 1972.

[6] P. J. Wyatt and D. T. Phillips, "Structure of single bacteria from light scattering," *J. Theor. Biol.,* vol. 37, pp. 493-501, 1972.

[7] P. J. Wyatt, "Cell wall thickness, size distribution, refractive index ratio and dry weight content of living bacteria," *Nature,* vol. 226, pp. 277-279, 1970.

[8] J. R. Mourant, T. M. Johnson, S. Carpenter, A. Guerra, T. Aida and J. P. Frever, "Polarized angular dependent spectroscopy of epithelial cells and epithelial cell nuclei to determine the size scale of scattering structures," *J. Biomed. Optics,* vol. 7, pp. 378-387, 2002.

[9] A. Dunn and R. Mourant, "Three-dimensional computation of light scattering from cells," *IEEE J. Selected Topics in Quantum Electronics,* vol. 2, no. 4, 1996.

[10] S. Saltsberger, I. Steinberg and I. Gannot, "Multilayer mie scattering model for investigation of intracellular structural changes in the nucleolus and cytoplasm," *International Journal of Optics,* 2012.

[11] A. Zharinov, P. Tarasov, A. Shvalov, K. Semyanov, D. R. van Bockstaele and V. Maltsev, "A study of light scattering of mononuclear blood cells with scanning flow cytometry," *J. of Quant. Spect. & Rad. Trans.,* vol. 102, pp. 121-128, 2006.

[12] M. Kalashnikov, W. Choi, C. C. Yu, Y. Sung, R. R. Dasari, K. Badizadegan and M. S. Feld, "Assessing light scattering of intracellular organelles in single intact living cells," *Optics*

Express, vol. 17, pp. 19674-19681, 2009.

[13] X. Li, Z. Chen, A. Taflove and V. Backman, "Equiphase-sphere approximation for light scattering by stochastically inhomogeneous microparticles," *Phys. Rev. E,* vol. 70, 2004.

[14] M. A. Yurkin, K. A. Semyanov, P. A. Tarasov, A. V. Chernyshev, A. G. Hoekstra and V. P. Maltsev, "Experimental and theoretical study of light scattering by individual mature red blood cells by use of scanning flow cytometry and discrete dipole approximation," *App. Opt.,* vol. 44, no. 25, pp. 5249-5256, 2005.

[15] R. S. Brock, X. H. Hu, D. A. Weidner, J. R. Mourant and J. Q. Lu, "Effect of detailed cell structure on light scattering distribution: FDTD study of a B-cell with 3D structure constructed from confocal images," *JQSRT,* vol. 102, pp. 25-36, 2006.

[16] J. R. Mourant, M. Canpolat, C. Brocker, O. Esponda-Ramos, T. M. Johnson, A. Matanock, K. Stetter and J. P. Freyer, "Light scattering from cells: the contribution of the nucleus and the effects of proliferative status," *J. Biomed. Opt.,* vol. 5, pp. 131-137, 2000.

[17] R. Drezek, M. Guillaud, T. Collier, I. Boiko, A. Malpica, C. Macaulay, M. Follen and R. Richards-Kortum, "Light scattering from cervical cells throughout neoplastic progression: influence of nuclear morphology, DNA content, and chromatin texture," *J. Biomed. Opt.,* vol. 8, pp. 7-16, 2003.

[18] H. Ding, J. Q. Lu, R. S. Brock, T. J. McConnell, J. F. Ojeda, K. M. Jacobs and X. H. Hu, "Angle-resolved Mueller matrix study of light scattering by B-cells at three wavelengths of 442, 633 and 850 nm," *J. Biomed. Opt.,* vol. 12, p. 034032, 2007.

[19] J. Q. Lu, P. Yang and X. H. Hu, "Simulations of light scattering from a biconcave red blood cell using the Finite-Difference Time-Domain method," *J. Biomed Opt.,* vol. 10, p. 024022, 2005.

[20] X. Su, W. Rozmus and Y. Y. Tsui, "Wide angle light scattering differentiation of organelle size particle distributions in whole cells," *Cytometry A.,* vol. 77, no. 6, pp. 580-584, 2010.

[21] X. T. Su, C. Capjack, W. Rozmus and C. Backhouse, "2D light scattering patterns of mitochondria in single cells," *Opt. Express,* vol. 15, no. 17, pp. 10562-10575, 2007.

[22] X. T. Su, K. Singh, W. Rozmus, C. Backhouse and C. Capjack, "Light scattering characterization of mitochondrial aggreagation in single cells," *Opt. Express,* vol. 17, pp. 13381-13388, 2009.

[23] X. Su, Y. Qiu, L. Marquez-Curtis, M. Gupta, C. E. Capjack, W. Rozmus, A. Janowska-Wieczorek and Y. Y. Tsui, "Label-free and noninvasive optical detection of the distribution of nanometer-size mitochondria in single cells," *J. Biomed. Opt.*, vol. 16, p. 067003, 2011.

[24] R. M. Haralick, K. Shanmugam and I. Dinstein, "Textural features for image classification," *IEEE Trans, Systems, Man, and Cybernetics SMC*, vol. 3, pp. 610-621, 1973.

[25] K. I. Laws, Textured Image Segmentation, Ph.D. Thesis, University of Southern California, 1980.

[26] P. M. Pilarski, X. T. Su, D. M. Glerum and C. J. Backhouse, "Computational analysis of mitochondrial placement and aggregation effects on wide-angle cell scattering patterns," *Proc. SPIE,* vol. 7187, p. 71870J, 2009.

[27] P. M. Pilarski and C. J. Backhouse, "Towards robust cellular image classification; theoretical foundations for wide-angle scattering pattern analysis," *Biomed. Opt. Express,* vol. 1, no. 4, pp. 1225-1233, 2010.

[28] V. A. Loiko, G. I. Ruban, O. A. Gritsai, A. D. Gruzdev, S. M. Kosmacheva, N. V. Goncharova and A. A. Miskevich, "Morphometric model of lymphocyte as applied to scanning flow cytometry," *Journal of QSRT,* vol. 102, no. 1, pp. 73-84, 2006.

[29] G. I. Ruban, S. M. Kosmacheva, N. V. Goncharova, D. Van Bockstaele and V. A. Loiko, "Investigation of morphometric parameters for granulocytes and lymphocytes as applied to a solution of direct and inverse light scattering problems," *J. Biomed Opt.,* vol. 12, no. 4, p. 044017, 2007.

[30] S. Johnsen and E. A. Widder, "The physical basis of transparency in biological tissue: ultrastructure and the minimization of light scattering," *J. Theor. Biol.,* vol. 199, no. 2, pp. 181-198, 1999.

[31] R. Drezek, A. Dunn and R. Richards-Kortum, "Light scattering from cells: finite-difference time-domain simulations and goniometric measurements," *Applied Optics,* vol. 38, no. 16, pp. 3651-3661, 1999.

[32] G. I. Ruban, W. Berdnik, D. V. Marinitch, N. V. Goncharova and V. A. Loiko, "Light scattering and morphology of the lymphocyte as applied to flow cytometry for distinguishing healthy and infected individuals," *Journal of Biomedical Optics,* vol. 15, no. 5, p. 057008, 2010.

[33] S. Majstoravich, J. Zhang, S. Nicholson-Dkysktra, S. Linder, W. Friedrich, K. A. Siminovitch and H. N. Higgs, "Lymphocyte microvilli are dynamic, actin-dependent structures that do not require Wiskott-Aldrich syndrome protein (WASp) for their morphology," *Blood,* vol. 104, no. 5, pp. 1396-1403, 2004.

[34] G. W. Schmid-Schonbein, Y. Y. Shih and S. Chien, "Morphometry of human leukocytes," *Blood,* vol. 56, no. 5, pp. 866-875, 1980.

[35] H. Jin, H. Zhao, L. Liu, J. Jiang, X. Wang, S. Ma and J. Cai, "Apoptosis induction of K562 cells by lymphocytes: An AFM study," *Scanning,* vol. 35, no. 1, pp. 7-11, 2013.

[36] P. Wang, R. K. Bista, W. Qiu, W. E. Khalbuss, L. Zhang, R. E. Brand and Y. Liu, "An insight into statistical refractive index properties of cell internal structure via low-coherence statistical amplitude microscopy," *Opt. Express,* vol. 18, no. 21, pp. 21950-8, 2010.

[37] D. Zink, A. H. Fisher and J. A. Nickerson, "Nuclear structure in cancer cells," *Nat. Rev. Cancer,* vol. 4, no. 9, pp. 677-87, 2004.

[38] N. E. Abdelmequid and S. G. Kourtian, "Subcellular disorders associated with autism peripheral blood," *Asian Journal of Biological Sciences,* vol. 5, no. 5, pp. 221-239, 2012.

[39] J. S. Modica-Napolitano and K. K. Singh, "Mitochondria as targets for detection and treatment of cancer," *Expert Reviews in Molecular medicine,* vol. 4, no. 9, pp. 1-19, 2004.

[40] W. J. Koopman, H. J. Visch, S. Verkaart, L. W. van den Heuvel, J. A. Smeitink and P. H. Willems, "Mitochondrial network complexity and pathological decrease in complex I activity are tightly correlated in isolated human complex I deficiency," *Am J. Physiol. Cell Physiol.,* vol. 289, no. 4, pp. C881-90, 2005.

[41] A. M. Cataldo, D. L. McPhie, N. T. Lange, S. Punzell, s. Elmiligy, N. Z. Ye, M. P. Froimowitz, L. C. Hassinger, E. B. Menesale, L. W. Sargent, D. J. Logan, A. E. Carpenter and B. M. Cohen, "Abnormalities in mitochondrial structure in cells from patients with bipolar disorder," *Am. J. Pathol.,* vol. 177, no. 2, pp. 575-85, 2010.

[42] P. L. Gourley, J. K. Hendricks, A. E. McDonald, R. G. Copeland, K. E. Barrett, C. R. Gourley and R. K. Naviaux, "Ultrafast nanolaser flow device for detecting cancer in single cells," *Biomed Microdevices,* vol. 7, no. 4, pp. 331-9, 2005.

[43] S. Campello and L. Scorrano, "Mitochondrial shape changes: orchestrating cell pathophysiology," *EMBO Rep.,* vol. 11, no. 9, pp. 678-84, 2010.

[44] J. Bereiter-Hahn and M. Voth, "Dynamics of Mitochondria in Living Cells: Shape Changes, dislocations, fusion, and fission of mitochondria," *Microsc. Res. Tech.,* vol. 27, no. 3, pp. 198-219, 1994.

[45] N. Uranova, P. Bonartsev, O. Brusov, M. Morozova, V. Rachmanova and D. Orlovskaya, "The ultrastructure of lymphocytes in schizophrenia," *The World Journal of Biological Psychiatry*, vol. 8, no. 1, pp. 30-37, 2007.

[46] T. Ahmad, K. Aggarwal, B. Pattnaik, S. Mukherjee, T. Sethi, B. K. Tiwari, M. Kumar, A. Micheal, U. Mabalirajan, B. Ghosh, R. S. Sinha and A. Agrawal, "Computational classification of mitochondrial shapes reflects stress and redox state," *Cell Death Dis.,* vol. 4, p. e461, 2013.

[47] L. C. Gomes, G. Di Benedetto and L. Scorrano, "During autophagy mitochondria elongate, are spared from degradation and sustain cell viability," *Nature Cell Biology,* vol. 13, pp. 589-598, 2011.

[48] A. M. Villa and S. M. Doglia, "Mitochondria in tumor cells studied by laser scanning confocal microscopy," *J. Biomed.,* vol. 9, no. 2, pp. 385-394, 2004.

[49] L. Packer, "Size and shape transformations correlated with oxidative phosphorylation in mitochondria. I. Swelling-shrinkage mechanisms in intact mitochondria," *J. Cell Biol.,* vol. 18, pp. 487-494, 1963.

[50] J. H. Jarvis and A. Jacobs, "Morphological abnormalities in lymphocyte mitochondria associated with iron-deficiency anaemia," *J. Clin. Pathol.,* vol. 27, p. 973, 1974.

[51] S. Sikder, J. M. Reyes, C. S. Moon, O. Suwan-apichon, J. H. Elisseeff and R. S. Chuck, "Noninvasive mitochondrial imaging in live cell culture," *photochem. photobiol.,* vol. 81, no. 6, pp. 1569-71, 2005.

[52] M. Yurkin, Discrete Dipole Simulations of Light Scattering by Blood Cells, The Netherlands: PrintPartners Ipskamp B.V., 2007.

[53] R. S. Brock, Modeling Light Scattering from Biological Cells Using a Finite-Difference Time-Domain Method, Greenville, NC: East Carolina University, 2007.

[54] C. F. Bohren and D. R. Huffman, Absorption and Scattering of Light by Small Particles, New York: John Wiley & Sons, 1983.

[55] M. Mishchenko, L. Travis and A. Lacis, Multiple Scattering of Light by Particles,

Cambridge: Cambridge U. Press, 2006.

[56] A. Lakhtakia and G. W. Mulholland, "On two numerical techniques for light scattering by dielectric agglomerated structures," *J. Res. Natl. Inst. Stand. Technol.*, vol. 98, p. 699, 1993.

[57] B. T. Draine, "The discrete-dipole approximation and its application to interstellar graphite grains," *Astrophys. J.*, vol. 333, pp. 848-872, 2004.

[58] A. K. Dunn, Light Scattering Properties of Cells, Austin, TX: University of Texas at Austin, 1997.

[59] A. Taflove and S. Hagness, Computational Electrodynamics: The Finite-Difference Time-Domain Method, Boston: Artech House, 2000.

[60] M. I. Mishchenko, J. W. Hovenier and L. D. Travis, Light Scattering by Nonspherical Particles, San Diego: Academic Press, 2000.

[61] R. S. Brock, X. H. Hu, P. Yang and J. Q. Lu, "Evaluation of a parallel FDTD code and application to modeling of light scattering by deformed red blood cells," *Optics Express*, vol. 13, pp. 5279-5292, 2005.

[62] M. A. Yurkin, A. G. Hoekstra, R. S. Brock and J. Q. Lu, "Systematic comparison of the discrete dipole approximation and the finite difference time domain method for large dielectric scatterers," *Opt. Express*, vol. 15, pp. 17902-17911, 2007.

[63] W. S. Bickel, J. F. Davidson, D. R. Huffman and R. Kilkson, "Application of polarization effects in light scattering: A new biophysical tool," *Proc. Natl. Acad. Sci. U.S.A.*, vol. 73, pp. 486-490, 1976.

[64] T. Nousiainen, Light Scattering by Nonspherical Atmospheric Particles, Helsinki: University of Helsinki, 2002.

[65] C. Liu, C. Capjack and W. Rozmus, "3-D simulation of light scattering from biological cells and cell differentiation," *J. Biomed. Opt.*, vol. 10, p. 14007, 2005.

[66] H. Volten, J. F. de Haan, J. W. Hovenier, R. Schreus, W. Vassen, A. G. Dekker, H. J. Hoogenboom, F. Charlton and R. Wouts, "Laboratory measurements of angular distributions of light scattered by phytoplankton and silt," *Limnol. Oceanogr.*, vol. 43, pp. 1180-1197, 1998.

[67] H. C. van de Hulst, Light Scattering by Small Particles, New York: Dover Publications,

1981.

[68] W. S. Bickel and W. M. Bailey, "Stokes vectors, Mueller matrices, and polarized scattered light," *Am. J. PHys.* , vol. 53, no. 5, pp. 468-78, 1985.

[69] T. Nousiainen, K. Muinonen and P. Raisanen, "Scattering of light by large saharan dust particles in a modified ray optics approximation," *J. Geophys. Res,* vol. 108, p. 4025, 2003.

[70] T. Nousiainen and G. M. McFarguhar, "Light scattering by quasi-spherical ice crystals," *J. Atmos. Sci.,* vol. 61, pp. 2229-2248, 2004.

[71] E. M. Purcell and C. R. Pennypacker, "Scattering and absorption of light by nonspherical dielectric grains," *Astrophysical Journal,* vol. 186, pp. 705-714, 1973.

[72] B. T. Draine and P. J. Flatau, "Discrete-dipole aproximation for scattering calculations," *J. Opt. Soc. Am .A,* vol. 11, no. 4, pp. 1491-1499, 1994.

[73] M. A. Yurkin, V. P. Maltsev and A. G. Hoekstra, "The discrete dipole approximation for simulation of light scattering by particles much larger than the wavelength," *J. Quant. Spectros. Radiat. Transf.,* vol. 106, pp. 546-557, 2007.

[74] R. W. Freund, "Conjugate gradient-type methods for linear systems with complex symmetric coefficient matrices," *SIAM J. Sci. Stat. Comput.*, vol. 13, no. 1, pp. 425-448, 1992.

[75] S. W. Zucker and D. Terzopoulos, "Finding structure in co-occurrence matrices for texture analysis," *Computer graphics and image processing,* vol. 12, pp. 286-308, 1980.

[76] H. A. Habib, M. H. Yousaf and M. Mohibullah, "Modified laws energy descriptor for inspection of ceramic tiles," *National Conference on Emerging Technologies,* 2004.

[77] D. Gabor, "Theory of communication," *J. of the Institute of Electrical Engineers,* vol. 93, pp. 429-457, 1946.

[78] B. S. Manjunath and W. Y. Ma, "Texture features for browsing and retrieval of image data," *IEEE Trans. Pattern Anal. Mach. Intell.*, vol. 18, pp. 837-842, 1996.

[79] J. Dougman, "Two-dimensional analysis of cortical receptive field profiles," *Vision Research,* vol. 20, pp. 846-856, 1980.

[80] D. S. Zhang and G. Lu, "Content-based image retrieval using gabor texture features," *Proc.*

of First IEEE Pacific-Rim Conference on Multimedia (PCM'00), pp. 392-395, 2000.

[81] B. Manly, Multivariate Statistical Methods: A Primer, Boca Raton, FL: CRC Press, 2005.

[82] J. Torppa, J. P. Valkonen and K. Muinonen, "Three-dimensional stochastic shape modeling for potato tubers," *Potato Res.*, vol. 49, pp. 109-118, 2006.

[83] M. Tegmark, "An icosahedron-based method for pixelizing the celestial sphere," *ApJ Lett,* vol. 470, pp. L81-L84, 1996.

[84] K. Muinonen, T. Nousiainen, P. Fast, K. Lumme and J. Peltoneimi, "Light scattering by Gaussian random particles: Ray optics approximation," *J. Quant. Spect. Rad. Transf.*, vol. 55, no. 5, pp. 577-601, 1996.

[85] K. Muinonen, "Introducing the Gaussian shape hypothesis for asteroids and comets," *Astron. Astrophys.*, vol. 332, pp. 1087-1098, 1998.

[86] E. Vanmarcke, Random Fields: Analysis and Synthesis, cambridge, MA: MIT Press, 1983.

[87] J. Bennett and L. Mattsson, Introduction to Surface Roughness and Scattering, Washington, D.C.: Opt. Soc. of America, 1999.

[88] K. M. Jacobs, J. Q. Lu and X. H. Hu, "Development of a diffraction imaging flow cytometer," *Opt. Lett.*, vol. 34, pp. 2985-2987, 2009.

[89] D. Clausi, "An analysis of co-occurrence texture statistics as a function of grey level quantization," *Canadian Journal of Remote Sensing*, vol. 28, pp. 45-62, 2002.

APPENDIX A: REPRESENTATION OF AN ELLIPSOID WITH ARBITRARY ORIENTATION IN SPHERICAL COORDINATES

This appendix provides the equation for an ellipsoid that is used to model the base shape of the cell models. It was derived as described in §6.1.

$$
\begin{aligned}
r_{\mathrm{ell}}(\theta, \varphi) = \sqrt{2}\, a\, b\, c \Big/ \Bigg(& \cos^2(\gamma) \left(c^2 \sin^2(\theta) \sin^2(\phi - \varphi) \left(a^2 + (a - b)(a + b) \cos(2\phi) + b^2 \right) + 2\, a^2\, b^2 \cos^2(\theta) \right) + \\
& c^2 \left(b^2 - a^2 \right) \sin(\gamma) \sin(2\theta) \sin(2\phi) \cos(\phi - \varphi) + \\
& c^2 \cos(\gamma) \sin(\theta) \Big(2 \sin(\gamma) \cos(\theta) \sin(\phi - \varphi) \left(a^2 + (a - b)(a + b) \cos(2\phi) + b^2 \right) + \\
& \quad \left(b^2 - a^2 \right) \sin(\theta) \sin(2\phi) \sin(2(\phi - \varphi)) \Big) + 2\, c^2 \sin^2(\gamma) \cos^2(\theta) \left(a^2 \cos^2(\phi) + b^2 \sin^2(\phi) \right) + \\
& \frac{1}{2} \sin^2(\theta) \Big(2\, c^2 \left(b^2 - a^2 \right) \cos(2\phi) \cos^2(\phi - \varphi) + \left(c^2 \left(a^2 + b^2 \right) - a^2\, b^2 \right) \cos(2(\phi - \varphi)) + \\
& \quad c^2 \left(a^2 + b^2 \right) + a^2\, b^2 \Big) - a^2\, b^2 \sin(2\gamma) \sin(2\theta) \sin(\phi - \varphi) - a^2\, b^2 \cos(2\gamma) \sin^2(\theta) \sin^2(\phi - \varphi) \Bigg)^{1/2}
\end{aligned}
$$

APPENDIX B: CLASSIFICATION RESULTS FOR INCIDENT LINEAR POLARIZATIONS PARALLEL AND AT A 45° ANGLE TO THE SCATTERING PLANE

This appendix provides the classification results for the polarization images mentioned in §9.2.

Table B1. Classification accuracy for various cell characteristics for incident linear polarization parallel to the scattering plane

Cell characteristic	Scattering planes					
	Side/ 45°/ fwd	Side/ 45°	Side/ fwd	Side	45°/ fwd	45°
Cell surface roughness (μm)						
0.11/0.29/0.39	0.74	0.71	0.62	0.61	0.68	0.65
0.11/0.29	0.84	0.84	0.76	0.76	0.79	0.78
0.29/0.39	0.79	0.77	0.69	0.67	0.75	0.71
0.11/0.39	0.96	0.94	0.88	0.87	0.91	0.89
Nuclear size (N/C %)						
30.0/40.0/50.0	0.69	0.55	0.66	0.49	0.66	0.52
30.0/40.0	0.77	0.65	0.75	0.58	0.74	0.64
40.0/50.0	0.81	0.74	0.79	0.72	0.78	0.70
30.0/50.0	0.93	0.79	0.91	0.74	0.91	0.75
Mitochondrial distribution						
Diffuse/Peripheral/Perinuclear	0.66	0.64	0.55	0.54	0.64	0.61
Diffuse/Peripheral	0.80	0.78	0.73	0.71	0.78	0.74
Peripheral/Perinuclear	0.87	0.86	0.78	0.78	0.85	0.82
Diffuse/Perinuclear	0.71	0.70	0.64	0.64	0.69	0.70
Mitochondrial volume density (M/C %)						
2.0/5.0/8.0	0.76	0.76	0.71	0.71	0.63	0.63
2.0/5.0	0.88	0.88	0.84	0.84	0.79	0.79
5.0/8.0	0.77	0.77	0.74	0.73	0.69	0.67
2.0/8.0	0.94	0.94	0.93	0.93	0.87	0.86
Mitochondrial size *a* (μm)						
0.26/0.44	0.89	0.89	0.73	0.73	0.79	0.79
Mitochondrial shape AR						
1.6/3.6	0.63	0.61	0.54	0.54	0.60	0.60

Table B2. Classification accuracy for various cell characteristics for incident linear polarization at a 45° angle to the scattering plane

Cell characteristic	Scattering planes					
	Side/ 45°/ fwd	Side/ 45°	Side/ fwd	Side	45°/ fwd	45°
Cell surface roughness (μm)						
0.11/0.29/0.39	0.74	0.71	0.62	0.61	0.68	0.65
0.11/0.29	0.84	0.84	0.76	0.76	0.80	0.78
0.29/0.39	0.79	0.76	0.69	0.68	0.75	0.71
0.11/0.39	0.96	0.94	0.88	0.86	0.91	0.89
Nuclear size (N/C %)						
30.0/40.0/50.0	0.70	0.55	0.67	0.49	0.66	0.52
30.0/40.0	0.77	0.65	0.74	0.58	0.74	0.64
40.0/50.0	0.81	0.74	0.79	0.72	0.78	0.70
30.0/50.0	0.93	0.79	0.91	0.74	0.91	0.75
Mitochondrial distribution						
Diffuse/Peripheral/Perinuclear	0.66	0.64	0.56	0.54	0.64	0.61
Diffuse/Peripheral	0.80	0.78	0.73	0.71	0.78	0.74
Peripheral/Perinuclear	0.87	0.86	0.78	0.77	0.85	0.82
Diffuse/Perinuclear	0.71	0.71	0.64	0.64	0.69	0.70
Mitochondrial volume density (M/C %)						
2.0/5.0/8.0	0.76	0.76	0.71	0.71	0.63	0.63
2.0/5.0	0.88	0.88	0.85	0.85	0.79	0.79
5.0/8.0	0.77	0.77	0.74	0.73	0.69	0.67
2.0/8.0	0.95	0.95	0.93	0.93	0.87	0.86
Mitochondrial size *a* (μm)						
0.26/0.44	0.89	0.89	0.73	0.73	0.79	0.79
Mitochondrial shape AR						
1.6/3.6	0.63	0.62	0.55	0.54	0.60	0.60